

# Dissertation

submitted to the

Combined Faculty for the Natural Sciences and Mathematics  
of the Ruperto-Carola University of Heidelberg, Germany

for the degree of

Doctor of Natural Sciences

presented by

Dipl. Math. Melanie Rinas  
born in Bad Saulgau, Germany

Oral-examination: \_\_\_\_\_



# Modeling the competition between virus infection and the antiviral interferon response

Referees: Prof. Dr. Anna Marciniak-Czochra  
Prof. Dr. Thomas Höfer



# Contents

<b>Abstract</b>	<b>i</b>
<b>Zusammenfassung</b>	<b>iii</b>
<b>1. Introduction</b>	<b>1</b>
1.1. Research on the antiviral interferon defense . . . . .	1
1.2. Outline of this thesis . . . . .	1
<b>2. Stochastic modeling predicts paracrine propagation of the IFN response induced by individual sentinels</b>	<b>3</b>
2.1. Experimental study of the IFN system reveals multi-layered stochasticity in individual cells . . . . .	4
2.1.1. Monitoring virus-induced IFN induction and response at single-cell level . . . . .	4
2.1.2. Cell-to-cell variability in IFN induction . . . . .	5
2.1.3. IFN target gene induction is an all-or-nothing switch . . . . .	11
2.2. Stochastic model of the IFN response against viral infection . . . . .	15
2.2.1. Stochastic simulation based on Gillespie's algorithm . . . . .	15
2.2.2. Model of virus-induced IFN signaling in single cells along with cell-to-cell communication through secreted IFN . . . . .	16
2.2.3. Model simulations using Gillespie's algorithm . . . . .	20
2.3. Estimation of the model parameters of the stochastic model . . . . .	25
2.3.1. Parameter determination for the virus-induced activation of the transcription factors of IFN . . . . .	25
2.3.2. Parameter determination of the IFN expression . . . . .	28
2.3.3. Parameter determination of the IFN response . . . . .	32
2.4. Stochastic modeling exposes individual IFN producers as sentinels of viral infection . . . . .	34
<b>3. Population-based modeling reveals major control of viral fitness by the antiviral effect of IFN on already infected cells</b>	<b>37</b>
3.1. Dissecting the dynamics of IFN-induced antiviral defense against spreading DENV in living cells . . . . .	38
3.1.1. Detection of the immediate interactions between DENV infection and the antiviral IFN response at single-cell level . . . . .	38
3.1.2. The competition between spreading DENV and IFN-induced antiviral protection . . . . .	43
3.1.3. Cell-to-cell heterogeneity of DENV replication and IFN response reveal coexistence of viral spread and antiviral protection	47

3.1.4. Examination of viral fitness by comparing DENV-wt with a DENV mutant lacking 2'-O-methyltransferase activity . . . . .	51
3.2. Population-based delay-differential equation model of viral spread and IFN-induced antiviral defense . . . . .	55
3.3. Parameterization of the population-based delay-differential equation model . . . . .	60
3.3.1. Estimation of model parameters by using DENV-wt measurements . . . . .	60
3.3.2. Detection of DENV mutant specific model parameters by utilizing the knowledge from wt-fitting . . . . .	68
3.4. Extension of the population-based model to analyze explicitly the autocrine and paracrine effect of IFN . . . . .	71
3.5. Quantitative modeling predicts strong limitation of viral spread by the antiviral effect of IFN on infected cells . . . . .	77
<b>4. Discussion</b>	<b>81</b>
<b>A. Appendix</b>	<b>83</b>
A.1. Jacobian matrices of the delay-differential equation model . . . . .	83
A.2. Jacobian matrices of the full delay-differential equation model . . . . .	84
A.3. The full model reproduces the observed dynamics of both DENV-wt and DENV-E217A mutant infections . . . . .	85
<b>Bibliography</b>	<b>86</b>
<b>Abbreviations and symbols</b>	<b>96</b>
<b>Acknowledgments</b>	<b>103</b>

# **Abstract**



# **Zusammenfassung**



# 1. Introduction

## 1.1. Research on the antiviral interferon defense

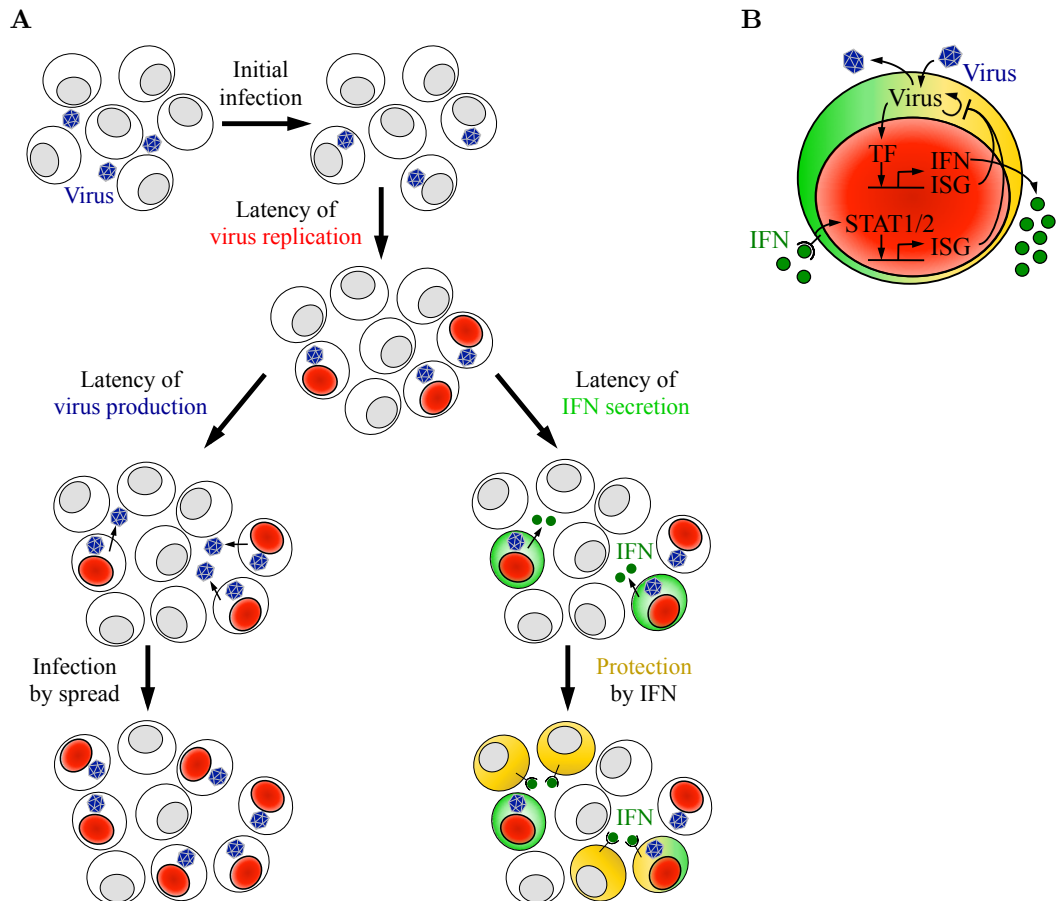


**Figure 1.1.:** (A) Population level (B) Single-cell level. (○)

## 1.2. Outline of this thesis



## **2. Stochastic modeling predicts paracrine propagation of the IFN response induced by individual sentinels**

The interferon (IFN) system, as the first line of defense against viral infections, has a central antiviral function (Kunzi and Pitha (2003), Sadler and Williams (2008), Takeuchi and Akira (2009)). Since the expression of IFN is crucial to induce an antiviral protective state, it is quite surprising that only a fraction of cells in a virus-infected cell population induces IFN (Zawatzky et al. (1985), Hu et al. (2007)).

The literature suggests various reasons for the observed cell-to-cell variability in IFN expression. Some studies have concluded that host cell-intrinsic causes, such as a mechanism of IFN gene induction (Hu et al. (2007), Apostolou and Thanos (2008)) or cellular variance in expression of the viral sensor protein retinoic-acid inducible gene-I (RIG-I) (Hu et al. (2011)) lead to heterogeneous IFN production. Alternatively, the infecting virus may be responsible for the stochasticity in IFN induction (Chen et al. (2010), Killip et al. (2011)). According to the involved cell type or virus it could be that multiple factors contribute to the heterogeneity in IFN induction.

To study cell-to-cell variability of the IFN system, our cooperation partners Ulfert Rand, Mario Köster and Hansjörg Hauser from the Department of Gene Regulation and Differentiation at the Helmholtz Centre for Infection Research (HZI) in Braunschweig generated a set of reporter constructs to monitor successive steps of IFN induction and IFN response in single cells (cf. section 2.1.1, Rand and Hauser (2010)). Live-cell imaging data demonstrate that all key steps of the IFN system - the virus-induced signal transduction, the IFN expression (cf. section 2.1.2), and the induction of IFN-stimulated genes (ISGs) (cf. section 2.1.3) - are stochastic events in single cells. Additional experiments reveal that cell-intrinsic variability contributes to the detected heterogeneity in IFN induction (cf. section 2.1.2). Moreover, the examination of the response to IFN discover a dose-dependent binary pattern of two distinct subpopulations (cf. section 2.1.3). The IFN-responding subpopulation achieves an antiviral protected state, while virus can still replicate in the non-responding cell fraction.

Based on the observed stochastic dynamics of the IFN network we establish a multi-scale mathematical model, which is simulated using Gillespie's stochastic simulation algorithm (cf. section 2.2 - 2.3). The model describes the intracellular viral replication, the expression of IFN and the activation of ISGs in individual cells together

## 2. Stochastic modeling predicts paracrine propagation of the IFN response

with the intercellular communication through secreted IFN. Our experimentally verified simulations predict that a small fraction of IFN-producing cells are sufficient to induce IFN target genes in the other, non-producing cells of the population (cf. section 2.4). Thus, we expect that the stochastic sensing of viral infections by the innate immune system together with the paracrine signal propagation provide an efficient and viral-load sensitive mechanism to limit viral spread (Rand and Rinas et al. (2012)).

### 2.1. Experimental study of the IFN system reveals multi-layered stochasticity in individual cells

#### 2.1.1. Monitoring virus-induced IFN induction and response at single-cell level

The finding that only a fraction of infected cells induces IFN (Zawatzky et al. (1985), Hu et al. (2007)) demonstrates the necessity to investigate the IFN system at single-cell level. A valuable method to monitor the dynamics and variability of individual cells in real time is provided by live-cell imaging (Spiller et al. (2010)). The first live-cell analysis for the IFN system was realized by our collaboration partners Ulfert Rand, Mario Köster and Hansjörg Hauser from the Department of Gene Regulation and Differentiation at the Helmholtz Centre for Infection Research (HZI) in Braunschweig (Rand and Hauser (2010)).

Hauser and colleagues developed fluorescence reporter cells to visualize successive key steps of the IFN system consisting of (i) virus-induced signal transduction, (ii) IFN expression and (iii) IFN response (Figure 2.1). The signal transduction after the recognition of viruses by the intracellular receptor RIG-I results in the nuclear translocation of the nuclear factor  $\kappa$ B (NF- $\kappa$ B) and the IFN regulatory factors (IRFs) 3 as well as 7 (Brennan and Bowie (2010)). To observe the nuclear translocation of the transcription factors, the scientists at the HZI designed dual reporter cells which were labeled with the fluorescent markers NF- $\kappa$ B/p65-YFP (yellow fluorescence protein) and IRF-7-CFP (cyan fluorescence protein), respectively. The presence of transcription factors in the nucleus induces the expression of IFN including IFN- $\beta$  (Theofilopoulos et al. (2005)). The induction of IFN- $\beta$  was monitored by transfecting murine fibroblasts with a bacterial artificial chromosome (BAC) encoded reporter expressing TurboGFP (green fluorescence protein) under the control of the IFN- $\beta$  promoter (IFN- $\beta$ -tGFP). Another BAC-based reporter construct in which the mCherry gene is linked to the C-terminal end of the genomic IRF-7 sequence (IRF-7-mCherry, monomeric cherry red fluorescent protein) enables the investigation of the prototypical ISG IRF-7 in response to secreted IFN (Honda et al. (2005)). All reporter constructs were transfected into murine NIH3T3 fibroblasts and representative stable cell clones were utilized for the studies (Rand and Rinas et al. (2012); Supplementary Figure S2 and Supplementary Figure S8, Rand and Hauser (2010)).

## 2.1. Experimental study of the IFN system reveals multi-layered stochasticity

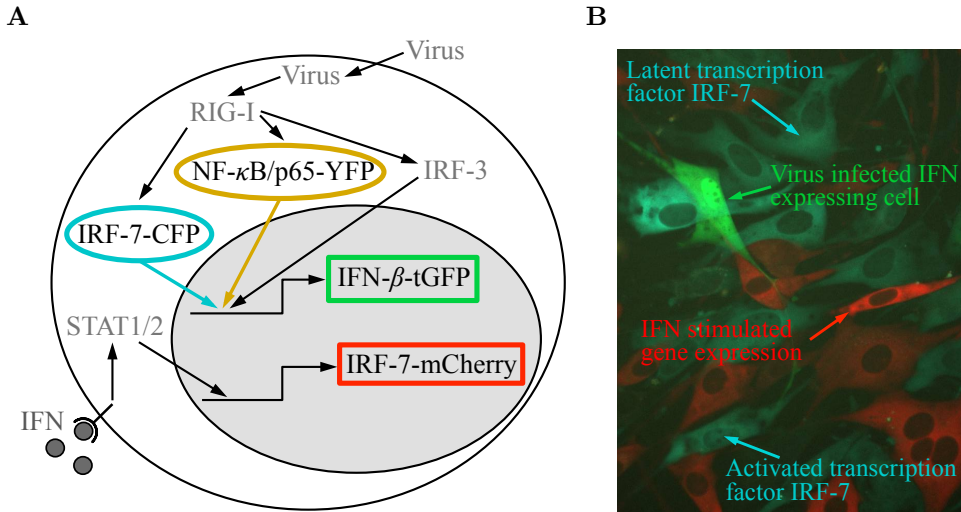


**Figure 2.1.:** Visualization of the key steps of the IFN pathway with fluorescence reporter cells. (A) Scheme of the established intracellular reporters. Virus recognition by RIG-I causes the nuclear translocation of the fusion proteins IRF-7-CFP (cyan cytoplasm → cyan nucleus) and NF-κB/p65-YFP (yellow cytoplasm → yellow nucleus). Subsequent IFN- $\beta$  expression becomes visible through the BAC reporter IFN- $\beta$ -tGFP (green cytoplasm) and induces the expression of ISGs illustrated by the BAC construct IRF-7-mCherry (red cytoplasm). (B) Fluorescence picture of the generated intracellular reporters. The virus-induced activation of the latent transcription factor IRF-7 (cyan cytoplasm) lead to its nuclear translocation (cyan nucleus). The following expression of IFN (green cytoplasm) results in the induction of ISGs (red cytoplasm). (Experiments by Ulfert Rand, Mario Köster and Hansjörg Hauser)

### 2.1.2. Cell-to-cell variability in IFN induction

In order to examine the properties of virus-induced IFN expression after infection, we used the enveloped single-stranded RNA Newcastle Disease Virus (NDV). The paramyxovirus NDV causes the contagious Newcastle disease in birds and a close contact to infected animals can trigger conjunctivitis as well as influenza-like symptoms in humans (Capua and Alexander (2004)). After infection NDV replicates and induces IFN expression in cells via the viral RNA sensor RIG-I (Kato et al. (2005), Childs et al. (2007)), but the NDV virus cannot generate new infectious virus particles (Rott (1979)). Therefore our experimental setup allows the examination of IFN induction after primary infection.

As we are primarily interested in the single-cell behavior of IFN expression, we firstly monitored IFN- $\beta$ -tGFP reporter cells by time-lapse microscopy (cf. section 2.1.1) after infection with different doses of NDV given in haemagglutinating unit per milliliter (HAU/ml) (Figure 2.2A left, Rand and Rinas et al. (2012): Supplementary Movie S1). The IFN- $\beta$ -producing cells started at various times to express IFN- $\beta$  with cell-to-cell differences of up to 20 h. Although we detected earlier onset of IFN- $\beta$ -tGFP induction after infection with higher viral loads, the relative variability or “noise” (Swain et al. (2002), Elowitz et al. (2002), Kærn et al. (2005)) which can be calculated with the coefficient of variation ( $CV$ ; standard deviation divided by

## 2. Stochastic modeling predicts paracrine propagation of the IFN response

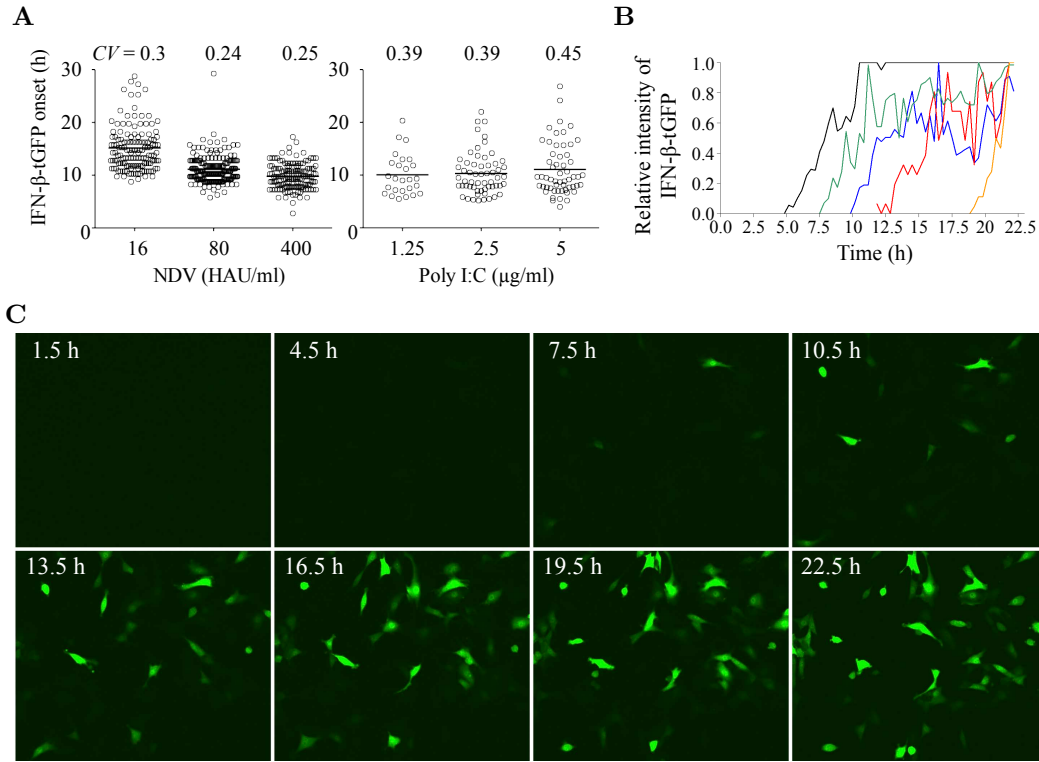


**Figure 2.2.: Cell-to-cell heterogeneity in onset of IFN- $\beta$  expression.** (A) Single-cell variability in IFN- $\beta$  induction is virus-independent. IFN- $\beta$ -tGFP reporter cells were infected for 1 h with different doses of NDV (left, x-axis) or transfected with varying concentrations of poly I:C (right, x-axis). Onset of IFN- $\beta$ -tGFP expression (y-axis) was detected by time-lapse microscopy at 15 min intervals. The scatter plots show the distribution of 456 NDV infected cells or 140 poly I:C transfected cells, respectively. Experiment-related coefficient of variation ( $CV$ ) is given at the top. (B, C) Live imaging illustrates heterogeneous IFN- $\beta$  induction in individual cells. IFN- $\beta$ -tGFP reporter cells were stimulated with 32  $\mu$ g/ml poly I:C and subsequently monitored via time-lapse microscopy every 20 min. Selected single-cell kinetics in (B) and fluorescence pictures at indicated time post stimulation in (C) are presented. (Experiments by Ulfert Rand, Mario Köster and Hansjörg Hauser)

mean) varied only slightly (Figure 2.2A top left).

Moreover, we analyzed if the temporal heterogeneity in IFN- $\beta$  expression is determined by varying times of infection or due to intrinsic features of the host cell. Therefore we bypassed viral infection through liposome transfection of the viral-surrogate polyinosinic-polycytidylic acid (poly I:C) stimuli (liposome-free delivery of poly I:C did not induce IFN- $\beta$  expression) into IFN- $\beta$ -tGFP reporter cells (Figure 2.2A right, B and C). Also after transfection with different poly I:C concentrations we observed an extremely heterogeneous onset of IFN- $\beta$  expression in individual cells, which was quantitatively comparable to viral infection as seen by the same order of magnitude of the  $CV$ s (Figure 2.2A top right). These data reveal that the cell-to-cell variance in IFN- $\beta$  expression is predominantly of cellular origin.

To quantitatively determine viral replication and IFN induction in single cells, IFN- $\beta$ -tGFP reporter cells were infected with NDV and subjected to flow cytometry.

## 2.1. Experimental study of the IFN system reveals multi-layered stochasticity

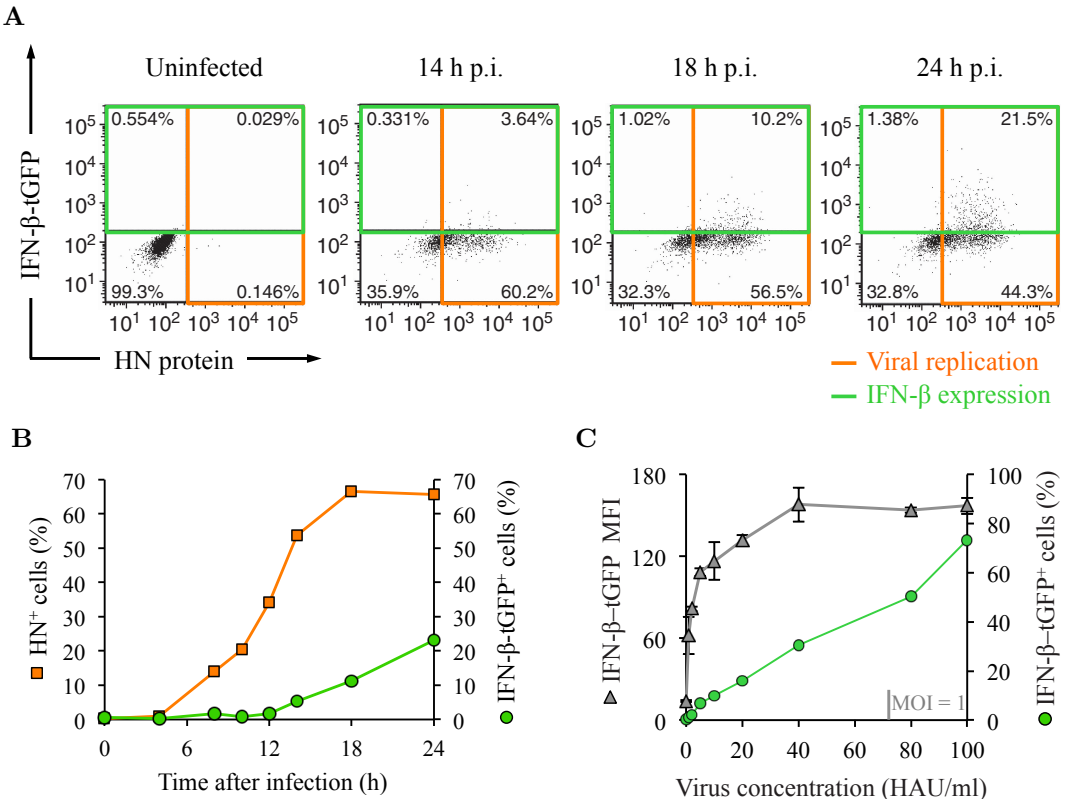


**Figure 2.3.: Quantitative and temporal heterogeneity in IFN- $\beta$  expression.** (A, B) Viral replication is necessary but not sufficient to activate IFN- $\beta$  expression. IFN- $\beta$ -tGFP reporter cells infected with 40 HAU/ml NDV for 1 h were subjected to flow cytometry at the indicated time points post infection (p.i.). Representative dot plots in (A) illustrate the jointly measured viral HN protein (x-axis) as well as IFN- $\beta$ -tGFP (y-axis) of individual cells. The corresponding kinetics of virus replicating cells (HN<sup>+</sup>, orange color) and IFN- $\beta$  expressing cells (IFN- $\beta$ -tGFP<sup>+</sup>, green color) are shown in (B). (C) Secreted IFN is determined by the fraction of IFN-producing cells. IFN- $\beta$ -tGFP reporter cells were infected with 1, 2, 5, 10, 20, 40, 80 or 100 HAU/ml NDV and analyzed by flow cytometry 24 h after infection. Illustrated are the fraction of IFN- $\beta$  positive cells (IFN- $\beta$ -tGFP<sup>+</sup>, green color) and the respective geometric mean of the fluorescence intensity (MFI, gray color, mean of triplicate measurements and error bars). (Experiments by Ulfert Rand, Mario Köster and Hansjörg Hauser)

At several time points post infection (p.i.) we measured simultaneously the viral hemagglutinin-neuraminidase (HN) protein and the IFN- $\beta$ -tGFP intensity (Figure 2.3A and B). The increasing fraction of virus replicating cells over time was followed by an about 12 h delayed rising number of IFN- $\beta$ -tGFP positive cells. As in other studies (Kumagai et al. (2009), Rehwinkel et al. (2010)), we detected IFN- $\beta$ -tGFP expression only in cells with replicating virus. However, a remarkable number of infected cells did not express IFN. To analyze this phenomenon further, we divided the amount of infected cells into cells with low or high viral load, respectively (Rand and Rinas et al. (2012): Supplementary Figure S3). Since both subpopulations contained nearly the same fraction of IFN- $\beta$ -tGFP positive cells, we found no correlation between the level of viral replication and the property to express IFN- $\beta$ -tGFP. In the literature it was discussed, that the absence of IFN-inducing viral RNA may be

## 2. Stochastic modeling predicts paracrine propagation of the IFN response

responsible for the heterogeneity in IFN expression (Killip et al. (2011)). Thus, we transfected intracellular RNA of IFN-producing and non-producing cells into naïve IFN- $\beta$ -tGFP reporter cells (Rand and Rinas et al. (2012): Figure 2C and Supplementary Figure S4). As both RNA transfections activated a comparable fraction of IFN- $\beta$ -tGFP positive cells, heterogeneous IFN induction appears despite the presence of IFN-inducing viral RNA. These results demonstrate that viral replication is necessary to induce IFN but not sufficient.

Moreover, we investigated the properties of IFN- $\beta$ -tGFP expression after infection with different virus doses (Figure 2.3C). The fraction of IFN- $\beta$ -tGFP positive cells increased almost linearly with higher virus concentrations and a multiplicity of infection (MOI; number of infectious virus particles divided by the number of potential host cells) of 1 induced IFN expression in less than half of the IFN- $\beta$ -tGFP reporter cells. In contrast, the mean fluorescence intensity (MFI) of IFN- $\beta$  expression reached ~ 70% of its maximum already at very low virus titer. Therefore, virus-induced IFN- $\beta$  production is dominated by the fraction of IFN- $\beta$  expressing cells.

To examine mechanistically how cell-to-cell variability in IFN expression arises, we had a closer look on the IFN induction pathway. We analyzed the virus-induced activation of the key transcription factors NF- $\kappa$ B and IRF-7 by utilizing the dual reporter cells expressing NF- $\kappa$ B/p65-YFP and IRF-7-CFP (cf. section 2.1.1). After infection with NDV, initially in the cytoplasm located latent transcription factors NF- $\kappa$ B and IRF-7 translocated into the nucleus (Figure 2.4A). The nuclear translocation of both transcription factors happened simultaneously in a single cell, but this joint translocation time varied strongly between different cells from 7 to 20 h post infection (Figure 2.4B). We also observed a joint translocation time of the transcription factors NF- $\kappa$ B/p65 and IRF-3 in individual cells by antibody staining of endogenous NF- $\kappa$ B/p65 as well as IRF-3 after infection with NDV or transfection with poly I:C (Rand and Rinas et al. (2012): Supplementary Figure S6). The discovery of a single cell specific but in the cell population diverse translocation time of the key transcription factors of IFN demonstrates that strong cell-to-cell heterogeneity in IFN induction originates already in the shared upstream activation pathway of NF- $\kappa$ B and IRF-7.

Additionally, we studied the relation between transcription factor activation and IFN induction using dual reporter cells expressing IRF-7-CFP together with IFN- $\beta$ -tGFP (Figure 2.4C as well as Rand and Rinas et al. (2012): Supplementary Figure S7). Most of the cells (91% at 80 HAU/ml NDV) with activated transcription factor IRF-7 also expressed IFN afterwards (Figure 2.4D). The few cells (9% at 80 HAU/ml NDV) which exhibited no IFN- $\beta$  expression after transcription factor activation showed similar distributed IRF-7 nuclear translocation times as the IFN- $\beta$  producing cells (Figure 2.4D bottom part). Since we found no IFN- $\beta$ -tGFP induction without prior nuclear translocation of IRF-7, activation of IRF-7 is absolutely necessary for IFN- $\beta$  production. Thus, we suggest that the decision to express IFN is primarily taken upstream of transcription factor activation.

Furthermore, the signaling delay from viral infection to IRF-7 nuclear translocation ( $T_{\text{sig}}$ ; mean value  $\bar{T}_{\text{sig}} = 11.7 \pm 4.0$  h) was comparably broadly distributed among individual cells as already detected with the dual reporter cells expressing the fusion

## 2.1. Experimental study of the IFN system reveals multi-layered stochasticity

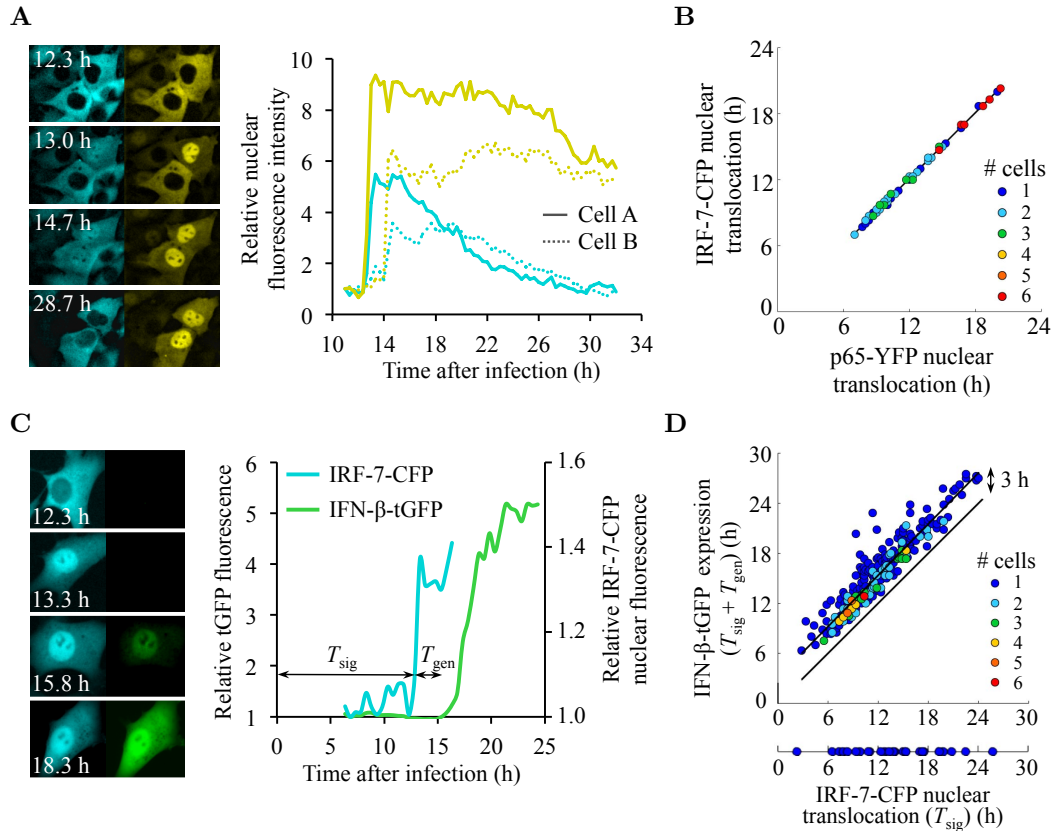


**Figure 2.4.:** Both virus-induced signal transduction and IFN expression are sources of heterogeneity. (A, B) Synchronous translocation time of transcription factors in single cells varies at cell population level. Dual reporter cells expressing the fusion proteins NF- $\kappa$ B/p65-YFP and IRF-7-CFP were infected with 80 HAU/ml NDV for 1 h and monitored by time-lapse microscopy every 20 min. (A) Fluorescence images of subcellular localization of IRF-7-CFP (left column) and p65-YFP (right column) at denoted time post infection. The kinetics show relative nuclear fluorescence for IRF-7-CFP (cyan) and p65-YFP (yellow) of two different cells. (B) Initial nuclear translocation of p65-YFP and IRF-7-CFP were determined in 65 individual cells and plotted against each other. Colored dots represent the frequency of data points. (C, D) Heterogeneous transcription factor activation and IFN expression in single cells. Dual reporter cells expressing IRF-7-CFP together with IFN- $\beta$ -tGFP were infected with 80 HAU/ml NDV and monitored by time-lapse microscopy at 20 min intervals. (C) Fluorescence images of subcellular localization of IRF-7-CFP (left column) and IFN- $\beta$ -tGFP (right column) at given time post infection. The kinetics show relative fluorescence intensity for nuclear IRF-7-CFP (cyan) as well as tGFP (green) of one cell.  $T_{\text{sig}}$  indicates the signaling delay from viral infection to IRF-7 nuclear translocation and  $T_{\text{gen}}$  defines the period of time between nuclear translocation of IRF-7 and onset of IFN- $\beta$ -tGFP expression. (D) Initial nuclear translocation of IRF-7-CFP ( $T_{\text{sig}}$ ) and IFN- $\beta$ -tGFP expression ( $T_{\text{sig}} + T_{\text{gen}}$ ) were determined in 315 individual cells and plotted against each other. Colored dots represent the frequency of data points. (Experiments by Ulfert Rand, Mario Köster and Hansjörg Hauser)

proteins NF- $\kappa$ B/p65-YFP and IRF-7-CFP (Figure 2.4B;  $\bar{T}_{\text{sig}} = 11.9 \pm 3.4$  h). But also the time delay between nuclear translocation of IRF-7 and onset of IFN- $\beta$ -tGFP expression ( $T_{\text{gen}}$ ; mean value  $\bar{T}_{\text{gen}} = 3.4 \pm 1.5$  h) differed remarkably from cell-to-cell. The similar CVs of  $T_{\text{sig}}$  ( $CV_{\text{sig}} = 0.34$ ) and  $T_{\text{gen}}$  ( $CV_{\text{gen}} = 0.44$ ) indicate a

## 2. Stochastic modeling predicts paracrine propagation of the IFN response

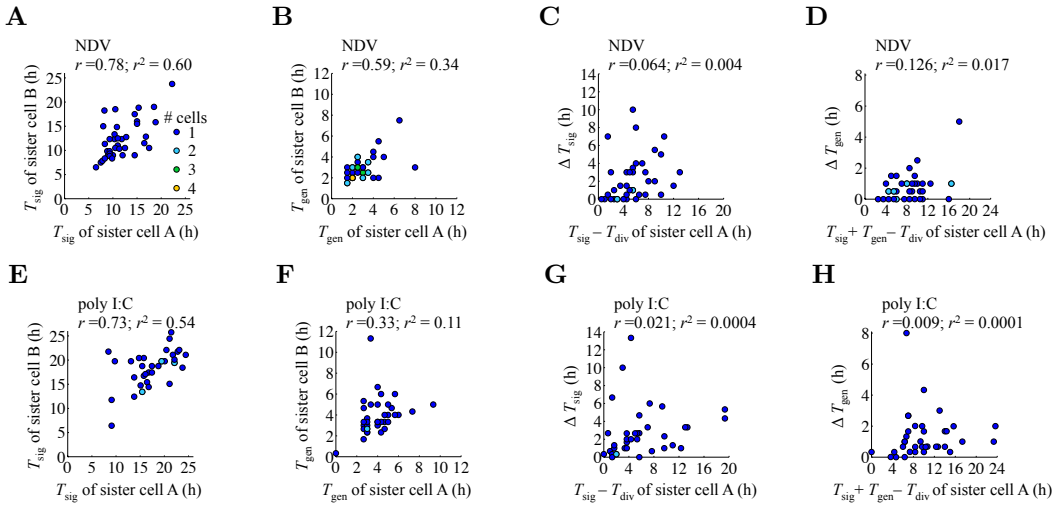


**Figure 2.5.: Heterogeneous IFN induction in sister cells.** (A-H) Dual reporter cells expressing IRF-7-CFP or IRF-7-TagRFP (red fluorescent protein tag) together with IFN- $\beta$ -tGFP were infected with 80 HAU/ml NDV for 1 h (A-D, 38 sister-cell pairs) or transfected with 5 mg/ml poly I:C (E-H, 36 sister-cell pairs) and monitored by time-lapse microscopy every 20 min. Colored dots represent the frequency of data points. Experiment-related correlation coefficient ( $r$ ) and the coefficient of determination ( $r^2$ ) are given at the top. (A, E) Time of IRF-7 nuclear translocation ( $T_{sig}$ ) of sister cell A versus sister cell B. (B, F) Time interval between IRF-7 nuclear translocation and IFN- $\beta$ -tGFP expression ( $T_{gen}$ ) of sister-cell pairs. (C, G) Time elapsed from cell division ( $T_{div}$ ) to IRF-7 nuclear translocation ( $T_{sig} - T_{div}$ ) of one sister cell versus time difference between sister cells regarding IRF-7 signaling ( $\Delta T_{sig}$ ). (D, H) Time elapsed from cell division to IFN- $\beta$ -tGFP expression ( $T_{sig} + T_{gen} - T_{div}$ ) of one sister cell versus time difference between sister cells regarding IFN- $\beta$ -tGFP expression ( $\Delta T_{gen}$ ). (Experiments by Ulfert Rand, Mario Köster and Hansjörg Hauser)

comparable variability of virus-induced signal transduction and subsequent IFN- $\beta$ -tGFP gene expression. These quantitative data thus reveal that both transcription factor activation and IFN- $\beta$  expression are sources of heterogeneity in single cells.

The phenomenon of cell-to-cell variability is widely studied in many different research areas (Raser and O'Shea (2005), Maheshri and O'Shea (2007), Raj and van Oudenaarden (2008), Snijder and Pelkmans (2011)) and classified into intrinsic noise arising from inherent stochastic biochemical reactions and extrinsic noise, which results from extrinsic factors like differences in cell-cycle stage or cellular environment (Elowitz et al. (2002), Swain et al. (2002)). To analyze the origin of the single-cell heterogeneity in our system more closely, we reduced extrinsic fluctuations through examining sister cells which divided during the first hour post infection (Spencer et al. (2009)). To quantify the relation of sister cells we used the correlation coefficient ( $r$ ) and the coefficient of determination ( $r^2$ ). The value of the coefficient of determination can be interpreted as the percentage of the variation that is explained through the correlation between the sister cells (Taylor (1990)). The experiments show that the virus-induced nuclear translocation of IRF-7 happened mainly asynchronously in sister cells with a temporal difference larger than 2 h in  $\sim 50\%$  of the cell pairs (Figure 2.5A). An even weaker relation between sister cells was found for the time of IFN- $\beta$ -tGFP expression after transcription factor activation (Figure

## 2.1. Experimental study of the IFN system reveals multi-layered stochasticity

2.5B), which agrees with the previously described stochastic transcription of the IFN- $\beta$  gene (Apostolou and Thanos (2008)). The corresponding coefficient of determination was 0.6 for  $T_{\text{sig}}$  and 0.34 for  $T_{\text{gen}}$ , which in turn means that 40% of the variability in signaling and 66% of the variability in IFN- $\beta$ -tGFP expression are uncorrelated between sister cells and thus provide an estimate for the cell-intrinsic heterogeneity. In order to verify whether different viral replication kinetics in sister-cell pairs are a source of stochasticity, we repeated the sister cell analysis with poly I:C stimulated reporter cells. Even after transfection with poly I:C the sister cells showed a largely uncorrelated behavior in IRF-7 activation as well as IFN- $\beta$ -tGFP expression (Figure 2.5E and F), with similar coefficients of determination ( $r^2 = 0.54$  for  $T_{\text{sig}}$  and  $r^2 = 0.11$  for  $T_{\text{gen}}$ ) as after viral infection. In addition, we tested if the time of cell division ( $T_{\text{div}}$ ) influences the variation between sister cells in terms of transcription factor activation or IFN- $\beta$  induction. For this purpose, we determined the time elapsed since cell division versus the time difference between sister cells regarding IRF-7 signaling ( $\Delta T_{\text{sig}}$ ) and IFN- $\beta$ -tGFP expression ( $\Delta T_{\text{gen}}$ ) (Figure 2.5C and D for NDV infection; Figure 2.5G and H for poly I:C stimulation). The consideration of cell division yielded very weak correlations which argues against strong impact of the cell cycle on the stochasticity in IFN induction.

In summary, our data revealed two sources of cell-to-cell heterogeneity in IFN induction, namely the virus-induced signal transduction and the subsequent IFN expression (cf. Figure 2.4). According to the sister-cell analysis, approximately half of the stochasticity in both sources can be attributed to cell-intrinsic variability (cf. Figure 2.5). This intrinsic stochasticity provides a rationale for the lack of correlation of viral replication and IFN- $\beta$  expression (cf. Figure 2.3A).

### 2.1.3. IFN target gene induction is an all-or-nothing switch

The observation that many cells with replicating virus do not express IFN- $\beta$  or do so only very late after infection implies an incomplete virus-induced IFN- $\beta$  expression

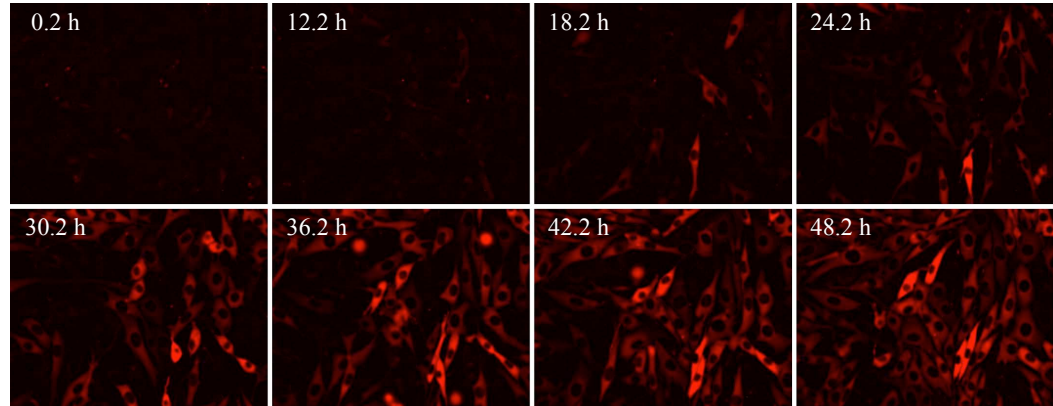


**Figure 2.6.:** Single-cell heterogeneity of IRF-7 expression in response to IFN- $\beta$ . IRF-7-mCherry reporter cells were stimulated with 500 U/ml IFN- $\beta$  and detected by time-lapse microscopy at 30 min intervals. Selected fluorescence pictures at indicated time post stimulation are presented. (Experiments by Ulfert Rand, Mario Köster and Hansjörg Hauser)

## 2. Stochastic modeling predicts paracrine propagation of the IFN response

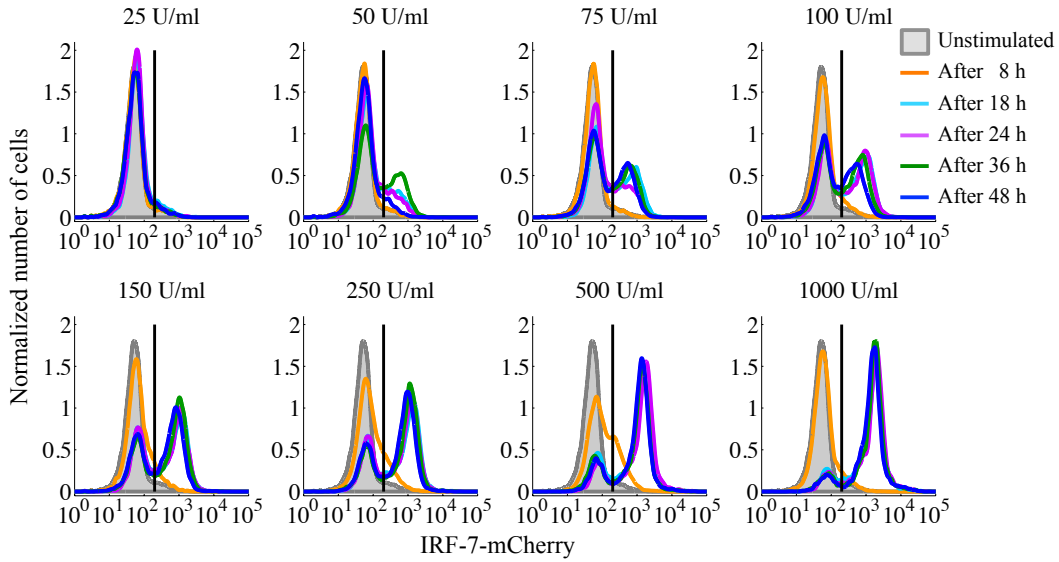


**Figure 2.7.:** Binary time- and dose-dependent IRF-7-mCherry response towards IFN- $\beta$ . IRF-7-mCherry reporter cells were stimulated with increasing concentrations of IFN- $\beta$  indicated at the top of each panel. The intensity of IRF-7-mCherry expression was measured by flow cytometry at multiple time points after stimulation, which is represented through different colors. Normalized distributions are shown to enable the comparison of individual measurements with each other. (Experiments by Ulfert Rand, Mario Köster and Hansjörg Hauser)

(cf. Figure 2.3). To understand the functional consequences of this stochastic and occasional IFN induction, the cellular antiviral response to IFN in terms of ISG expression should also be considered. In the literature we can find quantitative studies of IFN-stimulated signaling which have modeled relevant dynamics at cell-population level (Maiwald et al. (2010)) and regarded effects of single-cell variation (Levin et al. (2011)), but without characterization of ISG expression in individual cells. To investigate IFN response at single-cell level, we stimulated our IRF-7-mCherry reporter cells (cf. section 2.1.1) with IFN- $\beta$  (given in units per milliliter (U/ml)) and monitored IRF-7 expression by time-lapse microscopy (Figure 2.6, Rand and Rinas et al. (2012): Supplementary Movie S2). Surprisingly, individual cells responded very heterogeneously at various time points to IFN- $\beta$  stimulation.

To quantify the observed stochastic response to IFN, IRF-7-mCherry reporter cells were stimulated with different concentrations of IFN- $\beta$  and subjected to flow cytometry at several times after stimulation (Figure 2.7). The distributions of IRF-7-mCherry levels from individual cells showed a digital pattern with distinct IRF-7 expressing and non-expressing subpopulations. The IRF-7 expressing subpopulation increased with the passage of time and higher amount of extracellular IFN- $\beta$ , which implies a time- and dose-dependent response to IFN. We also measured the IFN response in several IRF-7-mCherry clones and detected consistently a binary IRF-7 expression (Rand and Rinas et al. (2012): Supplementary Figure S8). Moreover, the unresponsiveness was not influenced by competition of cells with IFN- $\beta$ , since IFN- $\beta$  was still detectable in the supernatant for more than 30 h (Rand and Rinas et al. (2012): Supplementary Figure S9).

## 2.1. Experimental study of the IFN system reveals multi-layered stochasticity

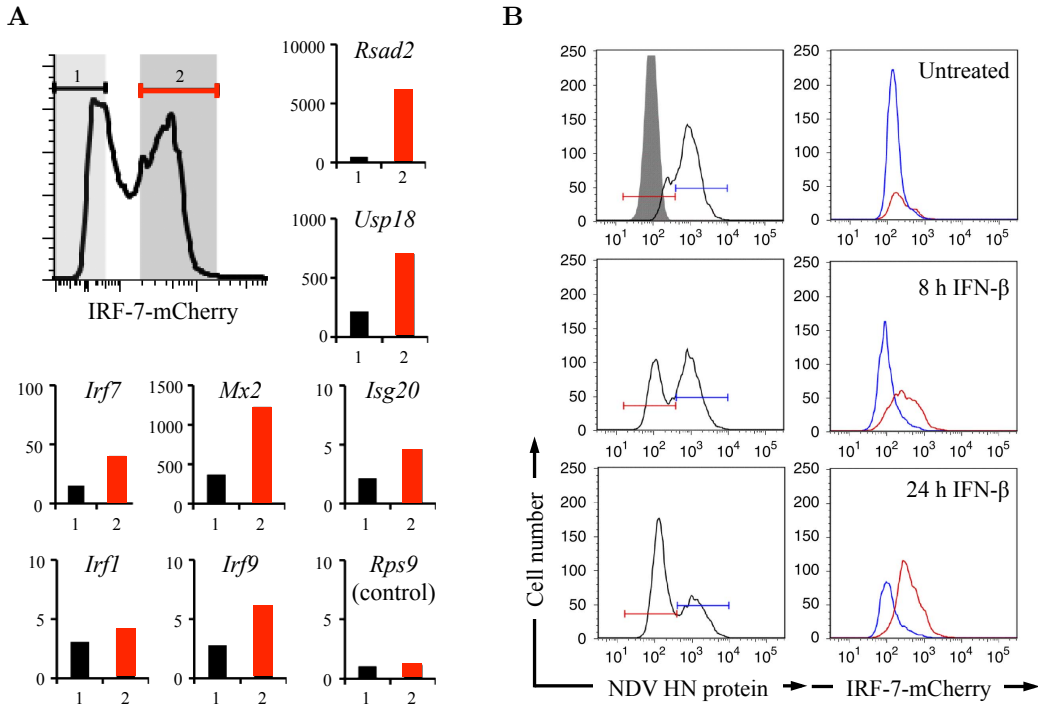


**Figure 2.8:** Bimodality of IRF-7 expression is reflected in ISG transcription and antiviral protection. (A) IRF-7 expression represents production of ISGs. IRF-7-mCherry reporter cells were stimulated with 500 U/ml IFN- $\beta$  for 16 h and subjected to FACS. IRF-7-mCherry negative (1, black) as well as positive (2, red) cells illustrated by the shaded areas were separated. RNA was isolated from both subpopulations and analyzed by qPCR for the expression of indicated ISGs and Rps9 as a control. The bar charts show the fold RNA increase in relation to untreated reporter cells after normalization to  $\beta$ -actin mRNA. (B) IRF-7 expression correlates with antiviral protection. IRF-7-mCherry reporter cells were left untreated (upper row), pre-treated for 8 h (middle row) or 24 h (lower row) with 500 U/ml IFN- $\beta$  and subsequently infected with 80 HAU/ml NDV. After an infection period of 20 h, we measured simultaneously in each single cell the NDV HN intracellular antibody level and IRF-7-mCherry fluorescence intensity by flow cytometry. The NDV HN positive (colored in blue) as well as negative cells (colored in red) were identified (left column) and examined for their respective IRF-7-mCherry expression (right column). (Experiments by Ulfert Rand, Mario Köster and Hansjörg Hauser)

To test whether activation of IRF-7-mCherry correlates with the expression of endogenous ISGs, we separated IRF-7-mCherry negative and positive cells by fluorescence-activated cell sorting (FACS) and analyzed isolated RNA from these cells by quantitative polymerase chain reaction (qPCR) for the expression of common ISGs (Figure 2.8A). All tested ISGs showed enhanced mRNA levels in IRF-7-mCherry expressing cells (Figure 2.8A red bars, whereas the 40S ribosomal protein S9 (RPS9) serves as control). These measurements suggest that a distinct subpopulation of cells which can be identified by IRF-7-mCherry expression coordinately activates an antiviral gene program. To examine this further, we pre-treated IRF-7-mCherry reporter cells with IFN- $\beta$  for 8 or 24 h to allow induction of ISGs and subsequently infected the cells with NDV (Figure 2.8B). Virus replicated in IRF-7-mCherry negative cells (Figure 2.8B in blue color) but not in the IRF-7-mCherry positive cells (Figure 2.8B in red color). Thus, only IRF-7-mCherry expressing cells have been

## *2. Stochastic modeling predicts paracrine propagation of the IFN response*

protected by IFN.

Taken together, our data demonstrate that IFN response is a stochastic, IFN- $\beta$  concentration-dependent, switch in individual cells. This switch is characterized by the all-or-nothing principle, in which virus can replicate in the non-responding subpopulation and the responding subpopulation is protected against viral replication.

## 2.2. Stochastic model of the IFN response against viral infection

The experimental study of the IFN system revealed a remarkable strong single cell heterogeneity of both IFN induction (cf. section 2.1.2) and antiviral IFN response (cf. section 2.1.3). To understand the stochastic dynamics of the IFN network we develop a multi-scale mathematical model that combines the virus-induced IFN signaling in individual cells with the extracellular cell-to-cell communication via secreted IFN in an infected cell population (Figure 2.9). The stochastic state transitions of individual cells with respect to virus replication, IFN induction and IFN response are iterated using Gillespie's algorithm.

### 2.2.1. Stochastic simulation based on Gillespie's algorithm

The stochastic simulation algorithm (SSA) by Daniel T. Gillespie is a Monte Carlo procedure to simulate numerically stochastic kinetics (Gillespie (1976), Gillespie (1977)). It has been proven that the SSA is fully equivalent to the master equation approach, which in turn is the fundamental description of stochastic processes (McQuarrie (1967), Matheson et al. (1975)). The usage of Gillespie's algorithm enables the realization of a continuous-time Markov process (Gillespie (1976), Banks et al. (2011)).

A continuous-time stochastic process  $\{X(t), t \geq 0\}$  is a set of random variables  $X$  at time  $t$  on a countable state space  $Q$ , where  $X$  can be in a state  $s \in Q$ . The process  $\{X(t), t \geq 0\}$  is called a Markov process, if the Markov property

$$\begin{aligned} & \mathcal{P}(X(t_{n+1}) = s_{n+1} | X(t_0) = s_0, X(t_1) = s_1, \dots, X(t_n) = s_n) \\ &= \mathcal{P}(X(t_{n+1}) = s_{n+1} | X(t_n) = s_n) \end{aligned} \quad (2.1)$$

is fulfilled for all  $n \in \mathbb{N}_0$ , successive times  $t_0 \leq t_1 \leq \dots \leq t_n \leq t_{n+1}$  and states  $s_0, s_1, \dots, s_{n+1} \in Q$  (Waldmann and Stocker (2004)). The used term  $\mathcal{P}(A | B)$  denotes the conditional probability of  $A$  under the condition  $B$ . The Markov property therefore requires a memoryless system in which a state change depends only on the current state and not on the past history.

In general, the Gillespie algorithm is applied to simulate the dynamic process of a heterogeneous population. The individuals of this population can be in  $K$  different states  $\{S_1, \dots, S_K\}$  and the transitions between the states are specified through  $M$  state depending propensity function  $\{W_1, \dots, W_M\}$ . The whole system is characterized by the state vector

$$X(t) = (X_1(t), \dots, X_K(t)) = x, \quad (2.2)$$

where  $X_k(t)$  denotes the number of individuals in the state  $S_k$  at time  $t \in \mathbb{R}_{\geq 0}$  for  $k = 1, \dots, K$ . The goal is to determine the dynamic of  $X(t)$ , given that the system was in state  $X(t_0) = x_0$  at the starting time  $t_0$  (Gillespie (2007)).

In the following section 2.2.2, we establish a stochastic model, that describes key steps of the IFN system at single cell level along with intercellular communication

## 2. Stochastic modeling predicts paracrine propagation of the IFN response

through expressed IFN. To simulate a time step  $X(t) \rightarrow X(t+dt)$  of the population dynamic, we consider at time  $t$  all possible state changes of the individual cells of the population and compute the time interval  $dt$  and the state change to be realized in accordance with Gillespie's direct method (cf. section 2.2.3).

### 2.2.2. Model of virus-induced IFN signaling in single cells along with cell-to-cell communication through secreted IFN

To simulate the heterogeneous single cell dynamics of the antiviral IFN network, we develop a stochastic model for an ensemble of  $N$  individual cells communicating via released IFN.

Since the experimentally used virus cannot spread (cf. section 2.1.2 page 5), we restrict the viral activity in our model to the initial infection with subsequent virus replication and neglect reinfection. Depending on the initial infection dose, we set a fraction of cells as infected. A certain percentage of these infected cells will eventually express IFN- $\beta$  corresponding to the measured number of IFN- $\beta$ -tGFP $^+$  cells (cf. Figure 2.3). Since the MOIs used in the experiments are approximately unity or below, the number of infecting virus particles per cell is low. At the starting time  $t_0 = 0$ , we therefore randomly assign each cell  $i = 1, \dots, N$  a number of intracellular virus particles  $V_i$  according to

$$V_i(0) = \begin{cases} 0 & , \text{ if cell } i \text{ is uninfected;} \\ 1, 2 \text{ or } 3 & , \text{ if cell } i \text{ is infected.} \end{cases} \quad (2.3)$$

The state  $S_{k,i}(t)$  of a cell  $i$  at time  $t \in \mathbb{R}_{\geq 0}$  is defined by the intracellular viral load  $V_i(t)$  and the phenomenological state  $Z_{l,i}(t)$  representing the signal transduction in single cells after viral infection. To count the number of all possible states  $K$ , we utilize the index  $k = 1, \dots, K$ .

The initial condition of the model is given by the states of the cells at time zero  $S_{k,i}(0) = (Z_{l,i}(0), V_i(0))$ , whereas only the following two phenomenological states are possible at time  $t_0 = 0$ :

(Z0)  $Z_{0,i} \hat{=} \text{cell } i \text{ is uninfected}$

(Z1)  $Z_{1,i} \hat{=} \text{cell } i \text{ is virus-infected.}$

After the initial infection, the cells change their current states  $S_{k,i}(t) = (Z_{l,i}(t), V_i(t))$  and the number of cells in a state  $S_k$  at time  $t \in \mathbb{R}_{\geq 0}$ , denoted as  $X_k(t)$ , varies over time. For a compact computational description of the system that can be compared with the live-cell imaging data (cf. section 2.1.2 and 2.1.3), we choose additional phenomenological states  $Z_{l,i}$  as illustrated in Figure 2.9 and outlined under (Z2)-(Z9) below.

The investigation of the virus-induced IFN expression detected two sources of single-cell variability, firstly, the activation of latent transcription factors NF- $\kappa$ B and IRF-7 downstream of viral sensing by RIG-I (cf. Figure 2.4A and B) and, secondly,

## 2.2. Stochastic model of the IFN response against viral infection

induction of the IFN- $\beta$  gene by nuclear located NF- $\kappa$ B and IRF-7 (cf. Figure 2.4C and D). Based on the sister-cell analysis, both of these sources arise substantially from cell-intrinsic noise (cf. Figure 2.5). In the model, we thus attributed the cell-to-cell variability in IFN induction and IFN response to intrinsic stochasticity. On the one hand, both the onset of transcription factor activation and IFN- $\beta$  expression are broadly distributed among the cell population (cf. Figure 2.4D). But, on the other hand, the examination of single-cell kinetics in terms of nuclear fluorescence intensity of the transcription factors NF- $\kappa$ B as well as IRF-7 (cf. sample trajectories in Figure 2.4A) and IFN- $\beta$  fluorescence (cf. sample kinetics in Figure 2.4C) show a quantitatively steep rise once nuclear translocation and gene induction, respectively, have been triggered. To account for the switch-like activation of the transcription factors and subsequent IFN- $\beta$  expression, we describe the dynamics of these events in an individual cell  $i = 1, \dots, N$  as stochastic transitions between the following discrete states (Z1)-(Z3) along the first column in Figure 2.9 (Mariani et al. (2010)):

- (Z1)  $Z_{1,i} \equiv$  cell  $i$  is virus-infected
- (Z2)  $Z_{2,i} \equiv$  NF- $\kappa$ B/IRF is activated in cell  $i$
- (Z3)  $Z_{3,i} \equiv$  cell  $i$  secretes IFN- $\beta$ .

Furthermore, our studies expose the IFN response as an IFN- $\beta$  concentration dependent all-or-nothing switch in individual cells (cf. Figure 2.7 and Figure 2.8). To model the switch-like induction of antiviral ISGs, we simulate the IFN response as two stochastic transitions between discrete states consisting of the IFN-dependent nuclear translocation of STAT1/2 (Lillemeier et al. (2001), Vinkemeier (2004)) and the subsequent expression of ISGs, such as IRF-7. With regard to the possible combinations of the cell properties we consider the states (Z4)-(Z9) as follows (cf. middle and last column in Figure 2.9):

- (Z4)  $Z_{4,i} \equiv$  STAT1/2 is activated in cell  $i$
- (Z5)  $Z_{5,i} \equiv$  NF- $\kappa$ B/IRF and STAT1/2 are activated in cell  $i$
- (Z6)  $Z_{6,i} \equiv$  cell  $i$  secretes IFN- $\beta$  and STAT1/2 is activated
- (Z7)  $Z_{7,i} \equiv$  cell  $i$  expresses ISGs
- (Z8)  $Z_{8,i} \equiv$  cell  $i$  expresses ISGs and NF- $\kappa$ B/IRF is activated
- (Z9)  $Z_{9,i} \equiv$  cell  $i$  expresses IFN- $\beta$  and ISGs.

The transitions between the states  $S_{k,i}(t) = (Z_{l,i}(t), V_i(t))$  with  $k = 1, \dots, K$  and  $l = 0, \dots, 9$  are defined by propensity functions  $W_m$  for  $m = 1, \dots, M$ , which depend on the current state  $x$  of the system (cf. equation (2.2)). In order to make a reference to the occurring state transition, we specify the propensity functions of an individual cell  $i$  as  $w_{:,i}^\pm(x)$  and choose the following transition rates (cf. Figure 2.9):

- (1) After the initial infection the virus starts to replicate in the host cells. We simulate the replication of virus particles in the model as a birth-death process (Kendall (1949)) with the rate constant of virus replication  $r_V$  and the rate

## 2. Stochastic modeling predicts paracrine propagation of the IFN response

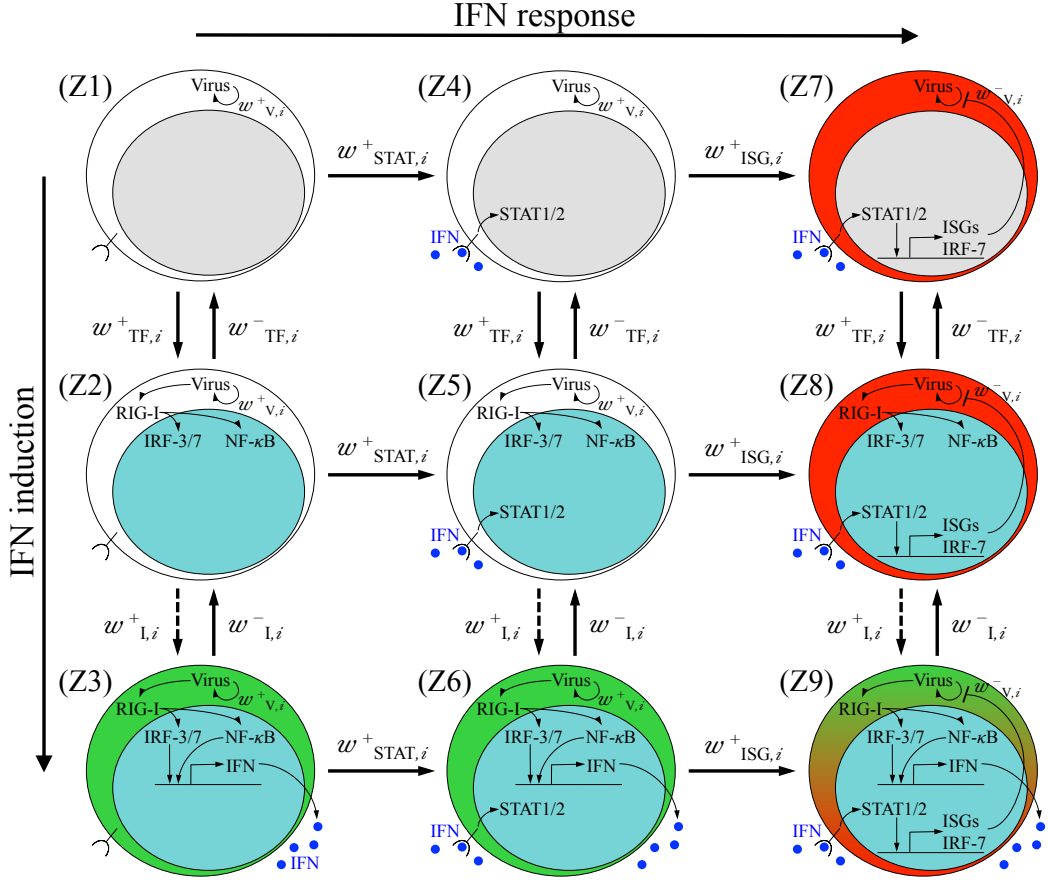


**Figure 2.9.:** A multi-scale mathematical model of IFN induction and response. The model describes an infected cell population with state transitions of individual cells according to (i) virus replication ( $\mathcal{Q}$ ), (ii) virus-induced nuclear translocation of the transcription factors IRFs/NF- $\kappa$ B (cyan nucleus), (iii) IFN- $\beta$  gene induction (green cytoplasm), (iv) nuclear translocation of STAT1/2 by extracellular IFN and (v) expression of antiviral ISGs including IRF-7 (red cytoplasm), in combination with the cell-to-cell communication via secreted IFN. Possible state changes of an individual cell  $i \in \{1, \dots, N\}$  between the discrete states (Z1)-(Z9) depend on the propensity functions  $w_{s,i}^{\pm}$  with  $s \in \{V, \text{TF}, I, \text{STAT}, \text{ISG}\}$ . The color code corresponds to the experimentally used fluorescence reporter cells (cf. section 2.1.1). Induction of IFN- $\beta$  (dashed arrow) is explicitly modeled as a multi-step process to fit the available experimental data (cf. section 2.3.2); all other state transitions are modeled as single steps (solid arrows).

constant of virus decay  $d_V$  (Figure 2.10). The associated propensity function of virus replication is specified through

$$w_{V,i}^+(x) = r_V V_i(t) \mathcal{H}(V_{\max} - V_i(t)), \quad (2.4)$$

where the Heaviside step function (Werner (2005))

$$\mathcal{H}(V_{\max} - V_i(t)) = \begin{cases} 0 & , \text{ if } V_i(t) \geq V_{\max}; \\ 1 & , \text{ if } V_i(t) < V_{\max} \end{cases} \quad (2.5)$$

is taken into account for the limited capacity of an intact cell to harbor maximal  $V_{\max}$  virus particles.

## 2.2. Stochastic model of the IFN response against viral infection

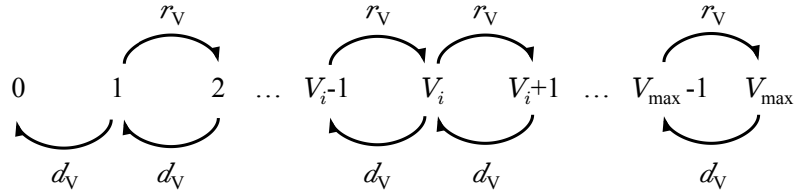


**Figure 2.10.:** Scheme of the used birth-death process to simulate virus replication. Intracellular virus particles  $V_i$  replicate in an infected cell  $i \in \{1, \dots, N\}$  with the rate constant of virus replication  $r_V$ . The maximal number of virus particles which an intact cell can harbor is defined by  $V_{\max}$ . The antiviral effect of ISG expression inhibits further viral replication and decreases the intracellular viral load with the rate constant of virus decay  $d_V$ .

- (2) The virus replication induces the activation of the transcription factors NF- $\kappa$ B as well as IRF-7. In dependence of the intracellular viral load  $V_i$ , we describe the propensity function of transcription factor (TF) activation by the Hill function

$$w_{\text{TF},i}^+(x) = k_{\text{RIG-I}} \frac{V_i(t)^{h_V}}{K_V^{h_V} + V_i(t)^{h_V}}, \quad (2.6)$$

with the half-saturation constant  $K_V$ , the Hill coefficient  $h_V$  and the rate  $k_{\text{RIG-I}}$  of RIG-I pathway activation by virus (Alon (2006)). This formulation enables a threshold response of the RIG-I pathway with saturation regarding the number of intracellular virus particle  $V_i$ . Since some reporter cells demonstrated that in the nucleus accumulated IRF-7 also returns to the cytoplasm (cf. left column in Figure 2.4A, Rand and Hauser (2010)), we allow in our model the inactivation of the RIG-I pathway with the rate

$$w_{\text{TF},i}^-(x) = l_{\text{RIG-I}}. \quad (2.7)$$

- (3) The nuclear translocation of the transcription factors NF- $\kappa$ B as well as IRF-7 leads to IFN- $\beta$  gene induction according to the propensity rate

$$w_{\text{I},i}^+(x) = k_{\text{IFN}}, \quad (2.8)$$

whereas IFN- $\beta$  expression can also terminate with the rate constant

$$w_{\text{I},i}^-(x) = l_{\text{IFN}}. \quad (2.9)$$

- (4) The experimental data show that the fraction of IFN- $\beta$  expressing cells determines the extracellular concentration of IFN- $\beta$  (cf. Figure 2.3C). Although extracellular IFN- $\beta$  decreases through the cellular uptake and degradation in the medium, IFN- $\beta$  was always detectable in the supernatant (cf. Rand and Rinias et al. (2012): Supplementary Figure S9) indicating the presence of a large number of IFN- $\beta$  molecules in the cell culture. Regarding the high diffusion coefficient of IFN (Kreuz and Levy (1965):  $D_{\text{IFN}} = 342000 \mu\text{m}^2/\text{h}$ ; Hu et al. (2011):  $D_{\text{IFN}} = 108000 \mu\text{m}^2/\text{h}$ ), diffusion on the relevant length scale of several cell diameters occurs fast within minutes compared to the hour-timescale of IFN and ISG expression. For these reasons, we consider an uniform distribution of secreted IFN in our model and calculate the extracellular concentration

## 2. Stochastic modeling predicts paracrine propagation of the IFN response

of IFN- $\beta$  in parallel with the Gillespie algorithm. We assume that IFN- $\beta$  producing cells secrete IFN- $\beta$  with the rate constant  $k_S$  and take into account a degradation of extracellular IFN- $\beta$  according to the rate constant  $d_{IFN}$ . The corresponding differential equation of the extracellular concentration of IFN- $\beta$   $I$  over time is given by

$$\dot{I}(t) = k_S N_{IFN}(t) - d_{IFN} I(t), \quad (2.10)$$

where  $N_{IFN}(t)$  stands for the number of IFN- $\beta$  expressing cells at time  $t$ .

- (5) The activation of STAT1/2 by autocrine or paracrine recognition of extracellular IFN- $\beta$   $I$  is formulated with the propensity function

$$w_{STAT,i}^+(x) = k_{STAT} \frac{I^{h_{IFN}}}{K_{IFN}^{h_{IFN}} + I^{h_{IFN}}}, \quad (2.11)$$

where  $k_{STAT}$ ,  $K_{IFN}$  and  $h_{IFN}$  denote the rate, the half-saturation constant and the Hill coefficient of STAT1/2 pathway activation by IFN, respectively.

- (6) Activated STAT1/2 in turn cause the expression of ISGs, including IRF-7, with the rate constant

$$w_{ISG,i}^+(x) = k_{ISG}. \quad (2.12)$$

As the observed number of IRF-7 expressing cells remained high within the observation period of 48 h post infection (cf. Figure 2.11B (4)), we ignore both a termination of ISG expression and an inactivation of STAT1/2.

- (7) To characterize the induction of an antiviral state through IFN response, we assume that in an ISG expressing cell  $i \in \{1, \dots, N\}$  viral replication is inhibited and the intracellular viral load  $V_i$  declines according to the propensity function

$$w_{V,i}^-(x) = d_V V_i(t), \quad (2.13)$$

where  $d_V$  denotes the rate constant of virus decay (cf. Figure 2.10).

An additional overall decline of viral load can be attributed to the death of virus-infected cells (cf. decrease of HN<sup>+</sup> cells in Figure 2.3A and B, orange color). To keep the model as simple as possible we have neglected cell death and also cell proliferation by simulating a constant cell population. The consideration of a non-growing cell population is justified since we did not detect obvious differences in heterogeneous IFN- $\beta$  induction between the cell fraction dividing during the time of observation (cf. Figure 2.5A and B) and the whole cell population which contains a sizable proportion of non-dividing cells (cf. Figure 2.4B and D).

### 2.2.3. Model simulations using Gillespie's algorithm

The simulation of our cell population model, which couples the stochastic state changes of individual cells according to the propensity functions  $w_{:,i}^\pm$  with the intercellular communication via secreted IFN- $\beta$  (cf. section 2.2.2), is performed using Gillespie's direct method.

## 2.2. Stochastic model of the IFN response against viral infection

To execute a time step of the dynamics, we consider at time  $t \in \mathbb{R}_{\geq 0}$  all possible state changes of each cell  $i = 1, \dots, N$  and calculate the time interval  $dt$  after which the next stochastic switching event takes place by

$$dt = -\frac{\ln(u_1)}{w_0}, \quad (2.14)$$

where  $u_1$  denotes an uniformly distributed random number. The denominator in (2.14) is defined as

$$w_0 = \sum_{s \in \mathcal{S}^+} \sum_{i=1}^N w_{s,i}^+(x) + \sum_{s \in \mathcal{S}^-} \sum_{i=1}^N w_{s,i}^-(x) = \sum_{m=1}^M W_m \quad (2.15)$$

with  $\mathcal{S}^+ = \{\text{V, TF, I, STAT, ISG}\}$  as well as  $\mathcal{S}^- = \{\text{V, TF, I}\}$ . The term  $w_0$  represents the sum of all propensity functions  $W_m$  for  $m = 1, \dots, M$  that “lead away” from the current state of the system.

The propensity function  $W_j$  of the actually occurring state transition at time  $t + dt$  has to fulfill the condition

$$\sum_{m=1}^{j-1} W_m < u_2 w_0 \leq \sum_{m=1}^j W_m, \quad (2.16)$$

where  $u_2$  denotes a second uniformly distributed random number.

In parallel to the Gillespie algorithm, we compute the extracellular IFN- $\beta$  concentration  $I$  by utilizing the Euler discretization of the differential equation (2.10):

$$\begin{aligned} \dot{I}(t) &= k_S N_{\text{IFN}}(t) - d_{\text{IFN}} I(t) \\ \iff \frac{d}{dt} I(t) &= k_S N_{\text{IFN}}(t) - d_{\text{IFN}} I(t) \\ \iff \frac{I(t+dt) - I(t)}{dt} &= k_S N_{\text{IFN}}(t) - d_{\text{IFN}} I(t) \\ \iff I(t+dt) &= I(t) + dt[k_S N_{\text{IFN}}(t) - d_{\text{IFN}} I(t)]. \end{aligned} \quad (2.17)$$

The application of the Euler method requires a sufficiently small time step  $dt$  that satisfies  $dt \ll d_{\text{IFN}}^{-1}$ . We found the latter condition to be guaranteed with the parameter choices (cf. Table 2.1) for our model. After every Gillespie step, we update the system in accordance with the current states of the cells. To compare the model simulations with the experimental data (Figure 2.11), we take into account the following readouts (ROs):

(RO1) The total viral load of the cell population computed by

$$V(t) = \sum_{i=1}^N V_i(t) \quad (2.18)$$

is compared with the measured mean fluorescence intensity of the HN staining (cf. Figure 2.3A) under the usage of a scaling factor.

## 2. Stochastic modeling predicts paracrine propagation of the IFN response

- (RO2) The simulated initial nuclear translocation times of the transcription factors NF- $\kappa$ B and IRF-7 after infection  $T_{\text{sig},i}, i = 1, \dots, N$  are used to fit the imaged activation times of the transcription factors  $T_{\text{sig}}$  (cf. Figure 2.4D, explicit for IRF-7 and analog for NF $\kappa$ -B as both transcription factors synchronously translocate into the nucleus (cf. Figure 2.4B)).
- (RO3) The calculated time delays between transcription factor activation and onset of IFN- $\beta$  expression  $T_{\text{gen},i}, i = 1, \dots, N$  are utilized for the estimation of the observed time spans  $T_{\text{gen}}$  of IFN- $\beta$ -tGFP switching-on times after activation of the transcription factors (cf. Figure 2.4D).
- (RO4) The number of IFN- $\beta$  expressing cells at time  $t$   $N_{\text{IFN}}(t)$  is related to the monitored IFN- $\beta$ -tGFP $^+$  reporter cells (cf. Figure 2.3B).
- (RO5) The computed extracellular IFN- $\beta$  concentration over time  $I(t)$  is compared with the experimentally quantified amount of released IFN- $\beta$ .
- (RO6) The number of ISG expressing cells at time  $t$   $N_{\text{ISG}}(t)$  represents the investigated IRF-7-mCherry $^+$  reporter cells (cf. Figure 2.7).

The determination of the model parameters is explained in detail in the next section 2.3 and results in the parameter values listed in Table 2.1. For the parameterization of our model, we focus on the extensive data for high-dose infections with 40 and 80 HAU/ml NDV (Figure 2.11). Fitting of the observed distributions regarding the NF- $\kappa$ B/IRF-7 nuclear translocation times ( $T_{\text{sig}}$ ) and the IFN- $\beta$ -tGFP switching-on times ( $T_{\text{sig}} + T_{\text{gen}}$ ) results in a good approximation of the data (Figure 2.11A) and enables the description of the measured kinetic of IFN- $\beta$ -tGFP $^+$  cells (Figure 2.11B (2)). The fits require that (i) the activation of the RIG-I-mediated signaling by virus is cooperative (cf. section 2.3.1) and (ii) IFN- $\beta$  gene induction is modeled as a multi-step process (cf. section 2.3.2). These two conclusions drawn from the parameter estimation corresponds well with experimental findings from the literature (Onoguchi et al. (2010), Ford and Thanos (2010)).

To estimate the parameters of the IFN response, we initially scale our model to the measuring unit of IFN by fitting the dose-response curve of IRF-7-expressing cells depending on external IFN- $\beta$  (cf. Figure 2.14). Restricted through this calibration and the already specified dynamics of IFN- $\beta$  producing cells (cf. Figure 2.11B (2), green curve), we determine the IFN- $\beta$  secretion rate per cell to match the observed time course of extracellular IFN (cf. Figure 2.11B (3)). With these parameters (cf. Table 2.1), the simulated kinetics of IRF-7-expressing cells agree with the data (cf. Figure 2.11B (4)).

Importantly, the model simulations demonstrate that the single-cell heterogeneity of transcription factor activation, IFN- $\beta$  gene induction as well as ISG expression translates into predictable dynamics of IFN-secreting and protected cell fractions at the population level.

## 2.2. Stochastic model of the IFN response against viral infection

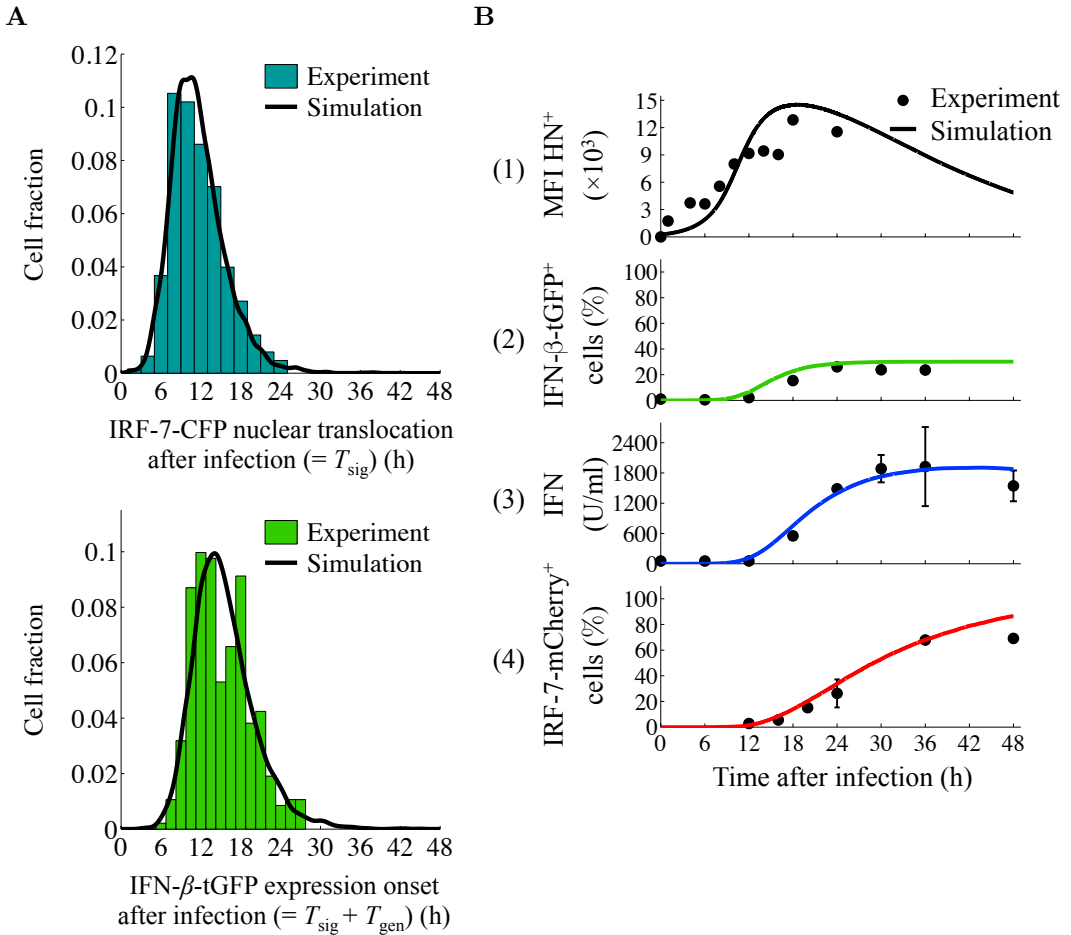


**Figure 2.11.:** Simulating the multi-layered cell-to-cell heterogeneity of the IFN system results in predictable populations dynamics. (A) Model simulations of NF- $\kappa$ B/IRF nuclear translocation time points and IFN- $\beta$ -tGFP onset times versus experimental data. With the stochastic model computed distributions (black lines) match the data of IRF-7-CFP nuclear translocation times ( $T_{\text{sig}}$ , cyan histogram) and IFN- $\beta$ -tGFP expression onset ( $T_{\text{sig}} + T_{\text{gen}}$ , green histogram) monitored in single cells after infection with 80 HAU/ml NDV (cf. Figure 2.4D for a representation of individual time points). (B) Comparison between simulated and measured cell population dynamics. The stochastic model (solid lines) reproduces the observed kinetics (dots) of (1) viral load (as measured by HN expression), (2) IFN- $\beta$ -tGFP induction, (3) extracellular IFN titre and (4) IRF-7-mCherry expression after infection with 40 HAU/ml NDV. The smooth model curves in (A) and (B) are mean values obtained by simulating  $10^4$  cells. (Experiments by Ulfert Rand, Mario Köster and Hansjörg Hauser)

## 2. Stochastic modeling predicts paracrine propagation of the IFN response

Model parameter		Value
Intracellular virus dynamics		
Maximum viral load per cell	$V_{\max}$	130
Rate constant of virus replication	$r_V$	0.34/h
Rate constant of virus decay	$d_V$	0.1/h
IFN induction		
Rate of RIG-I pathway activation by virus	$k_{\text{RIG-I}}$	0.48/h
Half-saturation constant of RIG-I pathway activation by virus	$K_V$	43
Hill coefficient of RIG-I pathway activation by virus	$h_V$	3
Rate of RIG-I pathway inactivation	$l_{\text{RIG-I}}$	0.4/h
Rate constant of IFN- $\beta$ gene induction	$k_{\text{IFN}}$	1.79/h
Rate of termination of IFN- $\beta$ expression	$l_{\text{IFN}}$	0.08/h
IFN response		
Half-saturation constant of STAT1/2 pathway activation by IFN- $\beta$	$K_{\text{IFN}}$	100 U/ml
Hill coefficient of STAT1/2 pathway activation by IFN- $\beta$	$h_{\text{IFN}}$	1
Rate of STAT1/2 pathway activation	$k_{\text{STAT}}$	0.1/h
Rate constant of ISG (IRF-7) induction by STAT1/2 pathway	$k_{\text{ISG}}$	0.1/h
Rate constant of IFN- $\beta$ secretion	$k_S$	0.13 U/h/ml/cell
Rate constant of IFN- $\beta$ degradation	$d_{\text{IFN}}$	0.15/h

**Table 2.1.:** Model parameters of the stochastic model. Based on the biological meaning of the model parameters (cf. section 2.2.2), we determined the parameter values as depicted in section 2.3. All model simulations in section 2.2.3 and 2.4 refer to this parameter set.

## 2.3. Estimation of the model parameters of the stochastic model

The Gillespie algorithm is a prevalent and valuable method to simulate stochastic processes. Nevertheless, the long computation time of this algorithm for extensive models with large time scales is a serious disadvantage (Gillespie (2007), Cao and Samuels (2009), Banks et al. (2011)). Also the simulation of our full model for a sufficient number of cells ( $N = 10^4$  cells) with dynamics over several hours is very time consuming and practically excludes straightforward optimization approaches for parameter estimation. Therefore we divide the parameter estimation problem into three parts: (1) determination of parameters for the virus-induced activation of the transcription factors IRFs/NF- $\kappa$ B (cf. section 2.3.1), (2) identification of parameters with respect to IFN- $\beta$  expression (cf. section 2.3.2) and (3) estimation of parameters concerning the IFN response (cf. section 2.3.3).

The first two parts consider the induction of IFN in individual cells without cell-to-cell communication via secreted IFN- $\beta$ . As the simulation of isolated single-cell behavior is much faster than the complete model, rigorous parameter estimation is applicable and several mechanistically relevant conclusions will be drawn from the parameter optimization.

The third part regarding ISG induction depends on the intercellular signaling between cells, which implies the need for simulating large numbers of cells and thus having impractically long calculation times. However, it turns out that we can still derive quantitative features of ISG expression from the experimental data.

An overview of the determined parameter values in this section is provided in Table 2.1 and serves as a reference for the used parameter set of all model simulations in section 2.2.3 and 2.4.

### 2.3.1. Parameter determination for the virus-induced activation of the transcription factors of IFN

In our model, we take into account the activation of the transcription factors of IFN in an infected cell  $i \in \{1, \dots, N\}$  as a state change from virus-infected to NF- $\kappa$ B/IRF-activated according to the propensity function

$$w_{TF,i}^+(x) = k_{RIG-I} \frac{V_i(t)^{h_V}}{K_V^{h_V} + V_i(t)^{h_V}},$$

with the rate constant  $k_{RIG-I}$ , the half-saturation constant  $K_V$  and the Hill coefficient  $h_V$  of RIG-I pathway activation depending on the current state  $x$  of the system (cf. equation (2.2)) and the intracellular viral load  $V_i(t)$  at time  $t \in \mathbb{R}_{\geq 0}$  (cf. Figure 2.9). A perfectly suited experiment to determine the parameters of  $w_{TF,i}^+$  is the single-cell analysis of the nuclear translocation time of NF- $\kappa$ B and IRF-7 after infection  $T_{sig}$  monitored by live-cell imaging (cf. Figure 2.4D explicit for IRF-7 and analog for NF- $\kappa$ B, since both transcription factors synchronously translocate into

## 2. Stochastic modeling predicts paracrine propagation of the IFN response

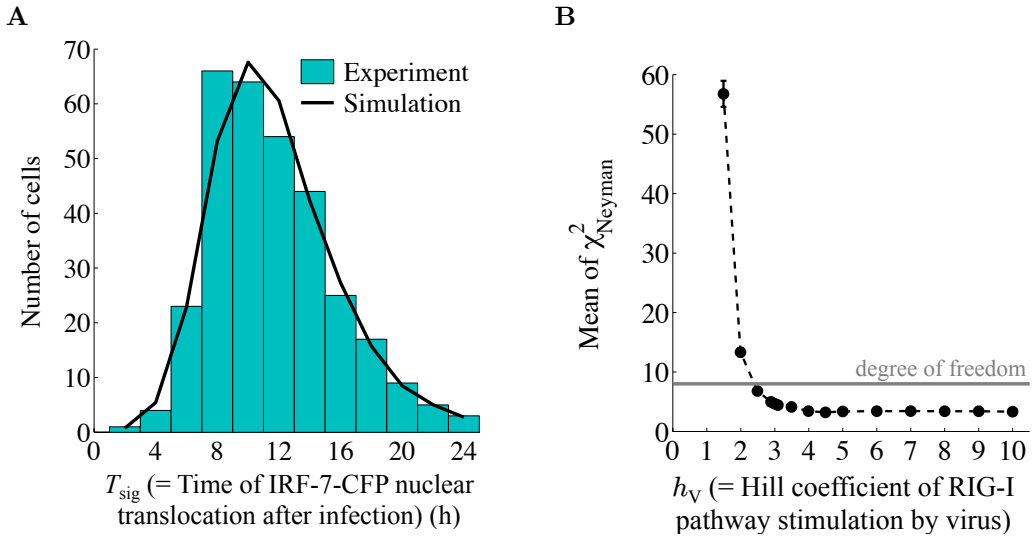


**Figure 2.12.:** Parameter determination demonstrates a cooperative induction of RIG-I mediated signaling by virus. (A) Parameter estimation of virus-induced transcription factor activation. As basis for the parameter determination serves the initial nuclear translocation time of IRF-7 monitored by live-cell imaging in 315 IRF-7-CFP reporter cells after infection with 80 HAU/ml NDV (cyan histogram, cf. Figure 2.4D for a representation of individual time points). The computed distribution (black line) is obtained by simulating  $5 \times 10^4$  runs of the mathematical submodel comprising viral replication and subsequent NF- $\kappa$ B/IRF-7 activation. A match of the computed with the measured distribution is achieved by applying the simulated annealing algorithm. (B) Profile likelihood with respect to the Hill coefficient of virus-induced RIG-I signaling  $h_V$ . The profile likelihood calculation is repeated  $10^4$  times for each fixed value of  $h_V$ . Shown are the resulting mean values and standard deviations of Neyman's chi-squares statistic. The upper limit for a good fit is defined by the degree of freedom ( $DF = 8$ , cf. (2.24)). (Experiments by Ulfert Rand, Mario Köster and Hansjörg Hauser)

the nucleus as illustrated in Figure 2.4B). To describe this measured histogram of nuclear translocation times of the transcription factors (Figure 2.12A), we utilize a submodel comprising viral replication and subsequent NF- $\kappa$ B/IRF-7 activation.

For the simulation of the submodel we initially characterize viral reproduction by comparing the model with the measured time course of viral replication after high-dose infection (cf. Figure 2.11B (1)). By setting the rate constant of virus replication  $r_V = 0.34/\text{h}$ , the maximum viral load per cell  $V_{\text{max}} = 130$  and the rate constant of virus termination  $d_V = 0.1/\text{h}$ , we receive a satisfactory match of the model with the data.

Next, we compute the distribution of NF- $\kappa$ B/IRF translocation times by simulating the submodel consisting of viral replication and subsequent NF- $\kappa$ B/IRF-7 activation sufficiently often using Gillespie's algorithm. To adjust this computed distribution to the experimentally measured histogram, we allow the parameters of the RIG-I pathway activation by virus ( $k_{\text{RIG-I}}$ ,  $K_V$  and  $h_V$ ) to vary while keeping the previously determined viral replication parameters ( $r_V$ ,  $V_{\text{max}}$  and  $d_V$ ) fix. As objective function we use Neyman's chi-squares statistic (Baker and Cousins (1984)), which considers the squared difference between the binned observed and simulated events weighted

### 2.3. Estimation of the model parameters of the stochastic model

by the inverse binned experimental data:

$$\chi^2_{\text{Neyman}} = \sum_{k=1}^B \frac{(D_k - E_k)^2}{D_k}, \quad (2.19)$$

where  $B$  denotes the number of bins of the histogram,  $D_k$  stands for the number of observed events in the  $k$ th bin and  $E_k$  represents the number of simulated events in the  $k$ th bin for  $k \in \{1, \dots, B\}$ , under the condition

$$\sum_{k=1}^B D_k = \sum_{k=1}^B E_k. \quad (2.20)$$

In order to satisfy the condition (2.20) and to ensure accuracy by simulating much more events ( $5 \times 10^4$  runs) than experimentally measured (315 cells), we calculate  $E_k$  under the usage of the cumulative distribution function (*CDF*) of the simulations for transcription factor activation at time  $t \in \mathbb{R}_{\geq 0}$  given by

$$CDF_{\text{TF}}(t) = \frac{1}{N_s} \sum_{i=1}^{N_s} \mathbb{1}_{[0;t]}(\mathcal{T}_{\text{sig},i}), \quad (2.21)$$

with the number of simulated events  $N_s$ , the simulated nuclear translocation times of the transcription factors  $\mathcal{T}_{\text{sig},i}, i = 1, \dots, N_s$  and the characteristic function  $\mathbb{1}$  of the interval  $[0; t]$

$$\mathbb{1}_{[0;t]}(\mathcal{T}_{\text{sig},i}) = \begin{cases} 1 & , \text{ for } \mathcal{T}_{\text{sig},i} \in [0; t]; \\ 0 & , \text{ for } \mathcal{T}_{\text{sig},i} \notin [0; t] \end{cases} \quad (2.22)$$

(Königsberger (2004)). After simulating the submodel  $N_s$  times, we compute the number of simulated events in the  $k$ th bin according to

$$E_k = N_{\text{data}}(CDF_{\text{TF}}(t_k^{j+1}) - CDF_{\text{TF}}(t_k^j)), \quad (2.23)$$

where  $N_{\text{data}}$  defines the number of observed data points, while  $t_k^j$  and  $t_k^{j+1}$  designate the left and the right bin edge of the  $k$ th bin for  $j \in \{1, \dots, B\}$ , respectively.

For the minimization of the objective function (2.19) we apply the simulated annealing algorithm (Schneider and Kirkpatrick (2006), Gonzalez et al. (2007)). The resulting parameter values ( $k_{\text{RIG-I}} = 0.48/\text{h}$ ,  $K_V = 43$  and  $h_V = 3.0$ ) yield a good match of computed and measured distributions of nuclear translocation times of the transcription factors (Figure 2.12A).

From a biological point of view, the most interesting feature of this parameter set is the high Hill coefficient  $h_V$ , since a Hill coefficient larger than 1 implies positive cooperativity (Murray (2002)). To analyze how robust the estimation of the Hill coefficient  $h_V$  is, we utilize the profile likelihood method (Venzon and Moolgavkar (1988)). Thus, we fix  $h_V$  systematically to different values around the estimated optimum of  $h_V = 3.0$  and refit  $k_{\text{RIG-I}}$  as well as  $K_V$  by simulated annealing. To ensure that the obtained values of the objective function (2.19) are unaffected by the inherent stochasticity of the submodel, we repeat the calculation for each fixed value of  $h_V$   $10^4$  times. The profile likelihood (Figure 2.12B) shows the corresponding mean values of Neyman's chi-squares statistic for each fixed  $h_V$ . A measure for the

## 2. Stochastic modeling predicts paracrine propagation of the IFN response

goodness of the fit is the degree of freedom ( $DF$ ), which defines an upper limit for good fits (Press et al. (2007)). In the present case, the degree of freedom is calculated by

$$\begin{aligned} DF &= B - \text{normalization constraint} - \text{number of fit parameters} \\ &= 12 - 1 - 3 \\ &= 8. \end{aligned} \tag{2.24}$$

A non-cooperative activation of the RIG-I pathway ( $h_V = 1$ ) far exceeds the degree of freedom, whereas a Hill coefficient  $h_V \geq 3$  leads to a very good fit of the translocation-time distribution. Based on these findings we conclude that the activation of the RIG-I pathway by virus is cooperative, while the available data are insufficient to estimate the precise degree of cooperativity.

After the nuclear translocation of the transcription factor IRF-7 we monitored in some reporter cells a relocation of IRF-7 back to the cytoplasm and after a while again an accumulation in the cytoplasm (cf. left column in Figure 2.4A, Rand and Hauser (2010)). To account for this nucleocytoplasmic transport of IRF-7 we allow in our model the inactivation of the RIG-I pathway with the rate  $l_{\text{RIG-I}}$ , which consequently prevents or at least delays a subsequent IFN- $\beta$  gene induction. For the adaptation of the parameter  $l_{\text{RIG-I}}$ , it is therefore necessary to simulate the whole IFN induction pathway with the determined parameter values for viral replication and RIG-I pathway activation formulated in this section and the results from the parameter estimation of IFN- $\beta$  gene induction outlined in the following section 2.3.2. After simulation of the IFN induction, we compare the arising distribution of IFN- $\beta$  switching-on times with the measured histogram (cf. Figure 2.11A, lower graph) and find an improved match by setting  $l_{\text{RIG-I}} = 0.4/\text{h}$ .

### 2.3.2. Parameter determination of the IFN expression

After the virus-induced nuclear translocation of the transcription factors NF- $\kappa$ B and IRF-7 we detected that the majority of the cells (91% at 80 HAU/ml NDV) also induces the IFN- $\beta$  gene (cf. Figure 2.4D). The time delay between nuclear translocation of IRF-7 and onset of IFN- $\beta$ -tGFP expression  $T_{\text{gen}}$  varied considerably in individual cells and resulted in a broad distribution (Figure 2.13). To simulate the heterogeneous onset of IFN- $\beta$  expression after transcription factor activation using Gillespie's algorithm, we have to formulate this state transition as a Markov process (cf. section 2.2 page 15). The only continuous distribution fulfilling the Markov property (2.1) is the memoryless exponential distribution (cf. Waldmann and Stocker (2004)). However, according to the shape of the experimentally measured histogram of  $T_{\text{gen}}$  (cf. Figure 2.13) a single exponentially distributed rate cannot generate the distinct time delay between transcription factor activation and IFN- $\beta$  gene induction. In this context it should be noted that the distribution of the transcription factor translocation times  $T_{\text{sig}}$  (cf. Figure 2.12A) can neither be modeled with a single exponential rate (cf. section 2.3.1). In the case of transcription factor activation, the time delay between infection and virus-induced signaling is explained by the viral replication process (cf. Figure 2.10).

### 2.3. Estimation of the model parameters of the stochastic model

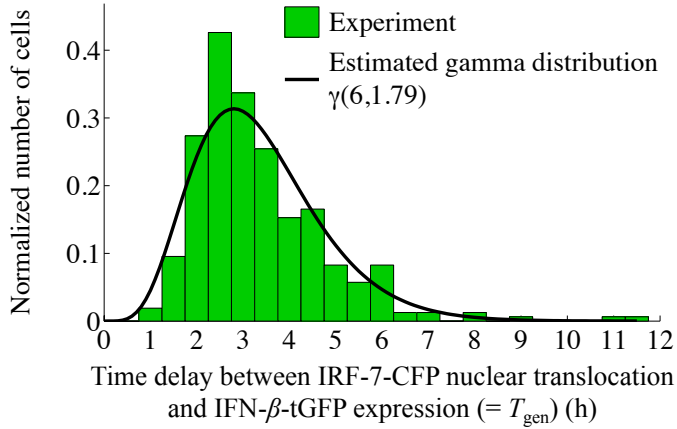


**Figure 2.13.:** Parameter estimation characterizes IFN- $\beta$  gene induction as a multi-step process. The parameter determination of IFN- $\beta$  gene induction is based on the time delay between IRF-7-CFP nuclear translocation and IFN- $\beta$ -tGFP expression ( $T_{\text{gen}}$ ) monitored by live-cell imaging in 315 dual reporter cells after infection with 80 HAU/ml NDV (green histogram, cf. Figure 2.4D for a representation of individual time points). The observed histogram can be approximated by the gamma distribution  $\gamma(6, 1.79)$  (black line), which represents a stochastic process consisting of 6 consecutive and with rate 1.79/h exponentially distributed steps. (Experiments by Ulfert Rand, Mario Köster and Hansjörg Hauser)

A possible explanation for the observed time delay between the nuclear translocation of the transcription factors NF- $\kappa$ B/IRF-7 and IFN- $\beta$  expression is the multi-step assembly of the IFN- $\beta$  enhanceosome that activates transcription from the IFN- $\beta$  promoter (Ford and Thanos (2010)). Therefore we analyze if the measured histogram of  $T_{\text{gen}}$  can be fitted with a gamma distribution  $\gamma(m, z)$ , which describes the sum of  $m$  independent and with parameter  $z$  exponentially distributed random numbers (Press et al. (2007)). Based on the measured onset times of IFN- $\beta$ -tGFP expression after transcription factor activation  $T_{\text{gen},i}$  for  $i = 1, \dots, N_{\text{data}}$  monitored in  $N_{\text{data}} = 315$  individual cells (cf. Figure 2.13), we estimate the parameters of the gamma distribution  $m$  and  $z$  with the maximum-likelihood method (Myung (2003)). For this purpose, we have to maximize the likelihood function  $L$  of our sample  $T_{\text{gen},i}$ ,  $i = 1, \dots, N_{\text{data}}$ , which is described as

$$L(p_1, \dots, p_{N_p} | T_{\text{gen},1}; \dots; T_{\text{gen},N_{\text{data}}}) = f(T_{\text{gen},1}; \dots; T_{\text{gen},N_{\text{data}}} | p_1, \dots, p_{N_p}) \quad (2.25)$$

under the usage of the assumed common density function  $f(t | p_1, \dots, p_{N_p})$  with the parameters  $p_1, \dots, p_{N_p}$  and  $t \in \mathbb{R}$ . The density function of the considered gamma distribution  $f_\gamma$  is given  $\forall m, z > 0$  by

$$f_\gamma(t | m, z) = \begin{cases} \frac{z^m}{\Gamma(m)} t^{m-1} e^{-z t} & , \text{ for } t > 0; \\ 0 & , \text{ for } t \leq 0, \end{cases} \quad (2.26)$$

with the natural exponential function  $\exp(y) = e^y, \forall y \in \mathbb{C}$  and the gamma function  $\Gamma(m)$ . According to Euler's integral representation, the gamma function is defined for  $m > 0$  as

$$\Gamma(m) = \int_0^\infty t^{m-1} e^{-t} dt. \quad (2.27)$$

## 2. Stochastic modeling predicts paracrine propagation of the IFN response

Instead of maximizing  $L$ , we prefer to maximize the log-likelihood function  $\mathcal{L}$  of our independent and identically distributed (i.i.d.) sample  $T_{\text{gen},i}$ ,  $i = 1, \dots, N_{\text{data}}$ :

$$\begin{aligned}
& \mathcal{L}(m, z | T_{\text{gen},1}; \dots; T_{\text{gen},N_{\text{data}}}) \\
&= \ln(L(m, z | T_{\text{gen},1}; \dots; T_{\text{gen},N_{\text{data}}})) \\
&\stackrel{(2.25)}{=} \ln(f_\gamma(T_{\text{gen},1}; \dots; T_{\text{gen},N_{\text{data}}} | m, z)) \\
&\stackrel{T_{\text{gen},i} \text{ i.i.d.}}{=} \ln \left( \prod_{i=1}^{N_{\text{data}}} f_\gamma(T_{\text{gen},i} | m, z) \right) \\
&\stackrel{(2.26)}{=} \ln \left( \prod_{i=1}^{N_{\text{data}}} \left[ \frac{z^m}{\Gamma(m)} T_{\text{gen},i}^{m-1} e^{-z T_{\text{gen},i}} \right] \right) \\
&= \ln \left( \left( \frac{z^m}{\Gamma(m)} \right)^{N_{\text{data}}} \prod_{i=1}^{N_{\text{data}}} [T_{\text{gen},i}^{m-1} e^{-z T_{\text{gen},i}}] \right) \\
&= N_{\text{data}} \ln \left( \frac{z^m}{\Gamma(m)} \right) + \sum_{i=1}^{N_{\text{data}}} \ln(T_{\text{gen},i}^{m-1} e^{-z T_{\text{gen},i}}) \\
&= N_{\text{data}} m \ln(z) - N_{\text{data}} \ln(\Gamma(m)) \\
&\quad + (m-1) \sum_{i=1}^{N_{\text{data}}} \ln(T_{\text{gen},i}) - z \sum_{i=1}^{N_{\text{data}}} T_{\text{gen},i}.
\end{aligned} \tag{2.28}$$

To find a maximum of the likelihood function, we first calculate the zero of the partial derivative of  $\mathcal{L}$  with respect to  $z$

$$\begin{aligned}
& \frac{\partial}{\partial z} \mathcal{L}(m, z | T_{\text{gen},1}; \dots; T_{\text{gen},N_{\text{data}}}) = 0 \\
&\stackrel{(2.28)}{\iff} N_{\text{data}} m \frac{1}{z} - \sum_{i=1}^{N_{\text{data}}} T_{\text{gen},i} = 0 \\
&\iff \frac{1}{z} = \frac{1}{N_{\text{data}} m} \sum_{i=1}^{N_{\text{data}}} T_{\text{gen},i} \\
&\iff z = \left( \frac{1}{N_{\text{data}} m} \sum_{i=1}^{N_{\text{data}}} T_{\text{gen},i} \right)^{-1},
\end{aligned} \tag{2.29}$$

which leads to an explicit estimator for  $z$  depending on  $m$  and allows to reformulate  $\mathcal{L}$  as follows:

$$\begin{aligned}
& \mathcal{L}(m, z | T_{\text{gen},1}; \dots; T_{\text{gen},N_{\text{data}}}) \\
&\stackrel{(2.29)}{=} -N_{\text{data}} m \ln \left( \frac{1}{N_{\text{data}} m} \sum_{i=1}^{N_{\text{data}}} T_{\text{gen},i} \right) - N_{\text{data}} \ln(\Gamma(m)) \\
&\quad + (m-1) \sum_{i=1}^{N_{\text{data}}} \ln(T_{\text{gen},i}) - m N_{\text{data}} \\
&= N_{\text{data}} \left[ m \ln(N_{\text{data}} m) - m \ln \left( \sum_{i=1}^{N_{\text{data}}} T_{\text{gen},i} \right) - \ln(\Gamma(m)) - m \right] \\
&\quad + (m-1) \sum_{i=1}^{N_{\text{data}}} \ln(T_{\text{gen},i}).
\end{aligned} \tag{2.30}$$

### 2.3. Estimation of the model parameters of the stochastic model

Utilizing this new formulation (2.30), the partial derivative of  $\mathcal{L}$  with respect to  $m$  is given by

$$\begin{aligned}
 & \frac{\partial}{\partial m} \mathcal{L}(m, z | T_{\text{gen},1}; \dots; T_{\text{gen},N_{\text{data}}}) \\
 = & N_{\text{data}} \left[ \ln(N_{\text{data}}m) + 1 - \ln \left( \sum_{i=1}^{N_{\text{data}}} T_{\text{gen},i} \right) - \frac{\Gamma'(m)}{\Gamma(m)} - 1 \right] + \sum_{i=1}^{N_{\text{data}}} \ln(T_{\text{gen},i}) \\
 \stackrel{(2.30)}{=} & N_{\text{data}} \left[ \ln(N_{\text{data}}m) - \ln \left( \sum_{i=1}^{N_{\text{data}}} T_{\text{gen},i} \right) - \frac{\Gamma'(m)}{\Gamma(m)} \right] + \sum_{i=1}^{N_{\text{data}}} \ln(T_{\text{gen},i}) \\
 =: & \mathcal{M}(m | T_{\text{gen},1}; \dots; T_{\text{gen},N_{\text{data}}}).
 \end{aligned} \tag{2.31}$$

Fulfilling the necessary condition for a maximum of the likelihood function concerning the partial derivative of  $\mathcal{L}$  with respect to  $m$  supplies an implicit estimate of  $m$ :

$$\begin{aligned}
 & \frac{\partial}{\partial m} \mathcal{L}(m, z | T_{\text{gen},1}; \dots; T_{\text{gen},N_{\text{data}}}) = 0 \\
 \stackrel{(2.31)}{\iff} & \mathcal{M}(m | T_{\text{gen},1}; \dots; T_{\text{gen},N_{\text{data}}}) = 0.
 \end{aligned} \tag{2.32}$$

We determine  $m$  independently from  $z$  through solving the nonlinear equation (2.32) with the trust-region-dogleg algorithm of Matlab's optimization toolbox (Coleman and Zhang (2003)). Under the usage of the measured data points  $T_{\text{gen},i}$  we receive  $m = 6.4$ . Since in the present case  $m$  is interpreted as the number of exponentially distributed steps in a stochastic process, we round  $m$  to the nearest integer. Inserting  $m = 6$  in (2.29) yields directly  $z = 1.79/\text{h}$ . The resulting gamma distribution  $\gamma(6, 1.79)$  provides a good approximation of the measured histogram of  $T_{\text{gen}}$  (cf. Figure 2.13). Therefore we conclude that IFN- $\beta$  expression after transcription factor activation can be described through 6 consecutive and with rate  $k_{\text{IFN}} = 1.79/\text{h}$  exponentially distributed steps. Consequently, each of these first-order processes has a half-life of  $\ln(2)/k_{\text{IFN}} = 23 \text{ min}$ . The estimated number of steps and the half-life correspond well with the mechanistic knowledge about the multi-step formation of the IFN- $\beta$  enhanceosome (Ford and Thanos (2010)), although transcription and translation might also contribute relevant steps.

In addition, we have observed that the activated transcription factors NF- $\kappa$ B and IRF-7 stay in average for  $\sim 13 \text{ h}$  in the nucleus (Rand and Hauser (2010)). This mean duration provides an upper limit for the average time span of IFN production, since IFN expression requires the stimulus of nuclear-located transcription factors. Accordingly, we fix the rate of termination of IFN- $\beta$  expression to  $l_{\text{IFN}} = 0.08/\text{h}$ .

## 2. Stochastic modeling predicts paracrine propagation of the IFN response

### 2.3.3. Parameter determination of the IFN response

With the intention to obtain quantitative insight into IFN-induced ISG regulation, we have a closer look on the performed IRF-7 response experiment, in which the IRF-7-mCherry reporter cells were stimulated with increasing units of IFN- $\beta$  and subjected to flow cytometry at different times after stimulation (cf. Figure 2.7). On the basis of this experiment, we derive a dose-response data set by taking into account the maximal fraction of IRF-7-mCherry $^+$  cells for each applied IFN- $\beta$  concentration (Figure 2.14). The hyperbolic shape of the derived data set indicates that the dose-response can be characterized by a Hill function

$$R(I) = \frac{I^{h_{\text{IFN}}}}{K_{\text{IFN}}^{h_{\text{IFN}}} + I^{h_{\text{IFN}}}}, \quad (2.33)$$

where  $K_{\text{IFN}}$  and  $h_{\text{IFN}}$  denote the half-saturation constant and the Hill coefficient of STAT1/2 pathway activation by IFN- $\beta$ , respectively.

To fit the parameters of the Hill function to the dose-response data set, we utilize the trust-region-reflective least-squares algorithm of Matlab's optimization toolbox (Coleman and Zhang (2003)). The least-squares method is based on the chi-squares statistic

$$\chi^2 = \sum_{i=1}^{N_{\text{data}}} \left( \frac{d_i - y(x_i | p_1, \dots, p_M)}{\sigma_i} \right)^2, \quad (2.34)$$

with the number of observed data points  $N_{\text{data}}$ , the measured data set  $(x_i, d_i)$ , the corresponding measurement error  $\sigma_i$  for  $i = 1, \dots, N_{\text{data}}$  and the objective function  $y(x_i | p_1, \dots, p_M)$  at  $x_i$  with  $M$  adjustable parameters  $p_j$  for  $j = 1, \dots, M$  (Press et al. (2007)). In order to find the best fit parameter values, the chi-squares statistic  $\chi^2$  has to be minimized.

In the present optimization problem, we consider (2.33) as objective function to describe the derived dose-response data set by assuming a measurement error of 10%. The resulting parameter values  $K_{\text{IFN}} = 100.8 \text{ U/ml}$  and  $h_{\text{IFN}} = 1.08$  yield a satisfying fit to the data (cf. Figure 2.14, black curve). For simulations of the full model we use whole numbers and set  $K_{\text{IFN}} = 100 \text{ U/ml}$  as well as  $h_{\text{IFN}} = 1$  (cf. Figure 2.14, red curve). The description of the IFN-induced response data by a Hill coefficient with value 1 implies a non-cooperative IRF-7 induction through extracellular IFN- $\beta$  (Murray (2002)).

In contrast to the dose-response parameters  $K_{\text{IFN}}$  and  $h_{\text{IFN}}$ , the rate constants for STAT1/2 activation and ISG induction cannot be rigorously fitted from the available data. By comparing the simulated kinetic of ISG expression to the experimentally measured one at high viral load (cf. Figure 2.11B (4)), we detect that  $k_{\text{STAT}} = k_{\text{ISG}} = 0.1/\text{h}$  leads to a good match between model and data.

For the determination of the IFN- $\beta$  secretion rate  $k_S$  and the IFN- $\beta$  degradation rate  $d_{\text{IFN}}$ , we use the measured kinetics of IFN- $\beta$ -tGFP expressing cells and the amount of released IFN after high-dose infection (cf. Figure 2.11B (2) and (3)). Using the preceding parameterization of the IFN- $\beta$  induction (cf. section 2.3.1 and 2.3.2) enables the description of the IFN- $\beta$ -tGFP $^+$  cell fraction over time. Restricted

### 2.3. Estimation of the model parameters of the stochastic model

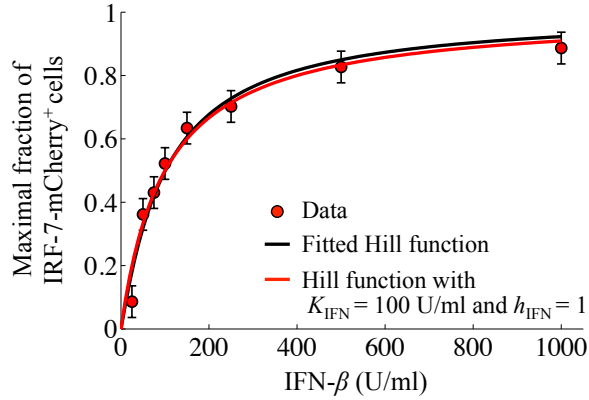


**Figure 2.14.:** Parameter estimation reveals a non-cooperative induction of IRF-7 by extracellular IFN- $\beta$ . Based on the IRF-7 response measurement (cf. Figure 2.7), we derive a dose-response data set (red dots) by considering the maximal fraction of IRF-7-mCherry<sup>+</sup> cells (y-axis) for each applied IFN- $\beta$  concentration (x-axis). The data was fitted with a Hill function (black curve) by applying a trust-region-reflective least-squares algorithm and assuming the indicated 10% measurement error (black error bars). For further simulations we set the fitted parameter values to the whole numbers  $K_{\text{IFN}} = 100 \text{ U/ml}$  and  $h_{\text{IFN}} = 1$  (red curve). (Experiments by Ulfert Rand, Mario Köster and Hansjörg Hauser)

by the kinetic of the IFN- $\beta$ -producing cells and the already adjusted measurement unit of IFN through fitting  $K_{\text{IFN}} = 100 \text{ U/ml}$ , we find that  $k_S = 0.13 \text{ U}/(\text{h ml cell})$  and  $d_{\text{IFN}} = 0.15/\text{h}$  lead to a good agreement between the measured and simulated dynamic of extracellular IFN.

2. Stochastic modeling predicts paracrine propagation of the IFN response

## 2.4. Stochastic modeling exposes individual IFN producers as sentinels of viral infection

The temporal dynamics of IFN- $\beta$ -tGFP expressing cells and IRF-7-mCherry responding cells after infection with high viral load (cf. Figure 2.11 (2) and (4)) suggest that IFN- $\beta$  secreted by a single cell can induce antiviral ISG production in several cells. To analyze this presumption more closely, we simulate the stochastic model for a range of low-dose infections, where IFN- $\beta$ -producing cells are rare. The subsequent comparison of the predicted kinetics of IFN-responding cells with the measured fraction of ISG-expressing cells shows a good match with the associated data (Figure 2.15A).

In addition, we consider the proportion of IFN responding cells to IFN producing cells after infection with different virus titers (Figure 2.15B). For low-dose infections, the model predicts a strong paracrine propagation of antiviral protection through secreted IFN, with up to 40 times as many ISG-expressing cells than IFN-secreting cells. This model prediction proved remarkably accurate when tested experimentally, given that the model is calibrated only for high dose infections (cf. Figure 2.15B blue square and Figure 2.11).

To further examine the relation between IFN expressing and IFN responding cells, we cultivated IFN- $\beta$ -tGFP reporter cells together with IRF-7-mCherry cells (Figure 2.16A). Indeed, we detected that few IFN- $\beta$ -tGFP expressing cells can activate ISG

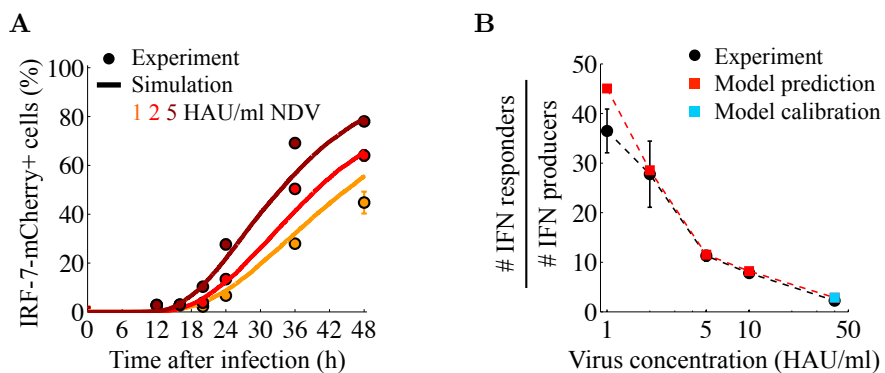


**Figure 2.15.**: Paracrine propagation of the IFN response is predicted by the model and verified experimentally. (A, B) After the model parameterization based on experimental data concerning high dose infections, we simulate the model for low dose infections by taking into account a population of  $10^4$  cells. (A) The model predicts IFN response dynamics after low-dose infections. The simulated kinetics of ISG expressing cells (solid curves) can be confirmed by the measured dynamics of IRF-7-mCherry<sup>+</sup> cells (dots) for sparse infections with 1, 2 and 5 HAU/ml NDV. (B) Predicted paracrine propagation of the IFN response induced by individual sentinels. Shown is the proportion of IFN responding cells to IFN producing cells (y-axis) after infection with different viral doses (x-axis) for an infection period of 48 h. The blue square denotes the model calibration (cf. Figure 2.11), while the red squares represent the predictions of the model regarding low-dose infections. The subsequent verification of the model predictions by experimental data is marked by the black dots. (Experiments by Ulfert Rand, Mario Köster and Hansjörg Hauser)

## 2.4. Stochastic modeling exposes IFN producers as sentinels of viral infection

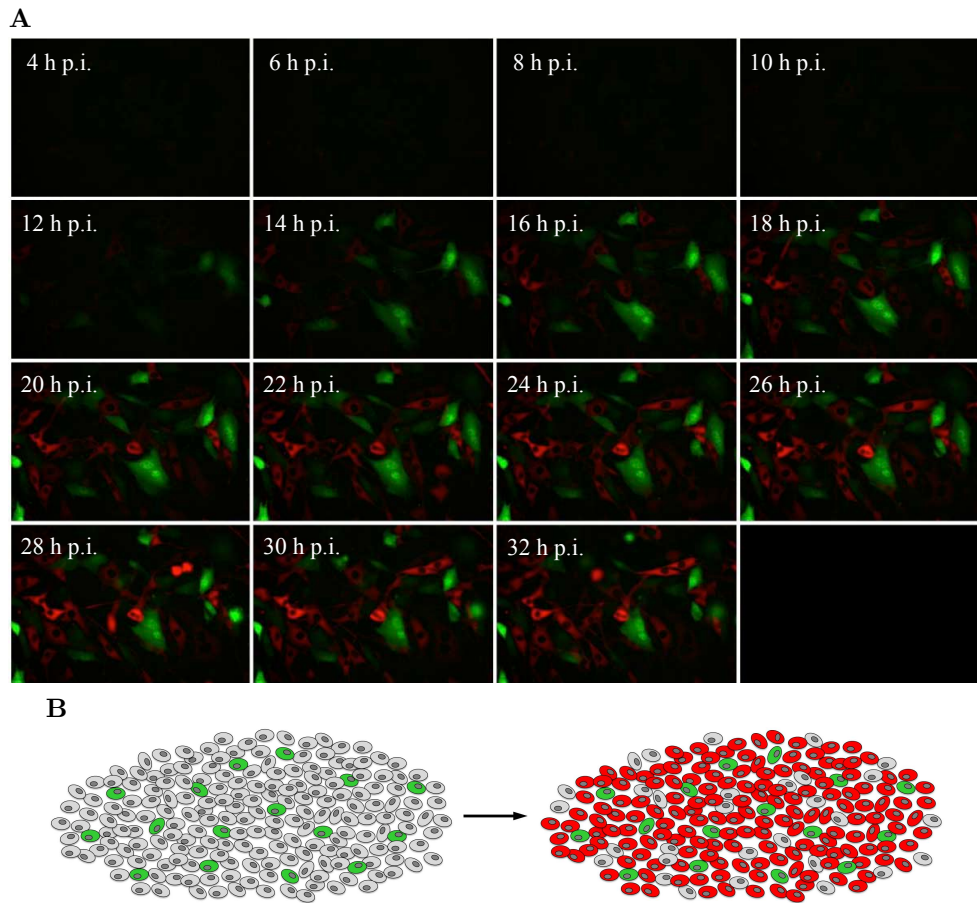


**Figure 2.16.:** Illustrations of the predicted paracrine response communication based on our study of the antiviral IFN system regarding primary infections. (A) Co-culturing of IFN- $\beta$ -tGFP and IRF-7-mCherry reporter cells illustrates paracrine communication. IFN- $\beta$ -tGFP reporter cells (green cells) were infected with 40 HAU/ml NDV for 1 h. After this infection period IRF-7-mCherry cells (red cells) were added at same density and cells were subjected to time-lapse microscopy. Merged fluorescent pictures for IFN- $\beta$ -tGFP and IRF-7-mCherry at indicated time points post infection (p.i.) are shown. (B) Scheme of the assumed protective function of IFN-producing cells. In consideration of our study of the IFN network, we suggest that few IFN- $\beta$  expressing cells (green cells) can induce an antiviral gene program in a large number of neighboring cells (red cells) to limit viral spread. (Experiments by Ulfert Rand, Mario Köster and Hansjörg Hauser)

expression in many neighboring IRF-7-mCherry cells. This observation corroborates the predicted paracrine amplification of the IFN signal (Figure 2.16B).

Based on our study of the antiviral IFN system regarding primary infections we assume that the paracrine propagation of the IFN response transforms stochastic single-cell behavior into efficient and predictable antiviral protection of the cell population. Accordingly, a few IFN-producing cells might suffice as sentinels of viral infection to protect a large number of cells surrounding the infection site (Rand and Rinas et al. (2012)).

2. Stochastic modeling predicts paracrine propagation of the IFN response

### 3. Population-based modeling reveals major control of viral fitness by the antiviral effect of IFN on already infected cells

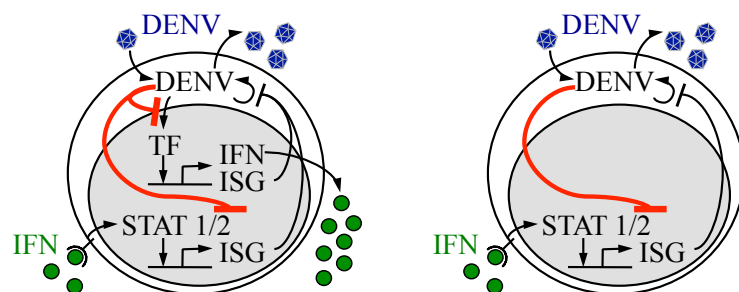


**Figure 3.1.:** Scheme of the countermeasures of DENV to interfere IFN production and IFN-induced signaling. (○)

3. Viral fitness is mainly controlled by the effect of IFN on already infected cells

### 3.1. Dissecting the dynamics of IFN-induced antiviral defense against spreading DENV in living cells

#### 3.1.1. Detection of the immediate interactions between DENV infection and the antiviral IFN response at single-cell level

Previous research on DENV have described the viral replication process (Lindenbach (2007), Bartenschlager and Miller (2008), Welsch et al. (2009), Kumar et al. (2013)), the propagation properties under the influence of IFN stimulation (Diamond et al. (2000), Jones et al. (2005)) or the interference with antiviral IFN target genes (Schoggins et al. (2012)) primarily under steady-state conditions. But an investigation of the direct interactions between DENV infection and the antiviral IFN response in individual cells has been missing. To address this lacking single-cell system our cooperation partners Bianca Schmid and Ralf Bartenschlager from the Department of Infectious Diseases at the University of Heidelberg have established both a fully viable DENV reporter and IFN-competent fluorescent reporter cells (Schmid (2014)).

For the visualization of DENV replication and spread our collaboration partners constructed a genetically modified DENV reporter virus expressing the far red fluorescent protein TurboFP635 “faR” (Figure 3.2A). This DENV-faR-wt reporter construct is based on the DENV serotype 2 (isolate 16681), which is an enveloped in positive-sense single-stranded RNA virus (Fischl and Bartenschlager (2013)). The DENV genome encodes 3 structural proteins, the capsid (C), the premembrane protein (prM) as well as the envelope protein (E) and 7 non-structural (NS) proteins (NS1, NS2A, NS2B, NS3, NS4A, NS4B, and NS5) (Chambers and Rice (1987), Bartenschlager and Miller (2008), Kumar et al. (2013), Acosta et al. (2014)). While the structural proteins and the RNA genome form the infectious virus particle, the non-structural proteins are required for RNA replication which takes place in the cytoplasm in close association with intracellular membranes (Welsch et al. (2009), Peña and Harris (2012)). During the replication process of the DENV-faR-wt construct, the integrated faR fluorescent protein accumulates in the nucleus as the capsid sequence contains a nuclear localization signal (NLS) (Figure 3.2B and C).

In order to study the interplay of DENV infection with the IFN system in real time at single-cell level, Bianca Schmid and Ralf Bartenschlager generated IFN-competent fluorescent reporter cell lines to monitor the virus-triggered signal transduction and the induction of distinct ISGs (Figure 3.2B and C). After infection, the sensing of virus by the intracellular receptor RIG-I leads to the nuclear translocation of the transcription factors NF- $\kappa$ B, IRF-3 as well as IRF-7 (Chang et al. (2006), Brennan and Bowie (2010)). For the detection of transcription factor activation, reporter cells were labeled with the fluorescent marker IRF-3-eGFP under the usage of the enhanced green fluorescence protein (eGFP) (cf. Figure 3.2B and C, in cyan color to clearly distinguish IRF-3-eGFP from other GFP markers). In the nucleus located transcription factors result in the expression of IFN and according to findings from the literature (Grandvaux et al. (2002), Diamond and Farzan (2013)) also some ISGs including the IFN-induced protein with tetratricopeptide repeats 1 (IFIT1,

### 3.1. Dissecting the dynamics of IFN-induced antiviral defense against DENV

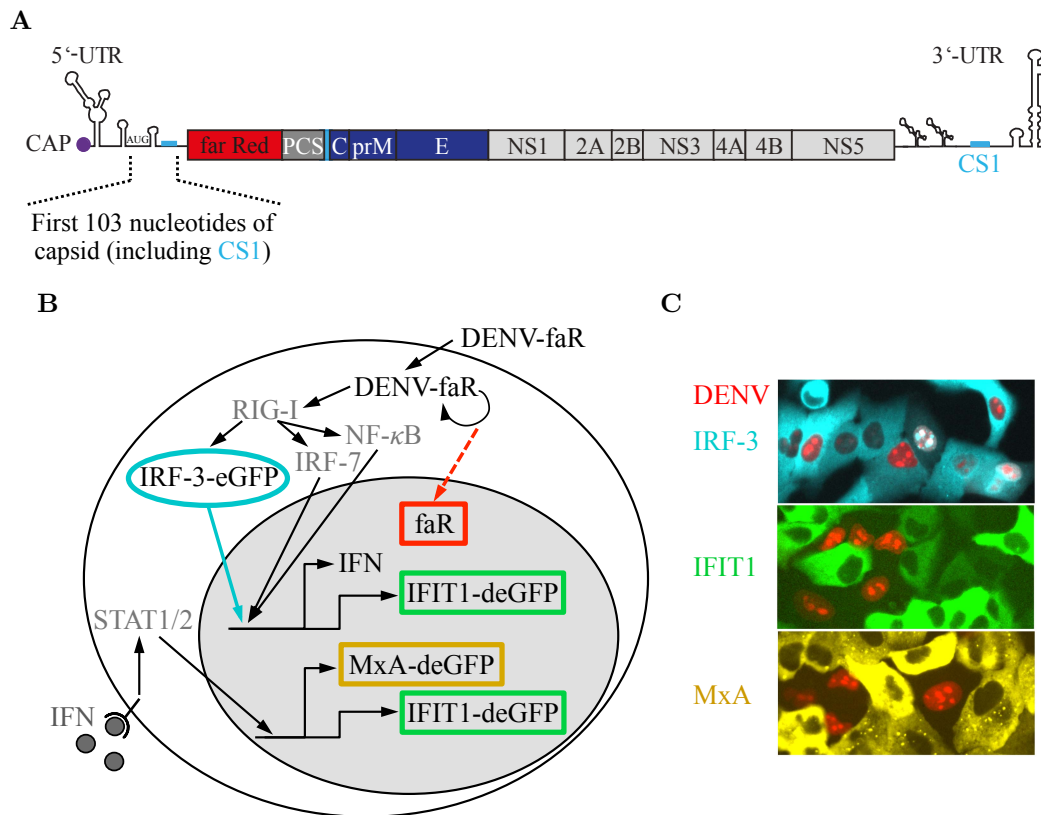


**Figure 3.2.:** The immediate interactions between DENV infection and the antiviral IFN response can be monitored in real time with generated fluorescence reporter constructs. (A) Scheme of the established DENV-faR-wt reporter virus construct. The first 103 nucleotides of the capsid coding sequence of DENV-wt contain the circularization sequence 1 (CS1), which is essential for DENV RNA replication. Thus, the virologists duplicated the first 103 nucleotides of the capsid sequence and inserted them at the 5' end of the reporter gene. The far red reporter is fused N-terminally with amino acid residues of the capsid protein, that contains a NLS, and C-terminally with the sequence encoding for the 2A cleavage factor of the Thosea asigna virus (PCS) to generate the authentic N-terminus of the capsid protein. The adjacent polyprotein can be cleaved into 3 structural proteins (capsid (C), premembrane protein (prM) as well as envelope protein (E)) and 7 non-structural (NS) proteins (NS1, NS2A, NS2B, NS3, NS4A, NS4B, and NS5) by viral and cellular proteases during the viral replication process. (B, C) Scheme and fluorescence pictures of the created intracellular reporter constructs. Infection with DENV-faR becomes visible through the nuclear accumulation of the faR fluorescence protein in virus replicating cells (yellow nucleus). Subsequent viral sensing through RIG-I causes the translocation of the latent fusion protein IRF-3-eGFP (cyan cytoplasm) into the nucleus (cyan nucleus). Activated transcription factors induce the expression of IFN and as recorded in the literature also some ISGs including IFIT1. The recognition of extracellular IFN stimulates the production of further ISGs such as IFIT1 and MxA. ISG expression is illustrated by the BAC constructs IFIT1-deGFP (green cytoplasm) and MxA-deGFP (yellow cytoplasm). (Experiments by Bianca Schmid and Ralf Bartenschlager)

also known as ISG56). The recognition of extracellular IFN induces the expression of further ISGs such as IFIT1 and MxA. To visualize the expression of ISGs that are expressed together with IFN as well as in response to IFN, the virologists transfected

### 3. Viral fitness is mainly controlled by the effect of IFN on already infected cells

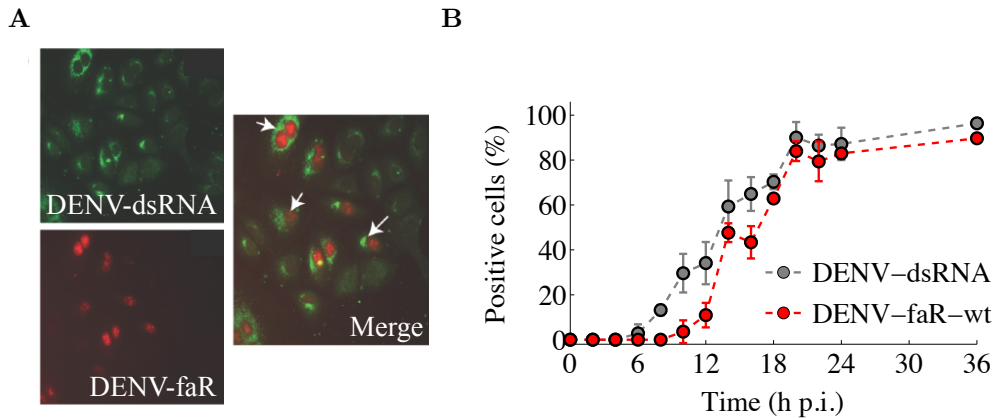


**Figure 3.3.:** The generated DENV-faR-wt reporter is a reliable marker to detect DENV replication dynamics in individual cells. (A, B) A549 cells were infected with DENV-faR-wt at a MOI of 10 and analyzed by immunofluorescence assay under the usage of the faR fluorescence protein or dsRNA-specific antibodies. (A) Strong correlation between faR fluorescence protein and dsRNA in a given host cell. Selected immunofluorescence pictures of DENV-dsRNA (top left in green color) and DENV-faR (bottom left in red color) individually or combined (right) at 14 h post infection demonstrate correlated presence of both markers in a given host cell. (B) Similar dynamics of faR protein and dsRNA expression. The fraction of dsRNA (gray color) or faR protein (red color) positive cells was determined post infection (p.i.) via ImageJ cell counter plugin. Shown are the mean values and standard deviations of two independent measurements. (Experiments by Bianca Schmid and Ralf Bartenschlager)

cells with a BAC encoding for a fusion protein composed of IFIT1 and a destabilized version of the enhanced green fluorescent protein (deGFP) (cf. Figure 3.2B and C, green color). Another BAC-based reporter construct MxA-deGFP was created to detect the expression of MxA which exclusively occurs in response to extracellular IFN (Bandyopadhyay et al. (1995)) (cf. Figure 3.2B and C, in yellow color for a better comparison of MxA-deGFP with other GFP markers).

All reporter constructs were stably transfected into carcinomic human alveolar epithelial cells (A549), since A549 cells are permissive for DENV, able to produce IFN and capable to activate an IFN-stimulated antiviral gene program (Schmid (2014)). While endogenous IFIT1 and MxA proteins have a half-life of more than 12 h, we observed for our deGFP reporter cells short half-lives of ~ 2 h for IFIT1-deGFP and ~ 4 h for MxA-deGFP (Schmid (2014)). The reduction of the half-lives due to destabilized reporter proteins enables a more precise characterization of the dynamics of the IFN response. Furthermore, infection of the three reporter cell lines IRF-3-eGFP, IFIT1-deGFP or MxA-deGFP with the generated DENV-faR-wt is a perfect tool for live-cell dual-color imaging of virus replication indicated by the red nucleus and latent IRF-3, IFIT1 or MxA expression appearing in the cytoplasm of individual cells over time.

To examine how accurate the constructed DENV reporter reflects viral replication, we directly compared our faR protein marker with the well-established DENV double-stranded RNA (dsRNA) indicator for active virus replication in the same cell after infection with a high dose of DENV-faR-wt (Figure 3.3). The subsequent

### 3.1. Dissecting the dynamics of IFN-induced antiviral defense against DENV

immunofluorescence analysis showed a strong correlation between the appearance of the faR fluorescence protein and the production of dsRNA in a given host cell (cf. Figure 3.3A). Following the heavily infected cell population resulted in similar kinetics of faR protein and dsRNA expression with only a slightly delayed detection of the faR protein marker (cf. Figure 3.3B). These data demonstrate that the DENV reporter is a reliable marker to study the dynamics of DENV replication at single-cell level.

Apart from verifying the reliability of the created DENV-faR-wt reporter to monitor viral replication we also characterized the propagation properties of our DENV reporter construct. First we investigated whether DENV-faR-wt infected cells produce a comparable amount of infectious virus particles as DENV-wt infected cells. The release of infectious virus particles was quantified by performing a limiting dilution assay to determine the tissue culture infectious dose 50 (TCID<sub>50</sub>) per milliliter (ml), where TCID<sub>50</sub> is the dilution which infects 50% of replicate cell cultures (Lindenbach et al. (2005)). The corresponding TCID<sub>50</sub> titers were calculated by applying the widely used method of Spearman and Kärber (Hierholzer et al. (1996)). The resulting extracellular virus titers after DENV-faR-wt was indistinguishable from DENV-wt, as the marginally lower virus production of the DENV reporter lies in the range of possible measurement variations of the approximative TCID<sub>50</sub> assay (Figure 3.4A). DENV-faR-wt is thus well suited to analyze the release of new viral particles.

Moreover, we examined if our DENV reporter efficiently spreads in IFN-competent A549 cells by comparing DENV-faR-wt with DENV-faR trans-complementation particle (TCP) infection. TCPs are particles which contain no genetic information to encode the structural proteins C, prM and E. While TCPs are able to enter host cells and replicate the viral genome, they cannot spread as the missing structural proteins are necessary to form infectious virus particles (Lai et al. (2008)). To produce infectious DENV-faR TCPs we transfected cells with a DENV-faR replicon construct that lacks the structural proteins C, prM as well as E and provided the structural proteins in trans by protein overexpression (Figure 3.4C (1)). The subsequent infection of targeting cells with the non-spreading DENV-faR TCPs enables the investigation of single round infections (Figure 3.4C (2)). The comparison of DENV-faR TCP and DENV-faR-wt infected cells showed an almost constant fraction of DENV-faR TCP positive cells over time, whereas the number of DENV-faR-wt positive cells grew steadily (Figure 3.4B). These data demonstrate that the DENV-faR-wt reporter efficiently spreads in an IFN-competent cell system.

Taken together, the established DENV-faR-wt reporter is a reliable tool to observe the dynamics of viral replication, virus production and viral spread. Additionally, the infection of the stable reporter cell lines IRF-3-eGFP, IFIT1-deGFP or MxA-deGFP with DENV-faR-wt allows the investigation of the immediate interactions between DENV infection and the antiviral IFN response at single-cell level.

3. Viral fitness is mainly controlled by the effect of IFN on already infected cells

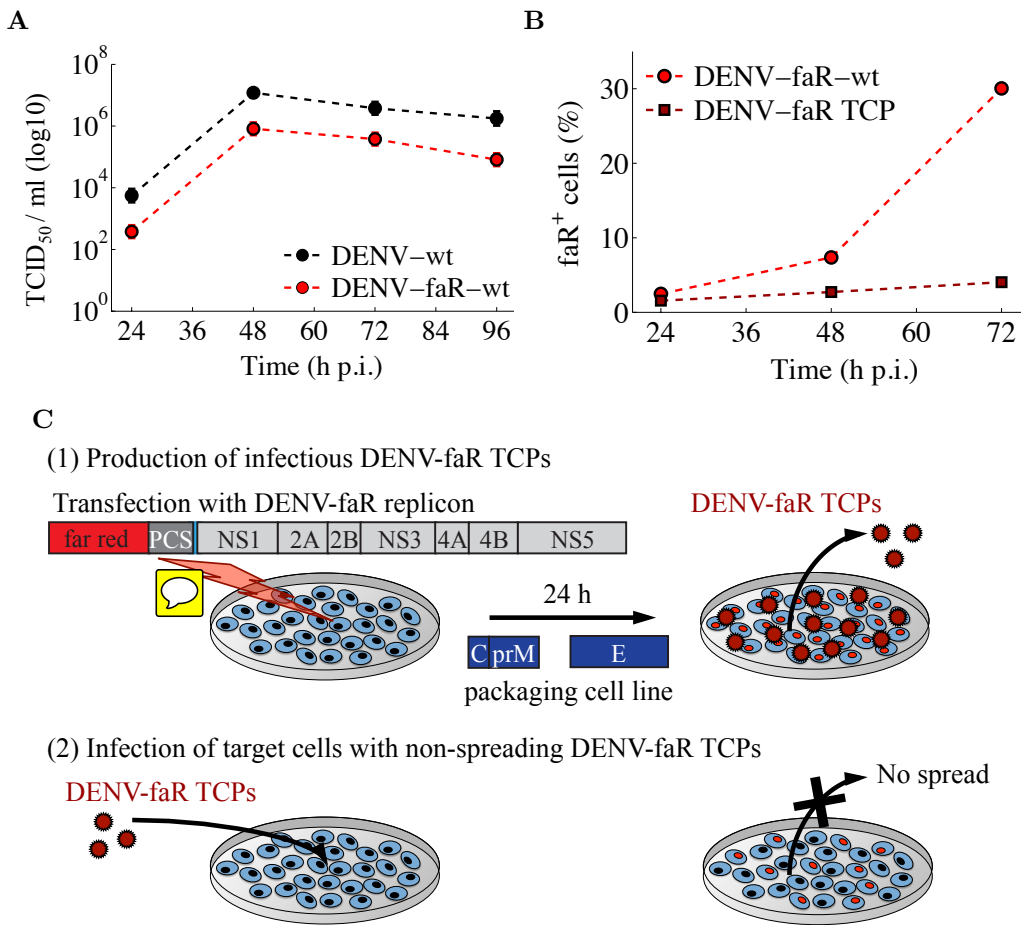


**Figure 3.4.:** The established DENV-faR reporter efficiently spreads in IFN-competent cells. (A) Virus production of DENV-faR-wt complies with the viral release of DENV-wt. A549 cells were infected with DENV-wt (black color) or DENV-faR-wt (red color) at a MOI of 1. At the indicated time points post infection (p.i.) we measured the virus titers in the supernatant by performing a limiting dilution assay to determine the tissue culture infectious dose 50 (TCID<sub>50</sub>) per milliliter (ml). (B) DENV-faR-wt propagates successfully in an IFN-competent cell system. A549 cells were infected with virus producing DENV-faR-wt (red color; virus production shown in (A)) or with non-spreading DENV-faR TCP (dark red color; cf. TCP system in (C)) at a MOI of 0.1. The fraction of faR positive cells was detected at three time points after infection by flow cytometry. (C) Scheme of the TCP system. (1) Infectious DENV-faR TCPs were produced by transfecting cells with a DENV-faR replicon construct which lacks the structural proteins C, prM as well as E and providing these structural proteins in trans by protein overexpression. DENV-faR TCPs (dark red circles) containing cell culture supernatant was harvested 24 h later. (2) DENV-faR TCPs are unable to spread in cell cultures, as these particles cannot encode the required structural proteins C, prM and E by themselves. Thus, infection of targeting cells with DENV-faR TCPs only leads to a single round infection. (Experiments by Bianca Schmid and Ralf Bartenschlager)

### *3.1. Dissecting the dynamics of IFN-induced antiviral defense against DENV*

#### **3.1.2. The competition between spreading DENV and IFN-induced antiviral protection**

The competition between DENV and the antiviral IFN system is characterized, on the one hand, by the virus-induced IFN expression followed by strong antiviral IFN response and, on the other hand, by the countermeasures of DENV to disturb IFN production as well as IFN-induced signaling (cf. Figure 3.1). To analyze the strength of the IFN-induced antiviral protection, we stimulated IFN-competent A549 cells prior, at or post DENV infection with IFN. We used a high viral dose to ensure a large number of primary infected cells and measured the fraction of DENV-wt positive cells 24 h post infection (Figure 3.5A and B). IFN pre-treatment enables a temporal advance to initiate the antiviral IFN response and resulted in a remarkable decrease of infected cells compared to the analog experiment without IFN stimulation (cf. Figure 3.5B black horizontal line). The comparison of lacking IFN treatment and stimulation with IFN at or post infection yielded a significantly reduced number of infected cells due to IFN treatment up to 6 h after infection. While the IFN pre-stimulation experiments demonstrate a protective effect of IFN against DENV infection, the IFN post-treatment measurements indicate a reduction of viral replication in infected cells through recognition of IFN in a certain time window post infection.

Findings from the literature describe that DENV is able to disturb IFN-induced signaling by STAT2 degradation (Jones et al. (2005), Ashour et al. (2009), Mazzon et al. (2009). Morrison et al. (2013)). To examine this proposed countermeasure of DENV in our system we related the dynamics of DENV replication directly with STAT2 expression. For this purpose, we infected A549 cells with DENV-wt and quantified simultaneously the DENV envelop and STAT2 protein levels over time by Western blot analysis (Figure 3.6). In agreement with other reports (Jones et al. (2005)), the Western blot analysis showed already after 6 h post infection a rapid decrease of STAT2. Approximately 20 h later STAT2 levels increased again, which might be due to ISG expression in response to secreted IFN or limitation of viral spread by IFN-induced protection of naïve cells in the meantime. Nevertheless, the dynamic of STAT2 expression after infection illustrates the impairment of the IFN response by DENV replication.

In order to obtain more insight in the properties of DENV with respect to viral replication, virus production and immune activation, we utilized the classical method for the determination of single-step growth curves (Ellis and Delbrück (1939), Gong et al. (1996)). Therefore, we infected A549 cells with our DENV-faR reporter (cf. Figure 3.2) at a high viral dose and measured in short time frames viral RNA, virus release, ISG56 mRNA expression and IFN- $\lambda$  production (Figure 3.7). The initial high level of detected viral RNA and extracellular virus is due to added DENV particles which stick to the cell surface and sustained the thoroughly performed multiple washing steps. Regarding the residual DENV particles bound on the cells, the first RNA replication occurred roughly 8 h p.i. and increasing viral RNA levels saturated 48 h p.i.. New infectious virus particles were released approximately between 14-36 h after infection. The subsequent decrease of extracellular virus can probably be attributed to exhausted or dying infected cells. In agreement with the dynamics of

3. Viral fitness is mainly controlled by the effect of IFN on already infected cells

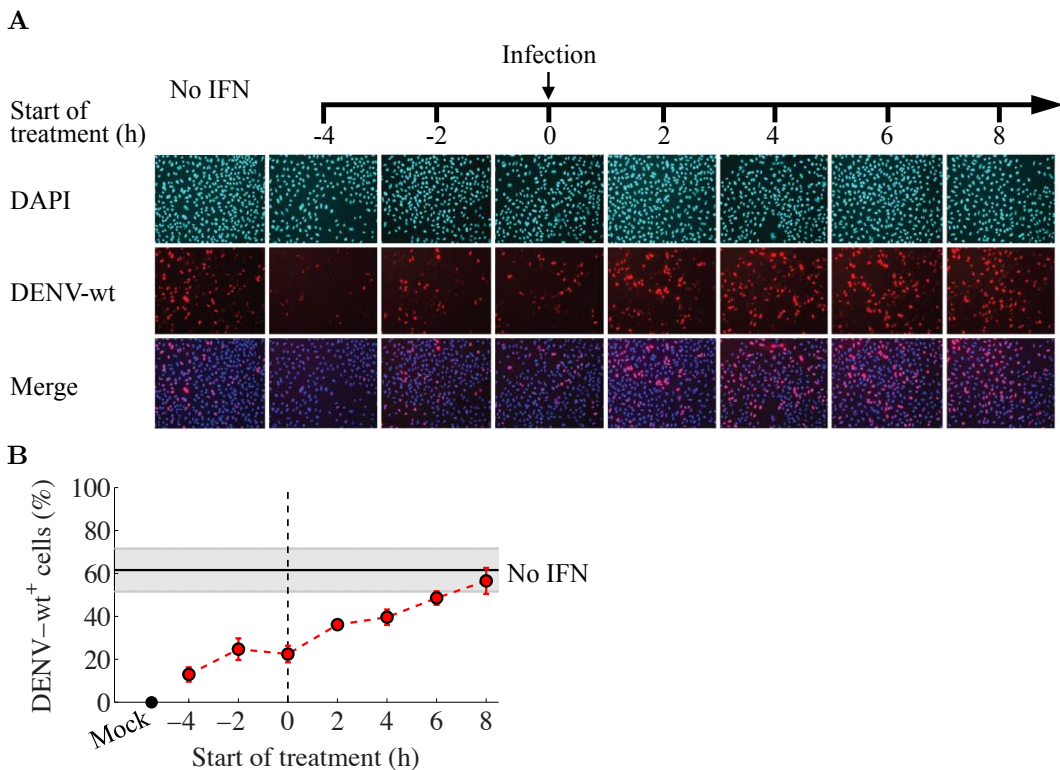


**Figure 3.5.: IFN can protect naïve cells against DENV infection and, if given early, reduces viral replication in infected cells.** (A, B) IFN-competent A549 cells were left untreated (no IFN, first column) or treated with 100 international units per milliliter (IU/ml) IFN- $\alpha$  prior (-4 h, -2 h), at (0 h) or post (2 h, 4 h, 6 h, 8 h) infection with DENV-wt at a MOI of 10. (A) After an infection period of 24 h we performed immunofluorescence assay to highlight nuclear DNA by 4',6-diamidino-2-phenylindole (DAPI) fluorescence staining (upper row, cyan color) and simultaneously visualized DENV-wt using a NS5-specific antiserum (middle row, red color). Merged images of DAPI and DENV-wt staining are shown in the last row. Mock-treated cells served as control (cf. (B)). (B) Quantification of DENV-wt positive cells in (A) by analyzing 500-1000 cells in two view fields for each column in (A). The error bar diagram illustrates the mean values and standard deviations for treated cells, while the mean value and standard deviation for the measurement without treatment is specified by the black and gray horizontal lines, respectively. The dashed vertical line indicates the experiment in which cells were stimulated and infected at the same time. (Experiments by Bianca Schmid and Ralf Bartenschlager)

viral replication and virus production, we found an increase of ISG56 mRNA (coding for IFIT1) starting 12 h p.i. followed by a delayed release of IFN- $\lambda$  from 18 h p.i. onwards. This temporally resolved data set provides a good overview of viral and virus-induced kinetics after DENV infection.

Furthermore, the data in Figure 3.7 demonstrate that DENV replication induces IFN production in A459 cells. To investigate the antiviral effect of secreted IFN to activate ISG expression in our system, we treated the established IFIT1-deGFP and MxA-deGFP reporter cells (cf. Figure 3.2) with IFN- $\alpha$  and measured for several ISGs the mRNA expression levels in deGFP positive as well as negative cells (Figure 3.8A for IFIT1-deGFP reporter cells, similar results for MxA-deGFP reporter cells (cf.

### 3.1. Dissecting the dynamics of IFN-induced antiviral defense against DENV

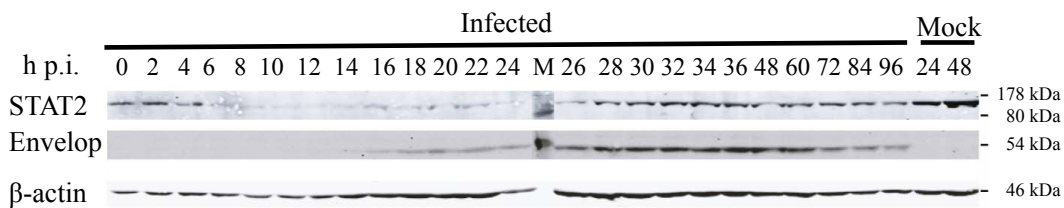


**Figure 3.6.:** DENV counteracts the IFN response by STAT2 degradation. IFN-competent A549 cells were infected with DENV-wt at a MOI of 10. At the given time points post infection (p.i.), STAT2 (upper strip), DENV envelop (middle strip) and  $\beta$ -actin (last strip, as loading control) protein levels were detected simultaneously by Western blot analyze under the usage of the respective specific antibodies. Mock-infected cells (last two columns) serves as reference. A representative immunoblot out of three independent experiments is shown. (Experiments by Bianca Schmid and Ralf Bartenschlager)

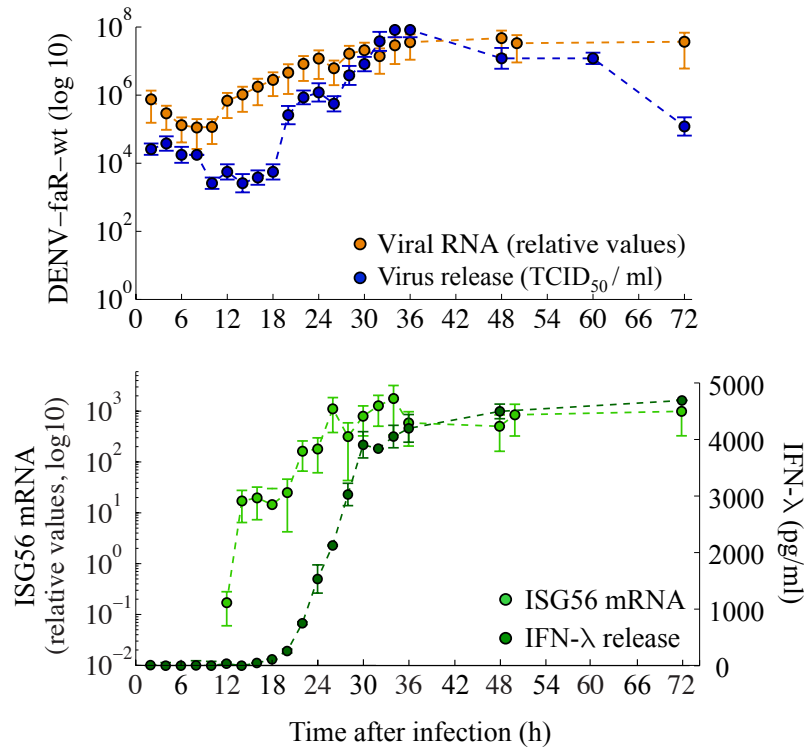


**Figure 3.7.:** Temporally resolved dynamics of viral replication, virus production and immune activation after DENV infection. IFN-competent A549 cells were infected with DENV-faR-wt at a MOI of 10 and analyzed at the indicated time points post infection (p.i.). Upper panel: Viral RNA (orange color) was evaluated by quantitative real time reverse polymerase chain reaction (qRT-PCR). In addition, we measured extracellular virus (blue color) by performing a limiting dilution assay to determine the tissue culture infectious dose 50 (TCID<sub>50</sub>) per milliliter (ml). Lower panel: ISG56 mRNA (light green color) was quantified using qRT-PCR. Moreover, we detected the amount of extracellular IFN- $\lambda$  (dark green color) by enzyme-linked immunosorbent assay (ELISA). The virus release data is a representative result out of three independent experiments. All other values correspond to the mean and standard deviation of independent triplicate measurements. (Experiments by Bianca Schmid and Ralf Bartenschlager)

3. Viral fitness is mainly controlled by the effect of IFN on already infected cells

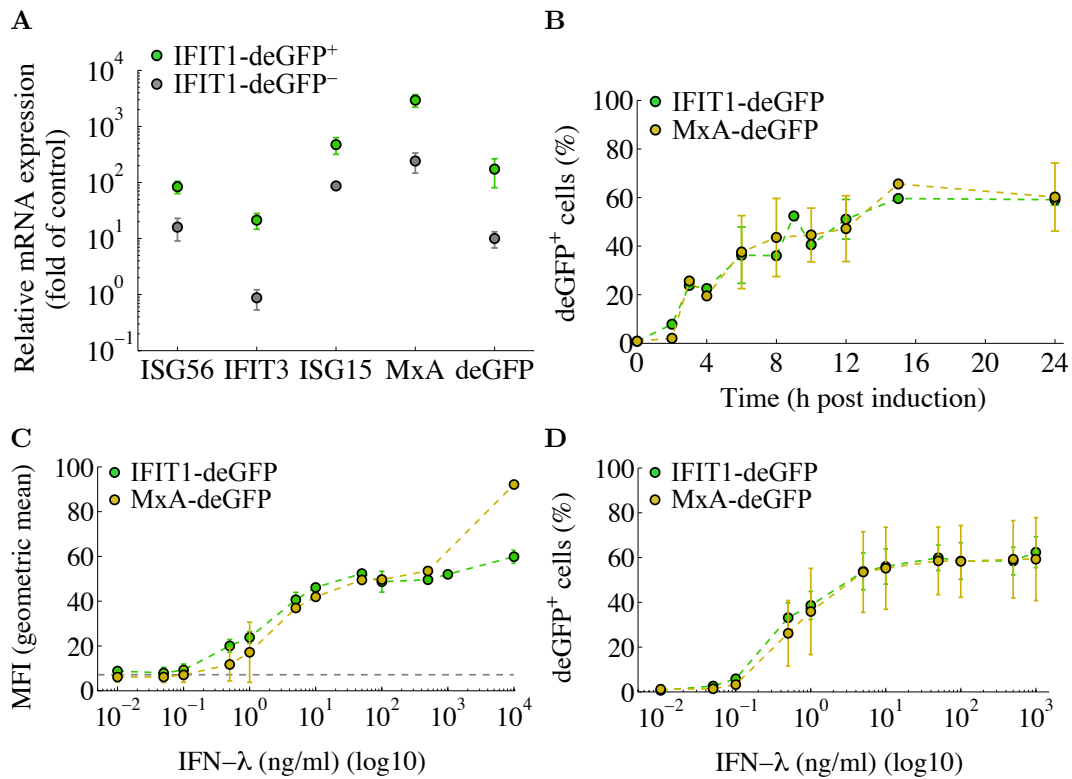


**Figure 3.8.**: Comparable time and dose-dependent IFN response of IFIT1 and MxA reporter cells. (A) Expression of different ISGs in IFIT1 positive cells. A549 IFIT1-deGFP reporter cells were stimulated with 10 IU/ml IFN- $\alpha$  for 24 h and subsequently sorted according to deGFP expression by flow cytometry. Immediately after sorting IFIT1-deGFP<sup>+</sup> (green error bars) and IFIT1-deGFP<sup>-</sup> (gray error bars) were lysed and total RNA was extracted. Amounts of different ISG mRNAs (x-axis) were quantified using qRT-PCR and normalized to GAPDH mRNA levels (y-axis). (B) Similar induction kinetics of IFIT1 and MxA reporter cells after IFN stimulation. A549 IFIT1-deGFP and MxA-deGFP reporter cells were stimulated with 10 ng/ml IFN- $\lambda$ . At the indicated time points we detected the fraction of IFIT1-deGFP<sup>+</sup> cells (green color) and MxA-deGFP<sup>+</sup> cells (yellow color) by flow cytometry. (C, D) Dose-dependent IFN response of IFIT1 and MxA reporter cells. A549 IFIT1-deGFP and MxA-deGFP reporter cells were stimulated with various concentrations of IFN- $\lambda$  (x-axis) for 24 h. The mean fluorescence intensity (MFI) (C; dashed gray line indicates the detection limit) and the fraction of deGFP positive cells (D) was determined for IFIT1-deGFP reporter cells (green color) and MxA-deGFP reporter cells (yellow color) by flow cytometry. The dose-response data regarding IFIT1 represents the mean and standard deviation of three independent experiments. All other values correspond to the mean and standard deviation of two independent measurements. (Experiments by Bianca Schmid and Ralf Bartenschlager)

Schmid (2014)). IFN-treated and deGFP positive cells expressed a higher amount of ISG mRNAs than IFN-stimulated deGFP negative cells. We also monitored the induction kinetics of our IFIT1-deGFP and MxA-deGFP reporter cells after stimulation with biologically equipotent concentrations (Bauhofer et al. (2012)) of IFN- $\alpha$  or IFN- $\lambda$  (Figure 3.8B for IFN- $\lambda$  treatment, similar results after IFN- $\alpha$  stimulation (cf. Schmid (2014))). The fraction of IFIT1-deGFP<sup>+</sup> and MxA-deGFP<sup>+</sup> was almost identical over time for both types of IFN. In addition, we studied the dose response

### *3.1. Dissecting the dynamics of IFN-induced antiviral defense against DENV*

of IFIT1-deGFP and MxA-deGFP reporter cells towards IFN- $\alpha$  and IFN- $\lambda$  (Figure 3.8C and D for IFN- $\lambda$ , similar results for IFN- $\alpha$  (cf. Schmid (2014)). The mean fluorescence intensity (MFI) (Figure 3.8C) as well as the number of IFN-responding cells (Figure 3.8D) increased with higher IFN concentrations. With the exception of the MFI values after stimulation with high IFN concentrations, we detected a substantial agreement of the dose-dependent IFN response between IFIT1 and MxA reporter cells. These data show that the IFIT1 and MxA reporter cells are comparable to each other and respond in a time and dose-dependent way to IFN- $\alpha$  as well as IFN- $\lambda$  with the expression of different ISGs.

In summary, our data revealed both the ability of DENV to spread efficiently in IFN-competent cells as well as the paracrine effect of secreted IFN to protect naïve cells from productive DENV infection and, if given early, to inhibit viral replication in infected cells in an autocrine manner.

#### **3.1.3. Cell-to-cell heterogeneity of DENV replication and IFN response reveal coexistence of viral spread and antiviral protection**

As we are particularly interested to analyze the immediate interactions between DENV infection and the antiviral IFN system, we utilized the generated DENV reporter construct together with our fluorescence reporter cells for live-cell dual-color imaging (cf. section 3.1.1).

Firstly, we studied the induction of IFN after DENV infection through analyzing the virus-induced nuclear translocation of the transcription factor IRF-3. After high-dose infection of the constructed IRF-3-eGFP reporter cells with DENV-faR-wt, we monitored viral replication along with IRF-3-eGFP expression by time-lapse microscopy (Figure 3.9A, viral replication colored in red and IRF-3-eGFP expression in cyan color). Initially, we observed the expression of the latent transcription factor IRF-3 in the cytoplasm of the cells. After a certain delay post infection, the number of virus replicating cells increased over time and nuclear translocation of IRF-3 was detectable in some infected cells. To quantify the onset of fluorescence expression and the first nuclear translocation of IRF-3-eGFP, our intern Jonas Förster manually tracked single cells by using the MTrackJ plug-in of the ImageJ software package. The tracking data of individual cells showed a broad distribution of DENV-faR-wt expression onset as well as highly varying initial nuclear translocation of IRF-3 (Figure 3.9B and C). The onset of viral replication started ~ 12 h p.i., whereas IRF-3 initially translocated into the nucleus ~ 18 h p.i.. During the approximately 55 h lasting time period of DENV-faR-wt expression onset as well as IRF-3 activation, we tracked IFN induction in 34% of the virus replicating cells. These live-cell imaging data demonstrate a high heterogeneity of viral replication and IFN induction after DENV infection at single-cell level.

In addition to the virus-induced transcription factor activation, we examined the dynamics of DENV replication and spread together with the IFN response in real time. For this purpose we performed live-cell microscopy experiments of IFIT1-

### 3. Viral fitness is mainly controlled by the effect of IFN on already infected cells

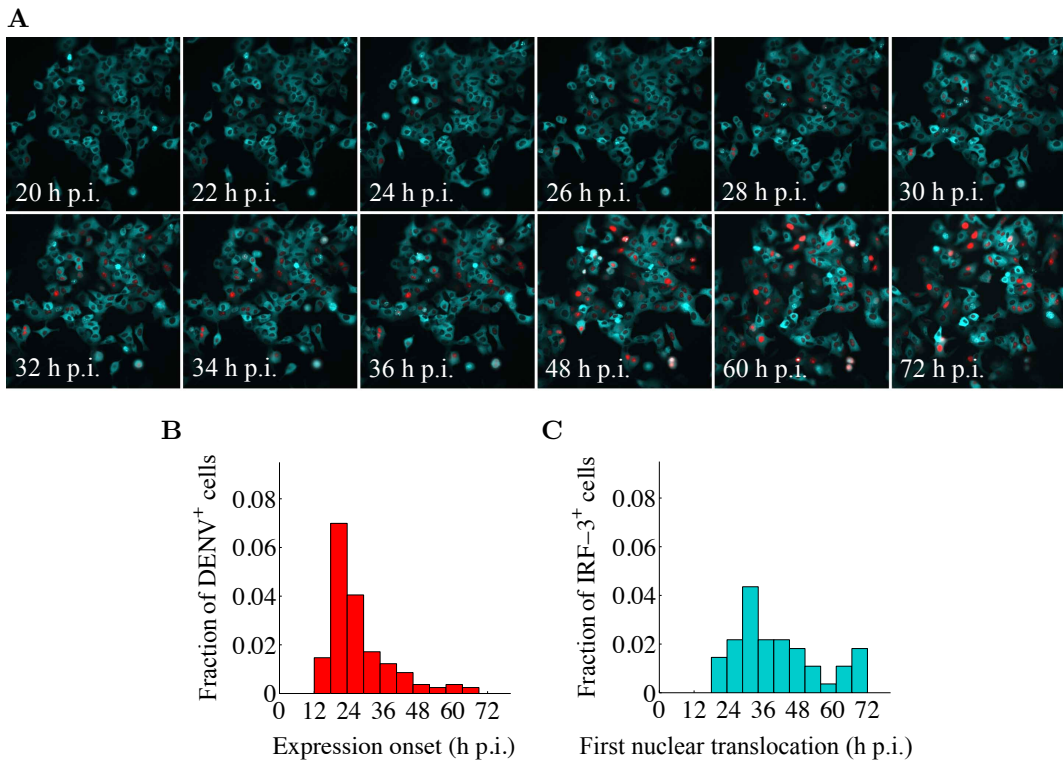


**Figure 3.9.: Single-cell heterogeneity of DENV replication and IFN induction.** (A-C) A549 IRF-3-eGFP reporter cells were infected with DENV-faR-wt at a MOI of 150 and monitored every hour via time-lapse microscopy. Quantification of expression onset of DENV-faR-wt and first nuclear translocation of IRF-3-eGFP was evaluated by manually tracking of single-cell dynamics under the usage of the MTrackJ plug-in of the ImageJ software package. Shown are tracking data without daughter cell informations. (A) Representative fluorescence pictures at indicated time post infection (p.i.) visualize the expression of latent transcription factor IRF-3 (cyan cytoplasm), DENV-faR-wt replication (red nucleus) and translocated IRF-3 (cyan nucleus). (B) Quantification of the expression onset of 143 DENV-faR-wt<sup>+</sup> cells in the time period between [12 h.p.i.; 69 h.p.i.]. (C) Detection of the first nuclear translocation of 51 IRF-3-eGFP<sup>+</sup> cells in the time frame between [18 h.p.i.; 72 h.p.i.]. (Experiments by Bianca Schmid and Ralf Bartenschlager; manual tracking by Jonas Förster)

deGFP reporter cells (Figure 3.10A) or MxA-deGFP reporter cells (Figure 3.11A) post infection with DENV-faR-wt at a low MOI to enable viral spread through secondary infection events. The time delay until the initial DENV-faR-wt expression appeared was quite similar in both cell lines with 22 h.p.i. for IFIT1-deGFP and 24 h.p.i. for MxA-deGFP reporter cell, respectively (cf. Figure 3.10B and Figure 3.11B). The expression onset of DENV-faR-wt was in both ISG reporter cells broadly distributed. Given that infected cells produce new virus particles from approximately 14 h.p.i. onwards (cf. blue curve in Figure 3.7) and that replication is detectable ~ 22 – 24 h after infection by the faR reporter, the large number of cells becoming DENV-faR-wt positive between 1.5 and 3 days is probably caused by viral spread and secondary infection events.

During the propagation process of DENV, many cells achieve protection against viral infection by induction of antiviral ISGs. The first onset of ISG-reporter expression

### 3.1. Dissecting the dynamics of IFN-induced antiviral defense against DENV

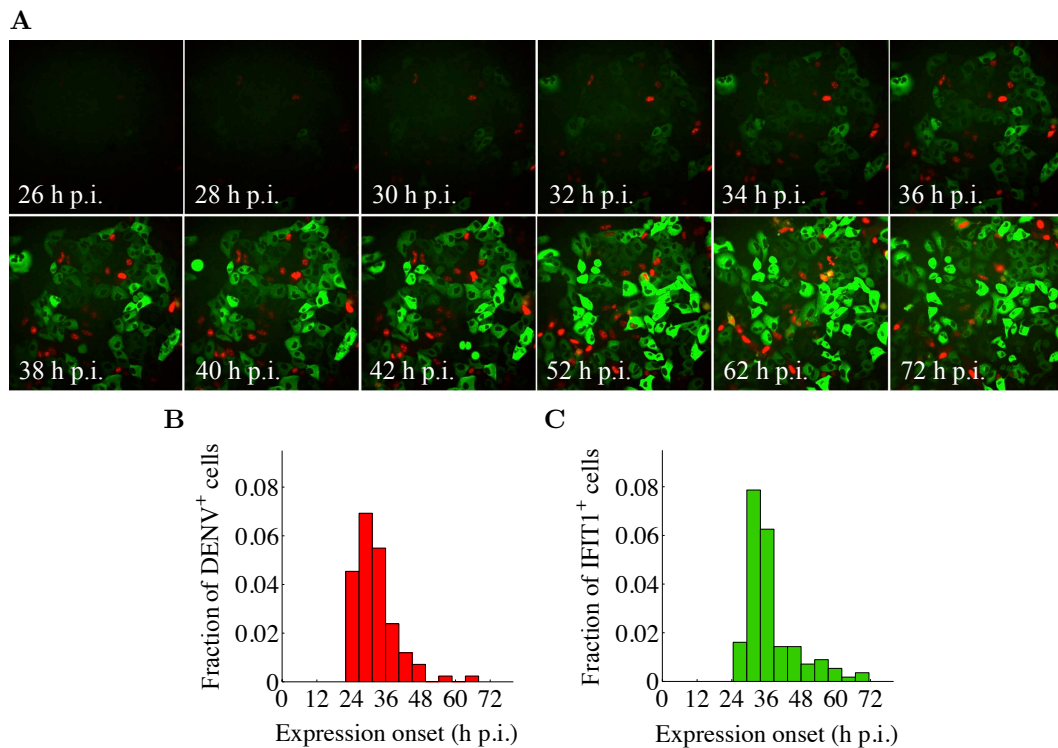


**Figure 3.10.:** Coexistence of viral spread and antiviral IFIT1 expression. (A-C) A549 IFIT1-deGFP reporter cells were infected with DENV-faR-wt at a MOI of 0.2 and monitored every half hour via time-lapse microscopy. Quantification of expression onset was evaluated by manually tracking of single-cell dynamics under the usage of the MTrackJ plug-in of the ImageJ software package. Shown are tracking data without daughter cell informations. (A) Representative fluorescence pictures at indicated time post infection (p.i.) visualize the expression of DENV-faR-wt (red nucleus) and IFIT1-deGFP (green cytoplasm). (B) Quantification of the expression onset of 91 DENV-faR-wt<sup>+</sup> cells in the time period between [22.0 h p.i.; 68.0 h p.i.]. (C) Detection of 119 IFIT1-deGFP<sup>+</sup> cells in the time frame between [24.5 h p.i.; 71.5 h p.i.]. (Experiments by Bianca Schmid and Ralf Bartenschlager; manual tracking by Jonas Förster)

was delayed relative to the appearance of DENV-faR-wt positive cells by 2.5 h for IFIT1-deGFP and 7 h in the case of MxA-deGFP. The short time period between the initial DENV-faR-wt and IFIT1-deGFP expression possibly reflects the required time to activate IFIT1 directly by IRF-3 in an IFN-independent manner as recorded in the literature (Grandvaux et al. (2002), Diamond and Farzan (2013)). However, only rarely we observed IFIT1-deGFP - DENV-faR-wt double-positive cells, arguing that in our system IFIT1 expression is induced primarily by IFN. In contrast to IFIT1, the induction of MxA requires the activation of JAK-STAT signaling pathway by extracellular IFN (Bandyopadhyay et al. (1995)). Indeed, the number of MxA-deGFP - DENV-faR-wt double-positive cells was negligible. In particular, the fact that DENV-faR expressing cells did not induce MxA-deGFP is consistent with an efficient block of JAK-STAT signaling in DENV-infected cells (cf. Figure 3.6). Although DENV is able to prevent antiviral protection in infected cells and efficiently spreads, the highly heterogeneous onset of IFIT1-deGFP and MxA-deGFP expression (cf. Figure 3.10C and Figure 3.11C) demonstrate that antiviral protection

### 3. Viral fitness is mainly controlled by the effect of IFN on already infected cells

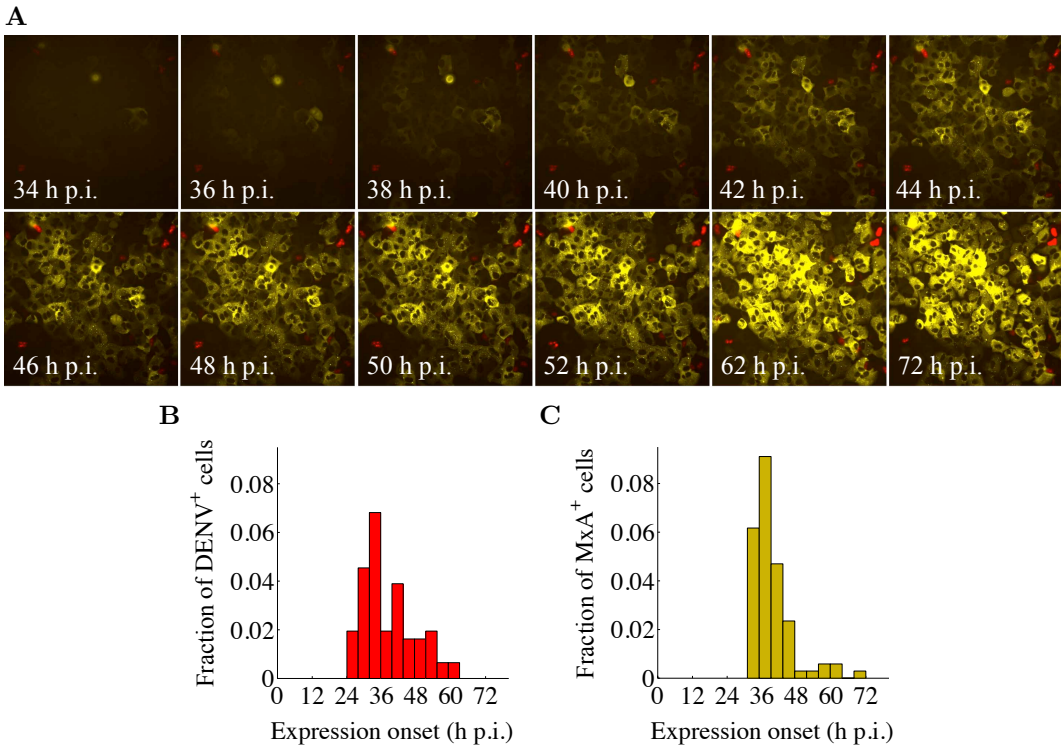


**Figure 3.11.: Coexistence of viral spread and antiviral MxA expression.** (A-C) A549 MxA-deGFP reporter cells were infected with DENV-faR-wt at a MOI of 0.1 and monitored every hour via time-lapse microscopy. Quantification of expression onset was evaluated by manually tracking of single-cell dynamics under the usage of the MTrackJ plug-in of the ImageJ software package. Shown are tracking data without daughter cell informations. (A) Representative fluorescence pictures at indicated time post infection (p.i.) visualize the expression of DENV-faR-wt (red nucleus) and MxA-deGFP (yellow cytoplasm). (B) Quantification of the expression onset of 79 DENV-faR-wt<sup>+</sup> cells in the time period between [24 h p.i.; 63 h p.i.]. (C) Detection of 83 MxA-deGFP<sup>+</sup> cells in the time frame between [31 h p.i.; 72 h p.i.]. (Experiments by Bianca Schmid and Ralf Bartenschlager; manual tracking by Jonas Förster)

of naïve cells by IFN coexists with viral spread in unprotected cells.

Additionally, we checked whether the heterogeneous IFN response in single cells is not caused by an insufficiency of cells to respond towards secreted IFN. Firstly, we measured the fraction of IFIT1-deGFP positive cells upon stimulation with different concentrations of IFN- $\alpha$  using flow cytometry (Figure 3.12A). The determined IFN-responding fraction increased continuously with IFN- $\alpha$  dose to nearly 100%. Afterwards, we sorted IFIT1-deGFP reporter cells treated with either 10 or 100 IU/ml IFN- $\alpha$  into deGFP-expressing and non-expressing fractions. Sorted cell fractions were seeded and re-stimulated with the same IFN- $\alpha$  concentrations as in the first treatment (Figure 3.12B). Almost all cells that had responded in the first stimulation experiment expressed IFIT1-deGFP after the second treatment. This high degree of responsiveness is possibly a result of larger amounts of signal-transduction molecules like STAT1/2 as well as IRF-9 and/or the further induction of these proteins during the first IFN treatment (Maiwald et al. (2010)). However, cells that

### 3.1. Examination of viral fitness by comparing DENV-wt with a DENV mutant

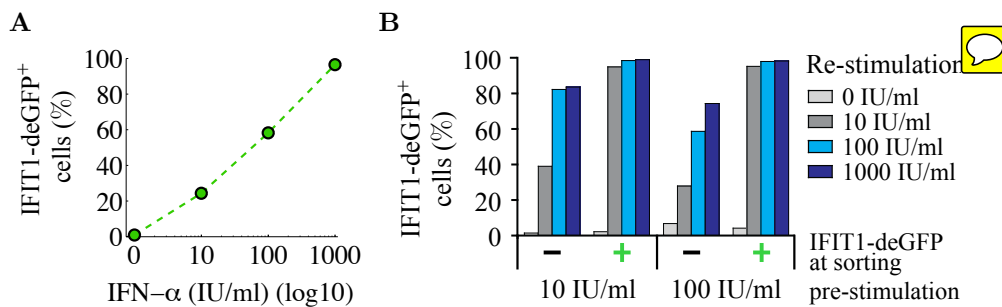


**Figure 3.12.:** Cell-to-cell heterogeneity of the IFN response. (A) A549 IFIT1-deGFP reporter cells were treated with increasing amounts of IFN- $\alpha$  (x-axis) for 24 h. After the stimulation period we determined the fraction of IFIT1-deGFP<sup>+</sup> cells (y-axis) by flow cytometry. (B) A549 IFIT1-deGFP reporter cells stimulated with 10 or 100 IU/ml IFN- $\alpha$  for 24 h from (A) were sorted in IFIT1-deGFP<sup>-</sup> and IFIT1-deGFP<sup>+</sup> cells (x-axis). Separated cell groups were seeded and 24 h later re-stimulated with IFN- $\alpha$  concentrations specified in the legend. After a re-stimulation period of 24 h we measured the fraction of IFIT1-deGFP<sup>+</sup> cells (y-axis) by flow cytometry. (Experiments by Bianca Schmid and Ralf Bartenschlager)

did not respond to primary IFN- $\alpha$  treatment showed practically the same dose response as naïve cells during primary IFN- $\alpha$  application. These results indicate that responsiveness to extracellular IFN is a stochastic process in individual cells.

Overall, the single-cell analysis demonstrates similar time courses of IFIT1-deGFP and MxA-deGFP induction, further supporting that secreted IFN are the prime inducer of the antiviral response. Cells expressing either ISG reporter remained DENV-faR-wt negative, showing that IFN produced from DENV-infected cells protected naïve cells against virus infection. Thus, the live-cell imaging data indicates that viral spread and protection of cells through the IFN response occur in parallel - and compete - after DENV infection.

#### 3.1.4. Examination of viral fitness by comparing DENV-wt with a DENV mutant lacking 2'-O-methyltransferase activity

Our studies of the interactions between DENV and the IFN system revealed that efficient viral spread and IFN-induced antiviral immune defense occur simultaneously in an infected cell population (cf. section 3.1.2 and 3.1.3). To analyze which antiviral factors have the greatest influence on viral fit*n*, we compared DENV-wt with the DENV-E217A mutant, which is unable to modify the DENV RNA genome by 2'-O-methylation (Egloff et al. (2002), Ray et al. (2006), Dong et al. (2014)). According to findings from the literature, the 2'-O-methylation of the viral genome serves as a mechanism to evade detection of the virus by intracellular pattern recognition receptors (Züst et al. (2011)). Additional published results show that the 2'-O-methyltransferase activity of viruses largely overcomes IFIT1-mediated antiviral response (Daffis et al. (2010), Züst et al. (2011), Szretter et al. (2012), Kimura et al. (2013)). However, virus mutants, which lack 2'-O methylation of the viral genome, induce stronger immune responses, are severely attenuated in vivo, and thus might serve as vaccine candidates (Li et al. (2013), Züst et al. (2013), Fink and

### 3. Viral fitness is mainly controlled by the effect of IFN on already infected cells

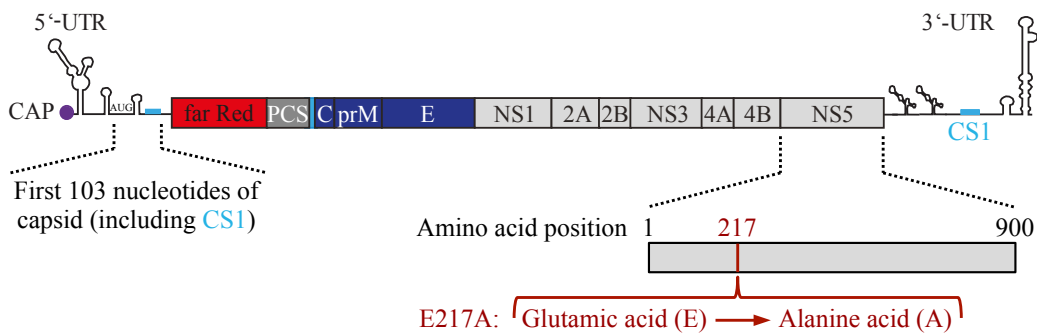


**Figure 3.13.:** Scheme of the established DENV-faR-E217A mutant reporter virus. Based on the DENV-faR-wt reporter construct (cf. Figure 3.2A) we generated the DENV-faR-E217A mutant through substituting the glutamic acid residue (E) by an alanine residue (A) at the amino acid position 217 of the NS5 protein (dark red color). To avoid reversion back to the original amino acid residue, two nucleotides were additionally exchanged. (Graph provided by Bianca Schmid (Schmid (2014)))

Shi (2014)). A molecular rationale for the attenuated DENV-E217A mutant infection comes from the observation that IFIT1 sequesters 2'-O-unmethylated capped RNA and hence inhibits the translation of viral RNA (Pichlmair et al. (2011), Habjan et al. (2013)). Given that IFIT1 can be expressed already in an IFN-independent manner (Grandvaux et al. (2002), Diamond and Farzan (2013)), it remains controversial whether the attenuation of the DENV-E217A mutant depends on IFN action (Züst et al. (2011)) or not (Daffis et al. (2010)). In the following we address this question for DENV on a quantitative basis.

To examine the dynamics of the DENV-E217A mutant in living cells, we generated a replication competent DENV-faR-E217A fluorescence reporter (Schmid (2014)). The DENV-faR-E217A mutant was created from the DENV-faR-wt reporter construct through substituting the glutamic acid residue (E) by an alanine residue (A) at the amino acid position 217 of the NS5 protein (cf. Figure 3.13) (Egloff et al. (2002), Züst et al. (2013)). To prevent reversion back to the original amino acid residue, we also exchanged two nucleotides.

The infection of our IFN-competent IFIT1-deGFP and MxA-deGFP reporter cells with DENV-faR-wt or DENV-faR-E217A is a suitable reporter system to investigate the differences between wild-type and 2'-O-unmethylated DENV infections. To directly compare the dynamics of DENV-wt with DENV-E217A mutant, we performed in parallel time-resolved flow cytometry measurements of our ISG reporter cells after infection with DENV-faR-wt or DENV-faR-E217A (Figure 3.14A and B for IFIT1-deGFP reporter cells, similar results for MxA-deGFP reporter cells (cf. Schmid (2014))). Both ISG reporter cell lines were infected with a low viral titer to allow viral spread through secondary infection events. The dynamic flow-cytometric analysis for all experimental combinations was independently repeated and yielded comparable results (cf. data in Figure 3.21 for IFIT1-deGFP reporter cells). After infection with DENV-faR-wt we detected the first virus replicating cells 36 h p.i. followed by a continuous rise of DENV-faR-wt positive cells over time. Approximately 12 h after the onset of DENV-faR-wt expression cells began to express IFIT1-deGFP and the fraction of responding cells increased in the

### 3.1. Examination of viral fitness by comparing DENV-wt with a DENV mutant

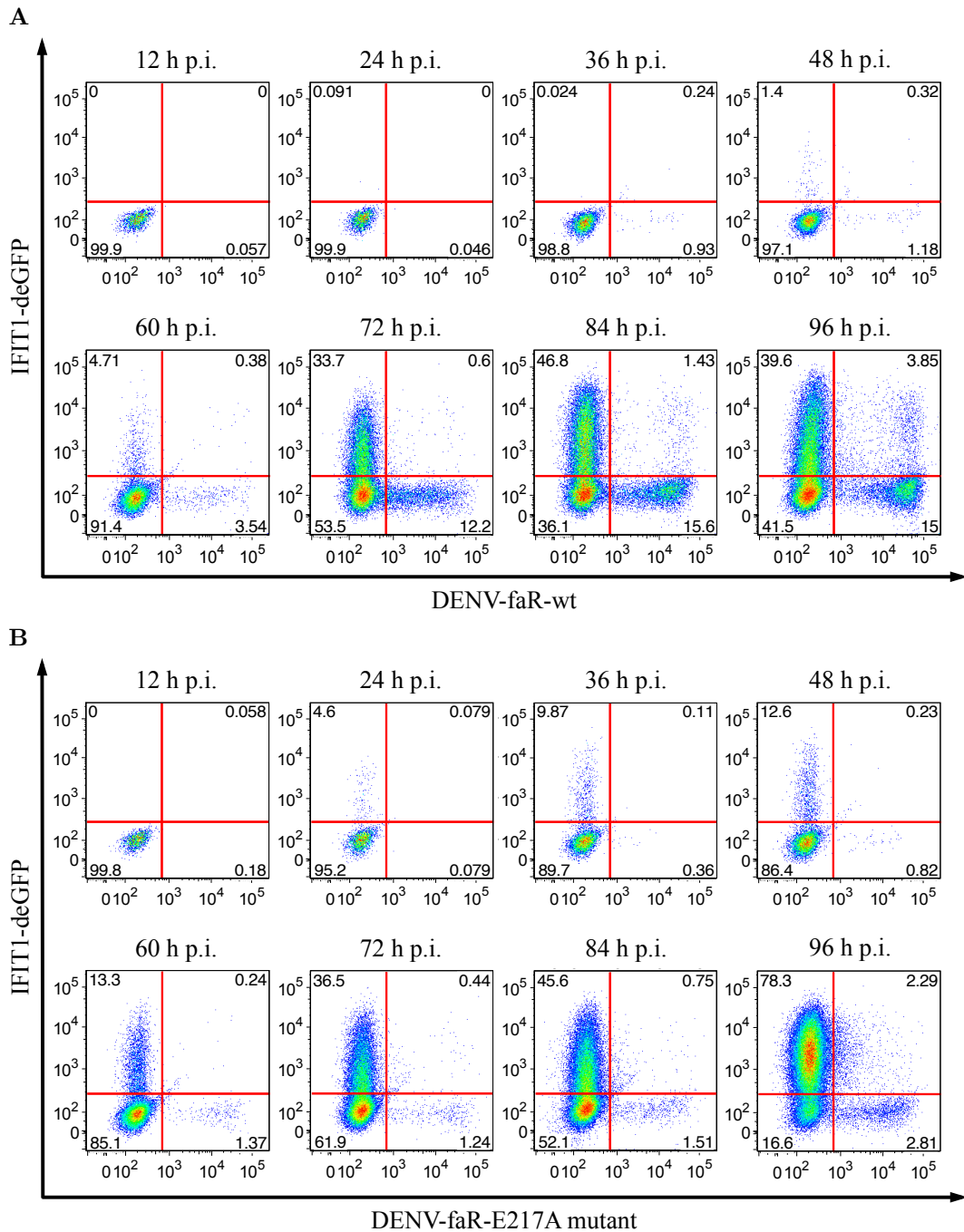


**Figure 3.14.: In contrast to DENV-wt, the DENV-E217A mutant causes faster IFN response and barely spreads. (A, B)** A549 IFIT1-deGFP reporter cells were infected with DENV-faR-wt (A) or DENV-faR-E217A mutant (B) at a MOI of 0.1. At the indicated time points post infection (p.i.), cells were fixed and 100  $\mu$ l of the cell suspension was subjected to flow cytometry. The dot plots illustrate the jointly measured DENV-faR (x-axis) and IFIT1-deGFP (y-axis) fluorescence intensities of individual cells. Shown is one of two independent experiments after infection with DENV-wt or DENV-E217A mutant. (Experiments by Bianca Schmid and Ralf Bartenschlager)

### 3. Viral fitness is mainly controlled by the effect of IFN on already infected cells

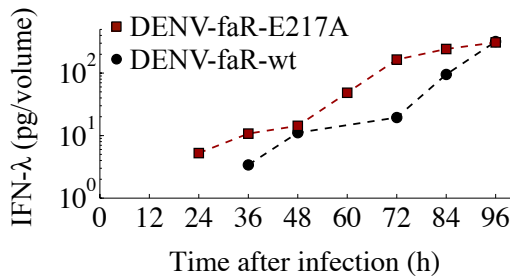


**Figure 3.15.:** In comparison to DENV-wt, the DENV-E217A mutant induces faster and enhanced IFN production. Cell supernatant of A549 IFIT1-deGFP reporter cells infected with DENV-faR-wt (black color) or DENV-faR-E217A mutant (dark red color) at a MOI of 0.1 from the experiment shown in Figure 3.14 were harvested in 12 hour intervals. The supernatants were analyzed for IFN- $\lambda$  expression by ELISA. With respect to the measured volume in the associated flow cytometry experiments (cf. Figure 3.14) IFN- $\lambda$  expression is given in pg per 100  $\mu$ l. (Experiments by Bianca Schmid and Ralf Bartenschlager)

time frame between [48 h p.i.; 84 h p.i.]. In contrast to DENV-faR-wt infection, the DENV-faR-E217A infected cells became IFIT1-deGFP positive much earlier at  $\sim$  24 h p.i. and the fraction of IFIT1-deGFP expressing cells rose strongly until the end of the experiment. The initial DENV-faR-E217A positive cells were visible 36 h p.i. and only a minor increase of DENV-faR-E217A replicating cells could be monitored within the observation period. In agreement with the single-cell analysis by time-lapse microscopy (cf. section 3.1.3 page 49), the fraction of IFIT1-deGFP - DENV-faR double-positive cells was very low. Altogether, the immediate comparison of DENV-wt with DENV-E217A demonstrates that the DENV-E217A mutant induces, on the one hand, an attenuated infection and, on the other hand, an earlier as well as enhanced IFN response.

In addition, we used the cell culture supernatants of the kinetic experiments to quantify the production of IFN. We found that the A549 reporter cells predominantly express IFN- $\lambda$  (Figure 3.15), while the secretion of IFN- $\beta$  was comparatively lower and IFN- $\alpha$  was not detectable (Schmid (2014)). After infection with DENV-faR-wt extracellular IFN- $\lambda$  was verifiable from 36 h p.i. onwards and increased over time. In the DENV-faR-E217A infected cell culture we detected IFN- $\lambda$  12 hours earlier and to a larger extent than after DENV-faR-wt infection, although the fraction of virus replicating cells was much lower after DENV-faR-E217A mutant infection. The IFN- $\lambda$  production and IFIT1-deGFP expression appeared simultaneously 24 h post DENV-faR-E217A infection (cf. Figure 3.14B), while in the DENV-faR-wt experiment the onset of IFIT1-deGFP expression occurred 12 hours after the initial release of IFN- $\lambda$  (cf. Figure 3.14A). As very low levels of produced IFN lie probably below the detection limit of the ELISA, we have no experimental informations about the exact onset time of IFN production. But comparing the shape of the IFN- $\lambda$  release kinetics after DENV-faR-wt or DENV-faR-E217A infection, we assume an earlier secretion of IFN- $\lambda$  through DENV-faR-E217A infected cells.

In summary, compared to DENV-wt, the vaccine candidate DENV-E217A mutant elicits faster IFN production which in turn results in an earlier onset of the IFN response and barely spreads in IFN-competent cells.

### 3.2. Population-based delay-differential equation model of viral spread and IFN-induced antiviral defense

Our research of the competition between spreading DENV and IFN-induced antiviral protection is driven by the question, which components of the IFN system have the greatest influence on viral fitness. The comparison between DENV-wt and attenuated DENV-E217A mutant infections (cf. section 3.1.4), is a perfectly suited experimental tool to detect key factors contributing strongly to the improved limitation of DENV-E217A mutant. To analyze the underling mechanisms of the differences between DENV-wt and DENV-E217A mutant infections by means of mathematical modeling, we need to select the appropriate type of model to describe our data beforehand.

On the one hand, the results of our stochastic model of the IFN response against primary viral infection demonstrate that the heterogeneous single-cell behavior can be translated into predictable cell population dynamics (cf. section 2.2.3 and 2.4). On the other hand, a rapid spread of DENV and IFN over many cell diameters on the relevant time scale of hours is proven by the high diffusion coefficients of DENV and IFN ( $D_{\text{DENV}} = 1.0 \times 10^4 \mu\text{m}^2/\text{h}$  (Chang et al. (2008)) and  $D_{\text{IFN}} = 1.1 \times 10^5 \mu\text{m}^2/\text{h}$  (Hu et al. (2011)), respectively), and spatial gradients are therefore negligible. For these reasons, we decide to use a population-based modeling approach with uniform distribution of secreted IFN and viral spread. The time-resolved data after DENV-wt or DENV-E217A mutant infection (cf. Figure 3.14 and 3.15) suggest that the timing of viral spread as well as IFN release plays an important role in the competition between virus and the IFN system. Accordingly, we established a population-based delay-differential equation (DDE) model of viral spread and IFN-induced antiviral defense.

DDEs form a category of equations, which can in a certain sense be classified between ordinary differential equations (ODEs) and time-dependent partial differential equations (PDEs) (Baker et al. (1999), Bocharov and Rihan (2000)). PDEs provide the basis for age-structured or, more widely, state-structured population models (Charlesworth (1980), Metz and Diekmann (1986), Barbarossa (2013)) where the population is characterized by a distribution depending on both time and a property of the individuals like age, mass or any other feature (cf. Bocharov and Hadeler (2000), Getto et al. (2008), Gwiazda et al. (2014), for instance). While state-structured population models deal with at least two independent dynamic variables, DDE models only consider temporal dynamics (cf. Lee et al. (2009), Pawelek et al. (2012), for example).

In general, DDEs are defined by equations of the form

$$\dot{y} = f(t, y(t), \mathcal{W}(\omega_1(t), y(t)), \mathcal{W}(\omega_2(t), y(t)), \dots, \mathcal{W}(\omega_n(t), y(t))), \quad (3.1)$$

with  $t \in \mathbb{R}$ ,  $n \in \mathbb{N}$ , weighting functions  $\omega_i(t)$  for  $i = 1, \dots, n$  and

$$\mathcal{W}(\omega_i(t), y(t)) = \int_{-\infty}^t \omega_i(t-s) y(s) ds. \quad (3.2)$$

### 3. Viral fitness is mainly controlled by the effect of IFN on already infected cells

A DDE with discrete delays arises, if the weighting factors  $\omega_i(t)$  correspond to delta functions, also called delta distributions,  $\delta(z)$  with  $z = t - \tau_i$  (Murray (2002)).

One possible definition of the delta function  $\delta(z)$  is given by

$$\delta(z) = \begin{cases} 0 & , \text{ for } z \neq 0; \\ \int_{z-\epsilon}^{z+\epsilon} \delta(s)ds = 1 & , \forall \epsilon > 0 \end{cases} \quad (3.3)$$

and results in the following characteristic property:

$$\int_{-\infty}^{\infty} \delta(s-z)f(s)ds = f(z), \quad (3.4)$$

for a continuous function  $f$  on  $\mathbb{R}$ . By applying the property (3.4) as well as setting  $\omega_i(t) = \delta(t - \tau_i)$ , equation (3.2) changes to

$$\mathcal{W}(\delta(t - \tau_i), y(t)) = \int_{-\infty}^t \delta(t - \tau_i - s)y(s)ds = y(t - \tau_i). \quad (3.5)$$

A discrete DDE is defined by the combination of the equation (3.1) and (3.5). If  $\tau_i$  in (3.5) is constant, time-dependent or depending on  $y(t)$ , then the discrete DDE describes a differential equation with constant delay, time-dependent delay or state-dependent delay, respectively (Barbarossa (2013)).

With our population-based model of viral spread and IFN-induced antiviral defense, we would like to analyze the timing of virus replication, virus production and IFN secretion. The measured single-step growth curve of these processes after high dose infection with DENV-faR-wt (cf. Figure 3.7) corresponds, from a mathematical point of view, to the integral of the respective single-cell distribution over time. As an approximation of these temporal distributions, we decided to create a DDE model with constant time delays for virus replication, virus production and IFN secretion. In section 3.3 we will show, that this model can be parameterized by experimental data and therefore could serve as a basis to develop a more complex model in the future.

In our DDE model with constant delays (Figure 3.16 and DDE system (3.11)) we initially consider a number of naïve cells  $S_0$  which are susceptible to virus infection as well as an initial extracellular viral load  $V_0$ . Susceptible cells  $S$  can become infected by extracellular virus  $V$  with the infection rate  $r_V$  (cf. blue arrow in Figure 3.16). Depending on the time, which has elapsed since viruses have entered the host cells, infected cells  $I$  can achieve up to three different features in parallel:

- After a mean latency of virus replication  $\tau_R$ , infected but not yet virus replicating cells  $I_{\bar{R}} \subseteq I$  turn into virus replicating cells  $I_R$ . The time delay  $\tau_R$  is related to the mean expression onset of virus replication in individual cells monitored after infection with DENV-faR-wt (cf. Figure 3.9 - 3.11 and 3.14A) or DENV-faR-E217A mutant (cf. Figure 3.14B).

### 3.2. Population-based model of viral spread and IFN-induced antiviral defense

- After a mean latency of virus production  $\tau_V$ , infected but not yet virus releasing cells  $I_{\bar{V}} \subseteq I$  become virus producing cells  $I_V$  and release new generated infectious virus particles with the virus production rate  $v_V$ . The time delay  $\tau_V$  represents the average time required to replicate, assemble and release new virus particles (cf. blue curve in Figure 3.7).
- After a mean latency of IFN secretion  $\tau_F$ , infected but not yet IFN expressing cells  $I_{\bar{F}} \subseteq I$  turn into IFN secreting cells  $I_F$  and produce IFN  $F$  with the IFN secretion rate  $v_F$ . The time delay  $\tau_F$  corresponds to the mean onset of IFN expression and includes the necessary time of viral sensing, transcription factor activation and subsequent release of IFN (cf. dark green curve in Figure 3.7 and Figure 3.15).

Since the time delay  $\tau_V$  also comprises the duration of virus replication, the condition  $\tau_V > \tau_R$  must be fulfilled, while we do not require any temporal link between  $\tau_F$  and the other both time delays.

According to our experimental study, IFN has two antiviral effects (cf. Figure 3.5):

- Pre-stimulation with IFN demonstrated that secreted IFN can protect naïve cells against productive DENV infection. To incorporate this paracrine IFN response in our model, we take into account an IFN-induced switch from susceptible cells to protected cells  $P$  with the protection rate  $r_F$  (cf. solid green arrow in Figure 3.16).
- Stimulation of infected cells with IFN in an early phase after viral entry can activate antiviral defense mechanisms, which reduce virus replication and consequently virus production. To keep the model simple, so that its parameters can be identified from experimental data, we neglect a direct autocrine impact of IFN in the first instance (cf. dashed green inhibition link in Figure 3.16). After the model parameterization (cf. section 3.3), we will examine the effect of secreted IFN on infected cells explicitly with an extended version of the model (cf. section 3.4 and 3.5).

In order to include the removal of extracellular virus and IFN by cellular uptake and, to a lesser extent, by extracellular degradation, we assume a decrease of virus and IFN with the rate constant of virus degradation  $d_V$  and the rate constant of IFN degradation  $d_F$ , respectively.

Furthermore, we detected that infected cells proliferate less and die faster than not infected cells. To compensate this propagation difference and, additionally, to keep the number of model parameters low, we suppose an inhibited proliferation in infected cells, whereas susceptible and protected cells proliferate with the rates  $p_S$  and  $p_P$ , respectively.

To establish the DDE system of our model, particular attention must be paid to the formulation of the three features of the infected cells comprising virus replication, virus production and IFN expression, which initiate at time  $\tau_R$ ,  $\tau_V$  and  $\tau_F$ , respectively. As the time delays  $\tau_m$  for  $m \in \{R, V, F\}$  are free parameters and only bound to the condition  $\tau_V > \tau_R$ , the properties of the infected cells can initiate at

3. Viral fitness is mainly controlled by the effect of IFN on already infected cells

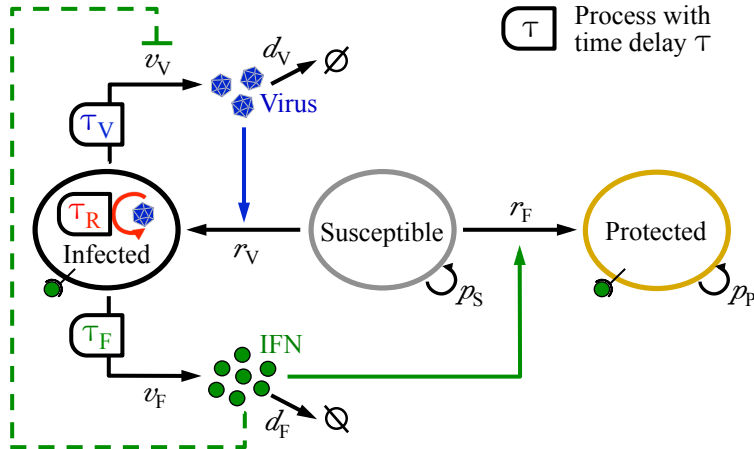


**Figure 3.16.:** Scheme of the mathematical model which describes how naïve and thus susceptible cells become either infected by extracellular virus or protected by the antiviral effect of secreted IFN. Susceptible cells (gray oval) can become infected by extracellular virus with the infection rate  $r_V$  (blue arrow). Virus replication ( $\mathcal{Q}$ ) initiates in infected cells (black oval) at time  $\tau_R$  after viral entry (red color) and results in virus production with the virus production rate  $v_V$  from time  $\tau_V > \tau_R$  onwards. Moreover, infected cells start to express IFN with the secretion rate  $v_F$  at time  $\tau_F$  after viral infestation. Recognition of secreted IFN turn susceptible cells into protected cells (yellow oval) with the protection rate  $r_F$  (solid green arrow). In addition, IFN can indirectly induce antiviral genes in infected cells (dashed green inhibition link). Extracellular virus and IFN are removed ( $\emptyset$ ) by cellular uptake as well as extracellular degradation with the rate constant of virus degradation  $d_V$  and the rate constant of IFN degradation  $d_F$ . While propagation is inhibited in infected cells, susceptible and protected cells proliferate ( $\mathcal{O}$ ) with the rates  $p_S$  and  $p_P$ , respectively.

different times, overlap each other and take place in parallel. Therefore we consider each feature of the infected cells separately and calculate the number of inactive infected cells  $I_{\bar{m}}(t)$  and active infected cells  $I_m(t)$  for  $m \in \{R, V, F\}$  depending on time  $t \in \mathbb{R}$ . For this purpose we firstly require the total number of infected cells  $I$  at time  $t$

$$I(t) = I_{\bar{m}}(t) + I_m(t) \quad (3.6)$$

and the corresponding differential equation

$$\dot{I}(t) \stackrel{\text{page 56}}{\underset{\text{Fig. 3.16}}{=}} r_V V(t) S(t). \quad (3.7)$$

The number of inactive infected cells  $I_{\bar{m}}$  at time  $t$  consists of all cells which become infected in the time period  $[t - \tau_m, t]$  and is given by

$$I_{\bar{m}}(t) \stackrel{(3.7)}{=} \int_{t-\tau_m}^t r_V V(s) S(s) ds. \quad (3.8)$$

To obtain the differential equation  $\dot{I}_{\bar{m}}$ , we differentiate both sides of (3.8) with respect to time  $t$  and apply the fundamental theorem of calculus (Königsberger (2004)):

### 3.2. Population-based model of viral spread and IFN-induced antiviral defense

$$\begin{aligned}\dot{I}_{\bar{m}}(t) &= \frac{d}{dt} \int_{t-\tau_m}^t r_V V(s) S(s) ds \\ &= r_V V(t) S(t) - r_V V(t - \tau_m) S(t - \tau_m).\end{aligned}\quad (3.9)$$

Using the preceding equations, the differential equation  $\dot{I}_m$  results from

$$\begin{aligned}\dot{I}_m(t) &\stackrel{(3.6)}{=} \frac{d}{dt} (I(t) - I_{\bar{m}}(t)) \\ &= \dot{I}(t) - \dot{I}_{\bar{m}}(t) \\ &\stackrel{(3.7)}{=} r_V V(t - \tau_m) S(t - \tau_m).\end{aligned}\quad (3.10)$$

Taking all considerations together, our model is described by the following DDE system:

$$\begin{aligned}\dot{S}(t) &= -r_V V(t) S(t) - r_F F(t) S(t) + p_S S(t) \\ \dot{I}_{\bar{R}}(t) &= r_V V(t) S(t) - r_V V(t - \tau_R) S(t - \tau_R) \\ \dot{I}_R(t) &= r_V V(t - \tau_R) S(t - \tau_R) \\ \dot{I}_{\bar{V}}(t) &= r_V V(t) S(t) - r_V V(t - \tau_V) S(t - \tau_V) \\ \dot{I}_V(t) &= r_V V(t - \tau_V) S(t - \tau_V) \\ \dot{I}_{\bar{F}}(t) &= r_V V(t) S(t) - r_V V(t - \tau_F) S(t - \tau_F) \\ \dot{I}_F(t) &= r_V V(t - \tau_F) S(t - \tau_F) \\ \dot{P}(t) &= r_F F(t) S(t) + p_P P(t) \\ \dot{F}(t) &= v_F I_F(t) - d_F F(t) \\ \dot{V}(t) &= v_V I_V(t) - d_V V(t).\end{aligned}\quad (3.11)$$

The corresponding initial value problem of our model is defined by the DDE system (3.11) for time  $t \geq 0$ . At the starting time  $t_0 = 0$  only two initial values are unequal to zero, namely the number of susceptible cells  $S(0) = S_0$  as well as the extracellular viral load  $V(0) = V_0$ . Additionally, we must provide history functions for those variables in our system (3.11), which have retarded arguments and refer to the past  $[t_0 - \tau_m, t_0]$  for  $m \in \{R, V, F\}$ . Since we will only simulate experiments that start with the initial infection at time  $t_0$ , we use as history functions the constant zero function and consider  $S(t) = 0$  as well as  $V(t) = 0$  for  $t < 0$ .

To solve the DDE system (3.11) we utilize the freely available RADAR5 solver written in ANSI Fortran-90 (Guglielmi and Hairer (2005)). The RADAR5 framework comprises an algorithm to calculate numerically the solution of stiff delay differential equations based on an adapted 3-stage Radau IIA collocation method (Hairer and Wanner (1999), Guglielmi and Hairer (2001), Guglielmi and Hairer (2008)). This algorithm corresponds to a certain implicit Runge-Kutta method of order 5 in which the Runge-Kutta equations are solved by means of a suitable Newton process (Guglielmi (2005)). The Newton iterations require two Jacobian matrices, on the

### 3. Viral fitness is mainly controlled by the effect of IFN on already infected cells

one hand, the standard Jacobian matrix  $\mathcal{J}$  and, on the other hand, the Jacobian matrix with respect to the retarded variables  $\mathcal{J}_\tau$ . These Jacobian matrices are either computed internally or can be provided by the user. In order to increase the accuracy of the numerical solution, we implemented within the RADAR5 framework the time depending Jacobian matrices  $\mathcal{J}(t)$  and  $\mathcal{J}_\tau(t)$  of our DDE system (3.11). An explicit presentation of both Jacobian matrices is given in appendix A.1.

In addition to the RADAR5 solver we also tested Matlab's dde23 solver for delay differential equations with constant delays (Shampine and Thompson (2001), Shampine and Thompson (2009)). Although the implementation in Matlab is more convenient and modifications of the model can be achieved with less effort than within the RADAR5 framework, the significantly faster calculation in Fortran makes the RADAR5 framework more suitable for our system.

## 3.3. Parameterization of the population-based delay-differential equation model

As we are primarily interested to examine the underling mechanisms of the differences between DENV-wt and attenuated DENV-E217A mutant infections (cf. section 3.1.4), we firstly parameterize our model (3.11) by exclusively using measurements concerning DENV-wt infection (cf. section 3.3.1). Based on this DENV-wt specific parameter set, we fit the DENV-E217A mutant related data by allowing only four key parameters to be different (cf. section 3.3.2).

This approach will enable us to discover two parameters which differ strongly between DENV-wt and DENV-mutant infections: The virus production rate is  $\sim 8$ -fold lower and the mean latency of IFN secretion is  $\sim 24$  h shorter after DENV-E217A mutant infection compared to DENV-wt.

### 3.3.1. Estimation of model parameters by using DENV-wt measurements

In order to analyze the mechanistic differences between DENV-wt and attenuated DENV-E217A mutant infections, we intend to firstly parameterize our model (3.11) by considering only experiments regarding DENV-wt infection and, subsequently, utilize these estimates to determine DENV-E217A mutant-specific parameters which differ from the corresponding wild-type values. For parameter estimation we focus on the very well suited data set consisting of time-resolved flow cytometry measurements along with ELISA quantification of IFN- $\lambda$  after infection of the ISG reporter cells with DENV-faR-wt or DENV-faR-E217A (cf. Figure 3.14 and 3.15). This data set was obtained by measuring a specified proportion of the cell suspensions and thus provides quantitative as well as directly comparable differences between DENV-wt and DENV-E217A mutant infections in terms of absolute cell numbers in a certain volume.

### 3.3. Parameterization of the population-based delay-differential equation model

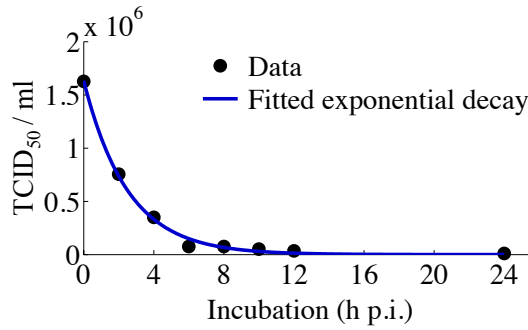


**Figure 3.17.:** Estimation of the rate constant of virus degradation  $d_V$ . The parameter determination of the rate constant of virus degradation  $d_V$  is based on a virus stability experiment, in which BHK-21 cells were incubated with DENV-faR virus particles and virus titers (black dots) were quantified by TCID<sub>50</sub> assay at the indicated time points post infection (p.i.). The data was fitted with an exponential decay equation (blue curve) by applying a trust-region-reflective least-squares algorithm with  $10^4$  different random initial values. The best fit resulted in  $d_V = 0.4/\text{h}$  together with an initial virus concentration of  $1.6 \times 10^6 \text{ TCID}_{50}/\text{ml}$ . (Experiments by Bianca Schmid and Ralf Bartenschlager)

At the beginning of the experiments, the ISG reporter cells were infected at a MOI of 0.1. Based on the definition of MOI given by

$$\text{MOI} = \frac{V_0}{S_0}, \quad (3.12)$$

and the initial number of naïve cells  $S_0 \sim 1500$  in the relevant experiments, we set the initial extracellular viral load  $V_0 \stackrel{(3.12)}{=} 0.1 \times 1500 = 150$  virus units/volume. This specification consequently means, that all other virus depending parameters can be determined up to a scaling factor.

In addition, we take advantage of an independently conducted virus stability experiment to obtain an estimate of the rate constant of virus degradation  $d_V$  (Figure 3.17). The DENV-faR-wt stability analysis was performed by infecting the IFN-incompetent baby hamster kidney cell line (BHK-21) with DENV-faR-wt and identifying the extracellular amount of virus by TCID<sub>50</sub> assay over time. According to the shape of the observed extracellular virus kinetic, we suppose an exponential virus decay and consider as objective function

$$\mathcal{V}(t) = V_0 e^{-d_V t} \quad (3.13)$$

for  $t \in \mathbb{R}$  with the initial condition  $\mathcal{V}(0) = V_0$ . To fit the parameters of the objective function (3.13) to the virus stability data, we utilized the trust-region-reflective least-squares algorithm of Matlab's optimization toolbox (Coleman and Zhang (2003)) and chose for the corresponding chi-squares statistic (2.34) a constant error of 1. After applying the optimization method with  $10^4$  different random initial values, the best fit yielded  $d_V = 0.4/\text{h}$  and provides a satisfying match with the data (cf. Figure 3.17, blue curve).

Moreover, we found that the formulation of the differential equation with respect to extracellular IFN given by

$$\dot{F}(t) = v_F I_F(t) - d_F F(t)$$

### 3. Viral fitness is mainly controlled by the effect of IFN on already infected cells

for  $t \in \mathbb{R}$ , leads to a correlation between the IFN secretion rate  $v_F$  and the rate constant of IFN degradation  $d_F$ . Thus, we set  $d_F = 0.15/\text{h}$  to the previously determined rate constant of IFN degradation of the stochastic model (cf. Table 2.1 in section 2.2.3).

For the parameter determination of the remaining model parameters, we use the time-resolved data set consisting of two independent flow cytometry measurements along with ELISA quantifications (cf. Figure 3.14 and 3.15) by comparing the following observed kinetics with the related model readouts (ROs) (Figure 3.18):

- (RO1) The total number of measured cells serves as a control and is described in our model by

$$A(t) = S(t) + I_m(t) + I_m(t) + P(t), \quad (3.14)$$

where  $A(t)$  denotes the overall number of cells in the system at time  $t \in \mathbb{R}$  and  $m \in \{\text{R}, \text{V}, \text{F}\}$ .

- (RO2) The number of experimentally identified IFIT1-deGFP - DENV-faR double-negative cells conform to the simulated cells  $\tilde{S}(t)$  defined as

$$\tilde{S}(t) = S(t) + I_{\bar{R}}(t). \quad (3.15)$$

$\tilde{S}(t)$  comprises both susceptible cells as well as already infected but not yet virus replicating cells, which implies that the DENV-faR fluorescence protein is not yet visible in the host cell.

- (RO3) The monitored DENV-faR positive cells corresponds to the calculated number of virus replicating cells  $I_R(t)$ .
- (RO4) The detected ISG expressing IFIT1-deGFP<sup>+</sup> - DENV-faR<sup>-</sup> cells comply with the computed number of protected cells  $P(t)$ .
- (RO5) Since IFN- $\lambda$  is the most prominent type of IFN in our cell system (Schmid (2014)), we consider the quantified level of secreted IFN- $\lambda$  as a reference for the simulated amount of released IFN  $F(t)$ .

To exploit both independently performed experiments, the model dynamics listed in (RO2)-(RO5) are simultaneously fitted to the related time course data of experiment 1 as well as experiment 2 by allowing only the initial number of susceptible cells  $S_0$  to be specific to each measurement, while all other parameters are identical for both experiments.

As optimization method we use the trust-region-reflective least-squares algorithm of Matlab's optimization toolbox (Coleman and Zhang (2003)) by calling the implemented Fortran program of our DDE system with a binary Matlab executable (mex) file. Since we compare several components of the model with their respective data, the chi-squares statistic  $\chi^2$  of the model parameters  $\theta_k$ ,  $k = 1, \dots, N_p$ , is given by

$$\chi^2(\theta_1, \dots, \theta_{N_p}) = \sum_{j=1}^{N_c} \sum_{i=1}^{N_t} \left( \frac{d_j(t_i) - y_j(t_i | \theta_1, \dots, \theta_{N_p})}{\sigma_j(t_i)} \right)^2, \quad (3.16)$$

### 3.3. Parameterization of the population-based delay-differential equation model

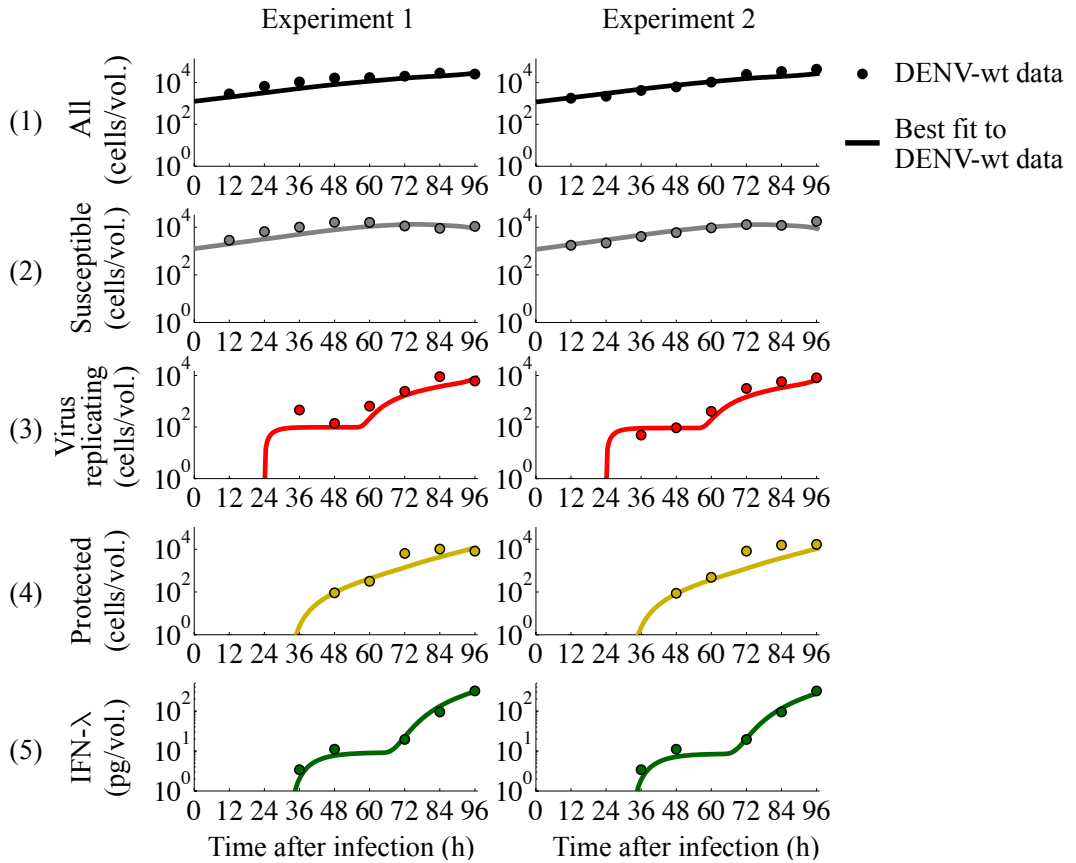


**Figure 3.18.:** Best fit of the mathematical model to two independent experiments concerning DENV-faR-wt infection. For parameter estimation we compared simulated with observed cell dynamics of (1) all (as control), (2) susceptible IFIT1-deGFP - DENV-faR-wt double-negative, (3) virus replicating DENV-faR-wt positive as well as (4) protected IFIT1-deGFP<sup>+</sup> - DENV-faR-wt<sup>-</sup> cells along with (5) IFN-λ release after infection of A549 IFIT1-deGFP reporter cells with DENV-faR-wt at a MOI of 0.1. The data set is based on two independently performed flow cytometry measurements (cf. Figure 3.14A), while IFN-λ was quantified in experiment 2 by ELISA (cf. Figure 3.15, colored in black). Absolute cell numbers can be considered as a volume (vol.) of 100  $\mu\text{l}$   consistently analyzed. The model was simultaneously fitted to both experiments by only allowing the initial number of susceptible cells to be specific to each measurement, whereas all other parameters are the same for both experiments. The best fit was obtained by using a trust-region-reflective least-squares algorithm with at least  $10^4$  different random initial values. (Experiments by Bianca Schmid and Ralf Bartenschlager)

where  $N_c$  denotes the number of model components  $y_j(t_i | \theta_1, \dots, \theta_{N_p})$  that describe the associated data set  $(t_i, d_j(t_i))$  at  $N_t$  observation times. For the measurement errors we assume a 10% deviation band referred to the measured kinetic data  through setting   $d_j(t_i) = 0.1 d_j(t_i)$  for  $i = 1, \dots, N_t$  and  $j = 1, \dots, N_c$ . To find a reliable best fit parameter set of our optimization problem

$$\min_{\{\theta_k | k=1, \dots, N_p\}} (\chi^2(\theta_1, \dots, \theta_{N_p})), \quad (3.17)$$

the least-squares minimization has to be repeated for a large number of different random initial values. Although it turned out that the simulation of the DDE

### 3. Viral fitness is mainly controlled by the effect of IFN on already infected cells

model (3.11) using the RADAR5 solver written in Fortran is considerably less time consuming as our stochastic model based on Gillespie's algorithm (cf. 2.2 - 2.3), the calculation of our DDE system is still slower than solving comparable large ODE systems. Therefore we utilized Matlab's parallel computing toolbox to run several optimization processes simultaneously on a Mac OS X based computer cluster. Since this cluster can execute 240 individual sessions in parallel, we were able to repeat the optimization procedure for more than  $10^4$  different random initial values. The resulting best fit correctly reproduces the observed kinetic data of both experiments (Figure 3.18).

In order to assess the uncertainties of the best fit parameter values, we calculate likelihood-based confidence intervals for the estimated parameters by applying the profile likelihood method (Venzon and Moolgavkar (1988)). Likelihood-based confidence regions dependent on a threshold in the likelihoods  $Q_{\chi^2}(1-a, DF)$ , which represents the  $(1-a)$  quantile of the  $\chi^2$ -distribution with  $DF$  degrees of freedom. As we aim to compute the confidence bound of each individual parameter, the degree of freedom in this case is equal to 1. The  $(1-a)$  confidence interval of a single parameter  $\theta_l$ ,  $l \in \{1, \dots, N_p\}$ , encloses a set of parameter values  $\nu$  and is defined as

$$CI_{1-a}(\theta_l) = \{\nu \mid \Delta\chi_{\theta_l}^2(\nu) \leq Q_{\chi^2}(1-a, 1)\}, \quad (3.18)$$

with

$$\begin{aligned} \Delta\chi_{\theta_l}^2(\nu) &= \min_{\{\theta_k | k=1, \dots, N_p; k \neq l\}} (\chi^2(\theta_1, \dots, \theta_{l-1}, \nu, \theta_{l+1}, \dots, \theta_{N_p})) \\ &\quad - \min_{\{\theta_k | k=1, \dots, N_p\}} (\chi^2(\theta_1, \dots, \theta_{N_p})). \end{aligned} \quad (3.19)$$

To compute

$$\min(\chi_{\theta_l \text{fix}}^2) := \min_{\{\theta_k | k=1, \dots, N_p; k \neq l\}} (\chi^2(\theta_1, \dots, \theta_{l-1}, \nu, \theta_{l+1}, \dots, \theta_{N_p})) \quad (3.20)$$

from equation (3.19), we fix the parameter  $\theta_l$ ,  $l \in \{1, \dots, N_p\}$  systematically to different values  $\nu$  around the estimated optimum and solve the minimization problem with respect of the remaining parameters  $\{\theta_k \mid k = 1, \dots, N_p; k \neq l\}$ . Afterwards, the term  $\Delta\chi_{\theta_l}^2(\nu)$  (cf. (3.19)) is obtained by subtracting the fitted  $\chi^2$ -value minimized over all parameters (3.17) from the calculated  $\min(\chi_{\theta_l \text{fix}}^2)$ -value. The most common confidence regions  $CI_{95\%}$  and  $CI_{68\%}$  follow from equation (3.18) by taking into account the corresponding quantiles of the  $\chi^2$ -distribution  $Q_{\chi^2}(95\%, 1) = 3.8$  and  $Q_{\chi^2}(68\%, 1) = 1$ , respectively. By plotting  $\Delta\chi_{\theta_l}^2(\nu)$  and detecting those values  $\nu$  for which  $\Delta\chi_{\theta_l}^2$  remain below the respective quantile-based thresholds, the confidence intervals can be determined directly from the graph of the profile likelihood.

The application of the profile likelihood method for our model regarding the parameters that were estimated based on the kinetic DENV-wt data set shown in Figure 3.18, reveal the identifiability of all these parameters within narrow confidence bounds (Figure 3.19 and Table 3.1). Since the model is constrained by experimental DENV-wt data, we can utilize our population-based model to make quantitative predictions about the competition between spreading DENV and IFN-induced antiviral protection.

### 3.3. Parameterization of the population-based delay-differential equation model

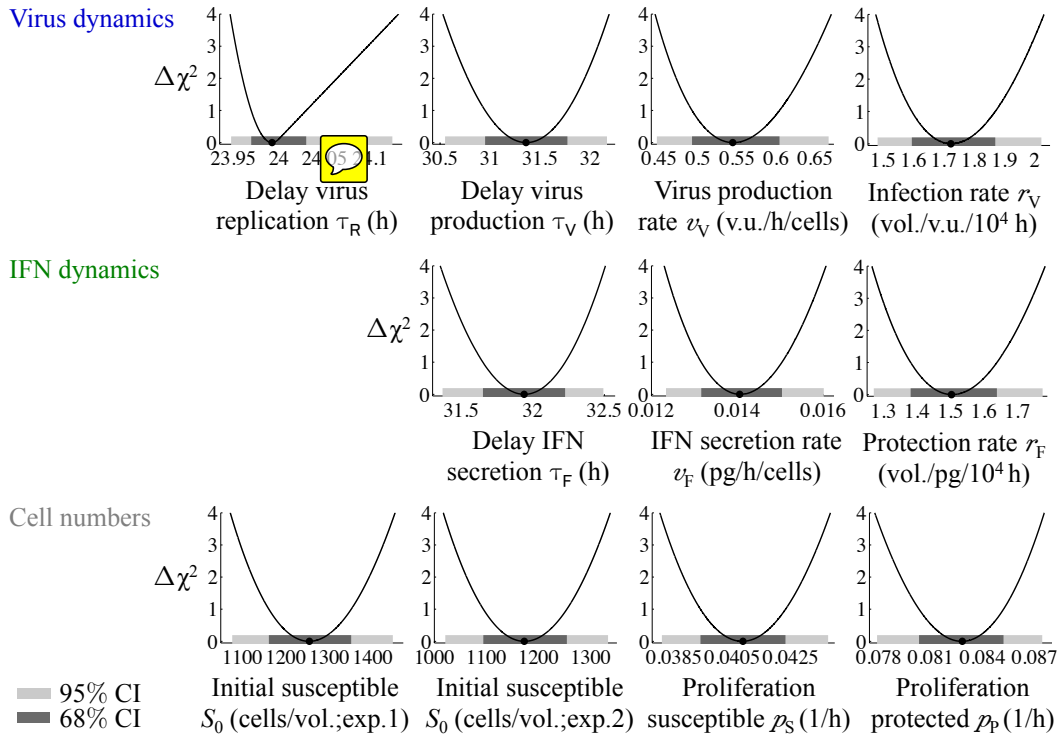


**Figure 3.19.:** Profile likelihoods demonstrate that the model parameters are identified by DENV-wt data. The profile likelihood method was applied to determine the 95% (bright gray band; cf. Table 3.1) and 68% (dark gray band) confidence interval (CI) of all model parameters, which were estimated using the kinetic DENV-wt data set shown in Figure 3.18. The plots illustrate the change of the  $\chi^2$ -function ( $\Delta\chi^2$ , y-axis) of the indicated parameter (x-axis) calculated according to equation (3.19). Abbreviations: experiment (exp.), hours (h), picogram (pg), volume (vol.), virus units (v.u.).

To verify the validity of our parameterized model, we examine whether key parameter values are consistent with the results of independent measurements. Since we suspect that timing is an important factor in the antiviral immune defense, our focus rests on the estimates of the three time delays.

The determined mean latency of virus replication  $\tau_R$  of 24 h (cf. Figure 3.19, first profile likelihood in the upper row and Table 3.1) is mainly influenced by fitting the virus replicating cells  $I_R(t)$  to the DENV-faR-wt positive IFIT1 reporter cells after low dose infection (cf. (RO3) on page 62 and Figure 3.18(3)). Thus,  $\tau_R$  should comply with the mean expression onset of virus replication in individual IFIT1-deGFP reporter cells after infection with DENV-faR-wt at a low MOI monitored by live-cell imaging (cf. Figure 3.10B). In this time-lapse microscopy experiment DENV-faR-wt<sup>+</sup> reporter cells became visible in the time period between [22.0 h p.i.; 68.0 h p.i.] with a mean onset of 32.2 h post infection. Hence, the time delay  $\tau_R$  corresponds to the initial detection of virus replication in real time at single-cell level.

For testing the estimated latency of virus production  $\tau_V = 31.4$  h (cf. Figure 3.19, second profile likelihood in the upper row and Table 3.1), we relate this time delay with the halftime of DENV particle release after high dose infection quantified in

### 3. Viral fitness is mainly controlled by the effect of IFN on already infected cells

Model parameter	Value [95% CI]	
<b>Virus dynamics</b>		
Initial viral load	$V_0$	150 v.u./vol.
Mean latency of virus replication	$\tau_R$	24.0[23.9;24.1] h
Mean latency of virus production	$\tau_V$	31.4[30.6;32.2] h
Virus production rate	$v_V$	0.54[0.45;0.67] v.u./h/cells
Infection rate	$r_V$	$1.7 \times 10^{-4}$ [ $1.5 \times 10^{-4}$ ; $2.0 \times 10^{-4}$ ] vol./v.u./h
Virus degradation rate	$d_V$	0.4/h
<b>IFN dynamics</b>		
Mean latency of IFN secretion	$\tau_F$	31.9[31.4;32.5] h
IFN secretion rate	$v_F$	0.014[0.012;0.016] pg/h/cells
Protection rate	$r_F$	$1.5 \times 10^{-4}$ [ $1.3 \times 10^{-4}$ ; $1.8 \times 10^{-4}$ ] vol./pg/h
IFN degradation rate	$d_F$	0.15/h
Cell numbers		
Initial susceptible cells (exp. 1)	$S_0$	1254 [1076;1446] cells/vol.
Initial susceptible cells (exp. 2)	$S_0$	1172 [1021;1333] cells/vol.
Proliferation rate susceptible cells	$p_S$	0.041[0.038;0.044] 1/h
Proliferation rate protected cells	$p_P$	0.083[0.078;0.087] 1/h

**Table 3.1.:** Model parameter estimates of the population-based DDE model. According to the biological meaning of the model parameters (cf. section 3.2), we estimated the parameter values as depicted in section 3.3.1 by considering only experiments regarding DENV-wt infection. Given are the best fit values and the 95% confidence intervals (calculated with the profile likelihood method) after fitting of the model to the time-resolved data set shown in Figure 3.18 under the usage of a fixed initial viral load along with separately determined values for virus and IFN degradation rates. All model simulations concerning DENV-wt refer to this parameter set. Abbreviations: confidence interval (CI), experiment (exp.), hours (h), picogram (pg), virus units (v.u.), volume (vol.).

short time frames by TCID<sub>50</sub> assay (cf. blue curve in Figure 3.7). A direct comparison demonstrate that the predicted time delay  $\tau_V$  accurately reflects the measured halftime of  $\sim 32$  h (Figure 3.20A). Moreover, the single-step growth curves in the upper panel of Figure 3.7 enable the extrapolation of the first appearance of replicated viral RNA and released DENV in an entirely infected cell population. Although these approximated values of  $\sim 8$  h and  $\sim 14$  h for the onset of virus replication and DENV production, respectively, are much shorter than the respective model estimates, the time difference of  $\sim 6$  h between the two events agrees with the predicted lag of  $\tau_V - \tau_R = 31.4 - 24 = 7.4$  h. The consistency between the predicted and detected mean latency of virus production post infection as well as after onset of virus replication is especially noteworthy, since the DDE system as a whole was fitted without using data of extracellular virus dynamics (cf. Figure 3.18).

Furthermore, the single-step growth curve of secreted IFN- $\lambda$  after infection with DENV-faR-wt at a high MOI (cf. dark green curve in Figure 3.7) serve as a control experiment for the determined mean latency of IFN secretion  $\tau_F = 31.9$  h (cf. Figure 3.19, first profile likelihood in the second row and Table 3.1). By comparing  $\tau_F$  with the measured halftime of IFN- $\lambda$  release of  $\sim 26.5$  h, we found that the model

### 3.3. Parameterization of the population-based delay-differential equation model

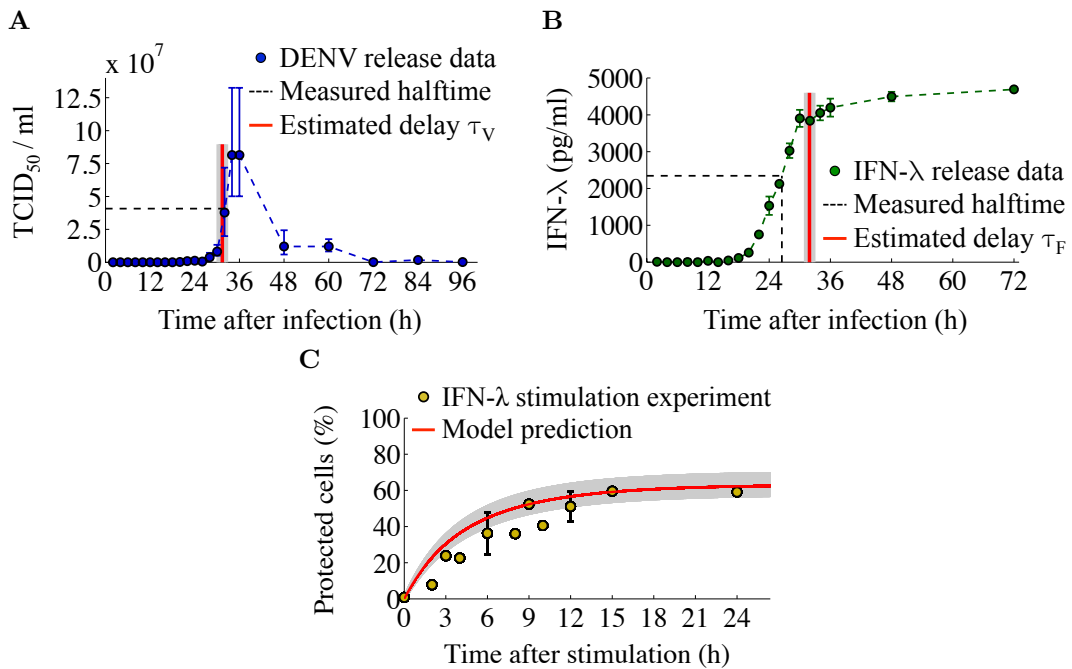


**Figure 3.20.:** The estimated parameter values of virus production time, IFN secretion delay and IFN response agree with independently measured **yellow** data. (A, B) IFN-competent A549 cells were infected with DENV-faR-wt at a MOI of 10 and analyzed at the indicated time points post infection. (A) Extracellular virus (blue color) was detected by TCID<sub>50</sub> assay. Highlighted are the observed halftime of  $\sim 32$  h (dashed black line) and the estimated mean latency of virus production  $\tau_V = 31.4$  h (red line with shaded 95% confidence interval [30.6 h; 32.2 h]; data replotted from Figure 3.7 on linear scale). (B) Extracellular IFN-λ (dark green color) was quantified by ELISA. Marked are the observed halftime of  $\sim 26.5$  h (dashed black line) and the estimated mean latency of IFN secretion  $\tau_F = 31.9$  h (red line with shaded 95% confidence region [31.4 h; 32.5 h]; data replotted from Figure 3.7). (C) A549 IFIT1-deGFP reporter cells were stimulated with 10 ng/ml IFN-λ and subjected to flow cytometry at the displayed times after treatment. Plotted are the experimentally observed rise in IFIT1-deGFP<sup>+</sup> cells (yellow dots) and the predicted increase in protected cells (red line with shaded 95% confidence bound) simulated with the submodel (3.21) by assuming an initial stimulation with IFN (data replotted from Figure 3.8B). (Experiments by Bianca Schmid and Ralf Bartenschlager)

prediction provides a reasonably close approximation (Figure 3.20B).

As already mentioned in section 3.2 (page 56), the single-step growth curves illustrate the temporal distribution of heterogeneous single-cell behavior, which we roughly approximated with constant time delays. However, the fact that the strict time delays of virus replication, virus production and IFN secretion of the parameterized model, match independent observed times at which infected cells become visibly infected and reach their half-maximal virus as well as IFN production rate, confirms the ability of the model to make quantitative predictions of cell population dynamics.

In addition to the time delays, we also examine the parameterized IFN response in the model under the usage of a previously described IFN stimulation experiment, in which A549 IFIT1-deGFP reporter cells were treated with IFN-λ (cf. green curve

### 3. Viral fitness is mainly controlled by the effect of IFN on already infected cells

in Figure 3.8B). To imitate the initial conditions of this experiment, we consider a number of susceptible cells  $S_0$  along with the applied extracellular IFN concentration  $F_0 = 10 \text{ ng/ml} = 1000 \text{ pg}/100\mu\text{l} = 1000 \text{ pg/volume}$ . For the simulation of the IFN response, we assume that the recognition of extracellular IFN  $F$  turn susceptible cells  $S$  into protected cells  $P$  with the protection rate  $r_F$ . The removal of IFN by cellular uptake and, to a lesser extent, by extracellular degradation is taken into account through the IFN degradation rate  $d_F$ . The dynamics of this small submodel at time  $t \in \mathbb{R}$  is defined by the following ODE system:

$$\begin{aligned}\dot{S}(t) &= -r_F F(t) S(t) & S(0) &= S_0 \\ \dot{P}(t) &= r_F F(t) S(t) & P(0) &= 0 \\ \dot{F}(t) &= -d_F F(t) & F(0) &= 1000 \text{ pg/volume.}\end{aligned}\tag{3.21}$$

For the model parameters  $S_0, r_F$  as well as  $d_F$ , we choose the fitted parameter values given in Table 3.1. The ODE system (3.21) was solved by using a standard ODE solver of MATLAB that is based on the explicit Runge-Kutta method of Bogacki and Shampine (Bogacki and Shampine (1989), Shampine and Reichelt (1997)). The direct comparison shows a good agreement between the simulated fraction of protected cells and the observed IFN-responding cells (Figure 3.20C).

Taken together, the validity of the model is corroborated by the parameterization within narrow confidence intervals under the usage of DENV-wt data and, additionally, by the consistency with key results obtained in independent experiments that were not utilized for model fitting.

#### 3.3.2. Detection of DENV mutant specific model parameters by utilizing the knowledge from wt-fitting

In order to analyze the differences between DENV-wt and attenuated DENV-E217A mutant infections on a quantitative level, we utilize the population-based model parameterized exclusively with DENV-wt data (cf. section 3.3.1) to identify DENV-E217A mutant specific parameters, which are able to describe the observed population dynamics after DENV-faR-E217A mutant infection (cf. Figure 3.14B and 3.15).

In consideration of findings from the literature, we argue that four parameters might vary between DENV-wt and DENV-E217A mutant infections. Since studies demonstrate an inhibited translation of mutant RNA caused by IFIT1 (Pichlmair et al. (2011), Habjan et al. (2013)), the generation of new infectious virus particles could take longer or occur at a lower rate. Moreover, as other reports show that 2'-O-unmethylated RNA is detected more readily by intracellular pattern recognition receptors (Züst et al. (2011)), infected cells might produce IFN faster or to a larger extent.

For the parameter optimization regarding DENV-E217A mutant infection, we take advantage of the established DENV-wt parameter set (cf. Table 3.1) and estimate only the four just mentioned potentially DENV-E217A mutant specific parameters (MP) in line with their respective constraints:

### 3.3. Parameterization of the population-based delay-differential equation model

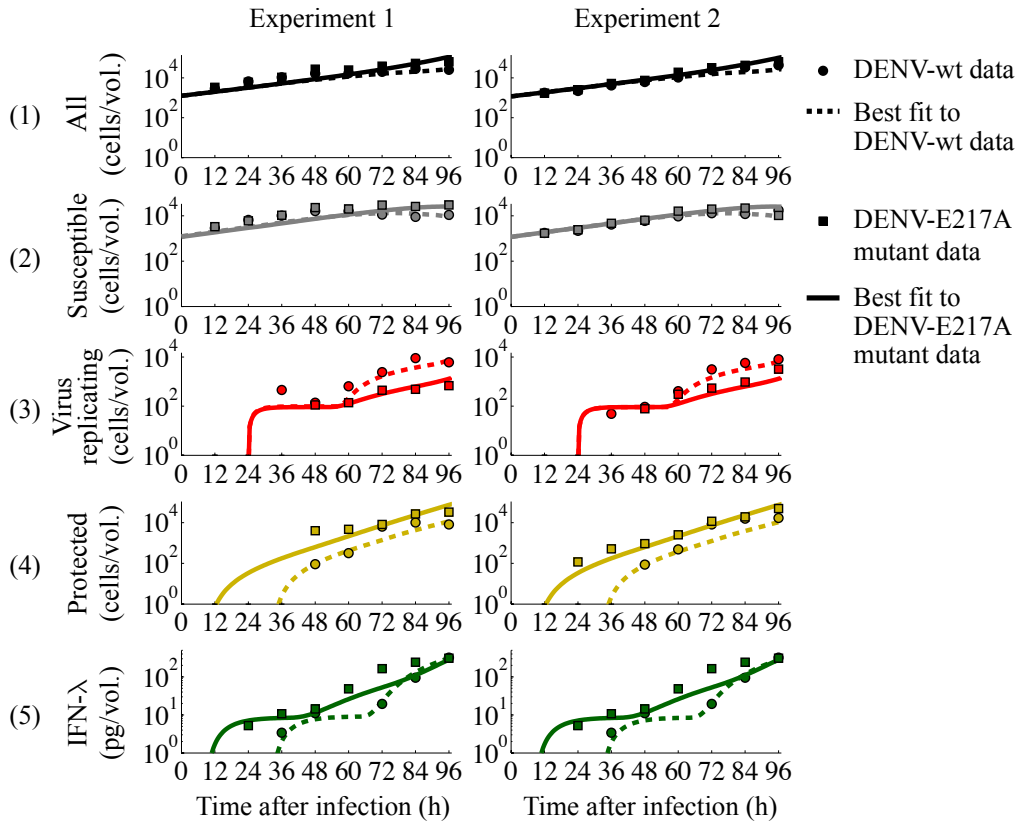


**Figure 3.21.:** Best fit of the mathematical model to two independent experiments concerning DENV-faR-E217A mutant infection by utilizing the DENV-wt parameter estimates. For parameter optimization we compared simulated with observed cell dynamics of (1) all (as control), (2) susceptible IFIT1-deGFP - DENV-faR double-negative, (3) virus replicating DENV-faR positive as well as (4) protected IFIT1-deGFP<sup>+</sup> - DENV-faR<sup>-</sup> cells along with (5) IFN- $\lambda$  release after infection of A549 IFIT1-deGFP reporter cells with DENV-faR at a MOI of 0.1. The data set is based on two independently performed flow cytometry measurements (cf. Figure 3.14), while IFN- $\lambda$  was quantified in experiment 2 by ELISA (cf. Figure 3.15). Absolute cell numbers can be considered as a volume (vol.) of 100  $\mu$ l was consistently analyzed. Initially, the model simulations concerning DENV-wt (dashed lines) were adapted to the respective time-resolved DENV-wt data (circles). The resulting DENV-wt parameter estimates (cf. section 3.3.1 and Table 3.1) were used to optimize the DENV-E217A mutant specific parameters (MP1)-(MP4) (cf. page 68) by fitting the model dynamics concerning DENV-E217A mutant (solid lines) simultaneously to the related DENV-E217A mutant kinetics (squares) of both independent experiments. The best fit was obtained by applying a trust-region-reflective least-squares algorithm with at least  $5 \times 10^3$  different random initial values. (Experiments by Bianca Schmid and Ralf Bartenschlager)

(MP1) Mean latency of mutant virus production  $\tau_{V\text{mut}} > \tau_R$

(MP2) Mutant virus production rate  $v_{V\text{mut}} \leq v_V$

(MP3) Mean latency of IFN secretion after mutant virus infection  $\tau_{F\text{mut}}$

(MP4) IFN secretion rate after mutant virus infection  $v_{F\text{mut}} \geq v_F$ .

In the same way as in the DENV-wt case, we determine the DENV-E217A mutant

3. Viral fitness is mainly controlled by the effect of IFN on already infected cells

Model parameter		Value [95% CI]
<b>Virus dynamics</b>		
Mean latency of virus production (wt)	$\tau_V$	31.4[30.6;32.2] h
Mean latency of virus production (mutant)	$\tau_{V\text{mut}}$	28.3[26.8;29.7] h
Virus production rate (wt)	$v_V$	0.540[0.45;0.670] v.u./h/cells
Virus production rate (mutant)	$v_{V\text{mut}}$	0.067[0.06;0.074] v.u./h/cells
<b>IFN dynamics</b>		
Mean latency of IFN secretion (wt)	$\tau_F$	31.9[31.4;32.5] h
Mean latency of IFN secretion (mutant)	$\tau_{F\text{mut}}$	8.2[ 7.5; 9.1] h
IFN secretion rate (wt)	$v_F$	0.014[0.012;0.016] pg/h/cells
IFN secretion rate (mutant)	$v_{F\text{mut}}$	0.014[0.014;0.015] pg/h/cells

**Table 3.2.:** Optimized model parameters of the population-based DDE model which differ between DENV-wt and DENV-E217A mutant infection. After the model parameterization by considering only DENV-wt related experiments (cf. section 3.3.1 and Table 3.1), data concerning DENV-E217A mutant infection were fitted by allowing only four parameters to differ between DENV-wt and DENV-E217A mutant (cf. section 3.3.2). Given are the best fit values and the 95% confidence intervals (calculated with the profile likelihood method) of these four infection specific parameters after fitting of the model to the time-resolved data set shown in Figure 3.21. Abbreviations: confidence interval (CI), DENV- E217A mutant (mut), DENV-wt (wt), hours (h), picogram (pg), virus units (v.u.).

specific parameters (MP1)-(MP4), by fitting the model dynamics listed in (RO2)-(RO5) (cf. section 3.3.1 page 62) simultaneously to the related time-resolved data set consisting of two independent flow cytometry measurements along with ELISA quantifications post DENV-faR-E217A mutant infection (cf. Figure 3.21(2)-(5)).

While retaining the proven optimization method based on the trust-region-reflective least-squares algorithm of Matlab's optimization toolbox (Coleman and Zhang (2003)) and assuming for the corresponding chi-squares statistic (3.16) a measurement error of 10%, we repeated the optimization procedure for more than  $5 \times 10^3$  different random initial values. The obtained best fit provides a good match with the observed kinetics after DENV-faR-E217A mutant infection of both experiments (cf. Figure 3.21).

By applying the profile likelihood method, we calculate the 95% confidence intervals of the estimated DENV-E217A mutant specific parameters (MP1)-(MP4) according to the formula (3.18). The resulting narrow confidence bounds confirm the identifiability of all four parameters. But more importantly, the comparison of the confidence regions reveal that only two of the four DENV-E217A mutant specific parameters differ strongly from their DENV-wt values: The mean latency of IFN secretion is  $\sim 24$  h shorter and the virus production rate is  $\sim 8$ -fold lower after DENV-E217A mutant infection in contrast to DENV-wt (Table 3.2 and Figure 3.22).

Obviously, both identified DENV-E217A mutant specific parameters could contribute to the observed attenuated spread of the 2'-O-unmethylated mutant, but their relative importance is still open. In section 3.5, we will analyze the antiviral effect of the DENV-E217A mutant specific parameters in detail by using an extended

### 3.4. Model extension to analyze explicitly the autocrine and paracrine effect of IFN

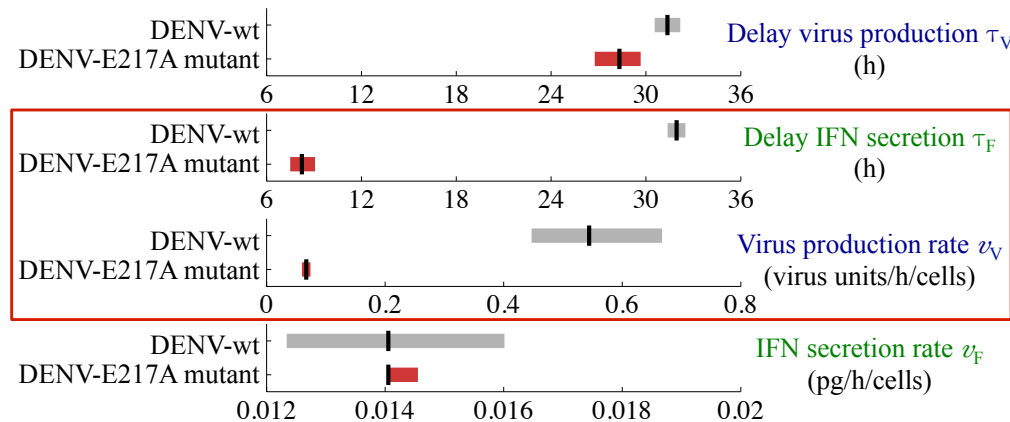


**Figure 3.22.:** The difference between DENV-wt and attenuated DENV-E217A mutant infection is mainly based on an accelerated IFN induction and a decreased virus production triggered by the 2'-O-unmethylated mutant. The direct comparison of the estimated best fit values (vertical black lines) and the corresponding 95% confidence intervals (bands; calculated with the profile likelihood method) of the four model parameters (right y-axis), which have been allowed to differ between DENV-wt and DENV-E217A mutant infection (left y-axis) demonstrate that only the mean latency of IFN secretion  $\tau_F$  and the virus production rate  $v_V$  differ considerably (framed in dark red color).

version of the model, which is described in the following section 3.4.

### 3.4. Extension of the population-based model to analyze explicitly the autocrine and paracrine effect of IFN

The prediction of the data-based quantitative model, that a decreased virus production and an accelerated IFN induction make the difference between DENV-wt and the attenuated DENV-E217A mutant (cf. Figure 3.22), raises the questions how much impact both factors individually have on the outcome of infection, or even if the two factors are possibly related to each other? The latter question is prompted by our observation that stimulation of infected cells with IFN in an early phase after infection causes a reduction of virus replication and consequently virus production (cf. Figure 3.5). However, this autocrine effect of IFN must be temporally limited, since stimulation with IFN has no further influence after a certain time period post infection.

To analyze explicitly the impact of IFN on infected cells, we expand our established model (3.11) by assuming that recognition of IFN with the rate  $r_P$ , in the time window of IFN permissiveness  $\tau_P$  after viral entry, inhibits the production of new infectious virus particles (Figure 3.23, solid green inhibition link). Technically, we calculate the probability of infected cells to sense secreted IFN in the time period  $\tau_P$  by applying a technique from the field of the survival analysis (Cox and Oakes (1984), Dobson (2001), Rodriguez (2007)).

3. Viral fitness is mainly controlled by the effect of IFN on already infected cells

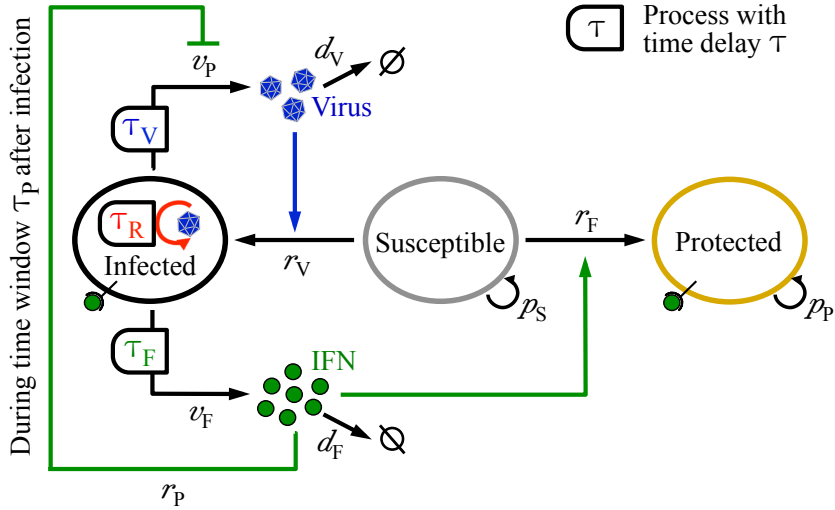


**Figure 3.23.:** Scheme of the full population-based model, which describes the competition between spreading virus and the antiviral immune response induced in a paracrine and temporally limited autocrine manner by secreted IFN. Susceptible cells (gray oval) can become infected by extracellular virus with the infection rate  $r_V$  (blue arrow). Virus replication ( $\bigcirc$ ) initiates in infected cells (black oval) at time  $\tau_R$  after viral entry (red color) and results in virus production with the virus production rate  $v_V$  from time  $\tau_V > \tau_R$  onwards. Moreover, infected cells start to express IFN with the secretion rate  $v_F$  at time  $\tau_F$  post viral infestation. Recognition of secreted IFN turn susceptible cells into protected cells (yellow oval) with the protection rate  $r_F$  (solid green arrow). In addition, sensing of IFN with the rate  $r_P$  in the time window  $\tau_P$  after viral entry inhibits virus production in infected cells (solid green inhibition link). Extracellular virus and IFN are removed ( $\emptyset$ ) by cellular uptake as well as extracellular degradation with the rate constant of virus degradation  $d_V$  and the rate constant of IFN degradation  $d_F$ . While propagation is inhibited in infected cells, susceptible and protected cells proliferate ( $\circlearrowright$ ) with the rates  $p_S$  and  $p_P$ , respectively.

For this purpose we firstly consider a non-negative, continuous random variable  $T$ , which represents the waiting time until an infected cell recognizes IFN. Taking into account the time depending density function of  $T$   $f_T$ , the cumulative distribution function (*CDF*) of  $T$  is defined by

$$CDF_T(\tilde{t}) = \mathcal{P}(T \leq \tilde{t}) \quad (3.22)$$

$$\stackrel{T \text{ continuous}}{=} \int_0^{\tilde{t}} f_T(x) dx \quad (3.23)$$

and describes the probability  $\mathcal{P}$  to recognize IFN within the time span  $\tilde{t} \in \mathbb{R}_{\geq 0}$ .

Accordingly, the complement of  $CDF_T$

$$\mathcal{Z}_T(\tilde{t}) = 1 - CDF_T(\tilde{t}) \quad (3.24)$$

$$\stackrel{(3.22)}{=} \mathcal{P}(T > \tilde{t}) \quad (3.25)$$

$$\stackrel{(3.23)}{=} \int_{\tilde{t}}^{\infty} f_T(x) dx,$$

### 3.4. Model extension to analyze explicitly the autocrine and paracrine effect of IFN

with the initial condition

$$\mathcal{Z}_T(0) \stackrel{(3.24)}{=} 1 - CDF_T(0) \stackrel{(3.23)}{=} 1, \quad (3.26)$$

is the probability that IFN was not sensed within the time period  $\tilde{t}$ . In the survival analysis,  $\mathcal{Z}_T$  is known as the “survival function”. The derivative of  $\mathcal{Z}_T$

$$\begin{aligned} \mathcal{Z}'_T(\tilde{t}) &\stackrel{(3.24)}{=} -CDF'_T(\tilde{t}) \\ &\stackrel{(3.23)}{=} -f_T(\tilde{t}) \end{aligned} \quad (3.27)$$

is equal to the negative value of the density function of  $T$ .

In addition, we need the so-called hazard function, which is the time depending probability rate of recognizing IFN in an infinitesimally small time interval  $[\tilde{t}; \tilde{t} + d\tilde{t}]$  under the condition that there was no stimulation through IFN up to time  $\tilde{t}$ . The hazard function is generally defined by

$$\begin{aligned} h(\tilde{t}) &= \lim_{d\tilde{t} \rightarrow 0} \left( \frac{\mathcal{P}(\tilde{t} \leq T < \tilde{t} + d\tilde{t} \mid T \geq \tilde{t})}{d\tilde{t}} \right) \\ &= \lim_{d\tilde{t} \rightarrow 0} \left( \frac{\mathcal{P}(\tilde{t} \leq T < \tilde{t} + d\tilde{t} \cap T \geq \tilde{t})}{d\tilde{t}} \right) \frac{1}{\mathcal{P}(T \geq \tilde{t})} \\ &\stackrel{T \text{ continuous}}{=} \lim_{d\tilde{t} \rightarrow 0} \left( \frac{\mathcal{P}(\tilde{t} \leq T < \tilde{t} + d\tilde{t})}{d\tilde{t}} \right) \frac{1}{\mathcal{Z}_T(\tilde{t})} \\ &\stackrel{T \text{ continuous}}{=} \lim_{dt \rightarrow 0} \left( \frac{CDF_T(\tilde{t} + dt) - CDF_T(\tilde{t})}{dt} \right) \frac{1}{\mathcal{Z}_T(\tilde{t})} \\ &\stackrel{\text{difference quotient}}{=} \frac{CDF'_T(\tilde{t})}{\mathcal{Z}_T(\tilde{t})} \\ &\stackrel{(3.23)}{=} \frac{f_T(\tilde{t})}{\mathcal{Z}_T(\tilde{t})} \\ &\stackrel{(3.27)}{=} -\frac{\mathcal{Z}'_T(\tilde{t})}{\mathcal{Z}_T(\tilde{t})}. \end{aligned} \quad (3.28)$$

In order to obtain a formula of  $\mathcal{Z}_T$  depending on the hazard function we reformulate equation (3.28) by integrating both sides:

$$\begin{aligned} h(\tilde{t}) &= -\frac{\mathcal{Z}'_T(\tilde{t})}{\mathcal{Z}_T(\tilde{t})} \\ \iff h(\tilde{t}) &= -\frac{d}{d\tilde{t}} (\ln(\mathcal{Z}_T(\tilde{t}))) \\ \iff \int_0^{\tilde{t}} h(x)dx &= -(\ln(\mathcal{Z}_T(\tilde{t})) - \ln(\mathcal{Z}_T(0))) \\ \stackrel{(3.26)}{\iff} -\int_0^{\tilde{t}} h(x)dx &= \ln(\mathcal{Z}_T(\tilde{t})) \\ \iff \mathcal{Z}_T(\tilde{t}) &= \exp \left( - \int_0^{\tilde{t}} h(x)dx \right). \end{aligned} \quad (3.29)$$

3. Viral fitness is mainly controlled by the effect of IFN on already infected cells

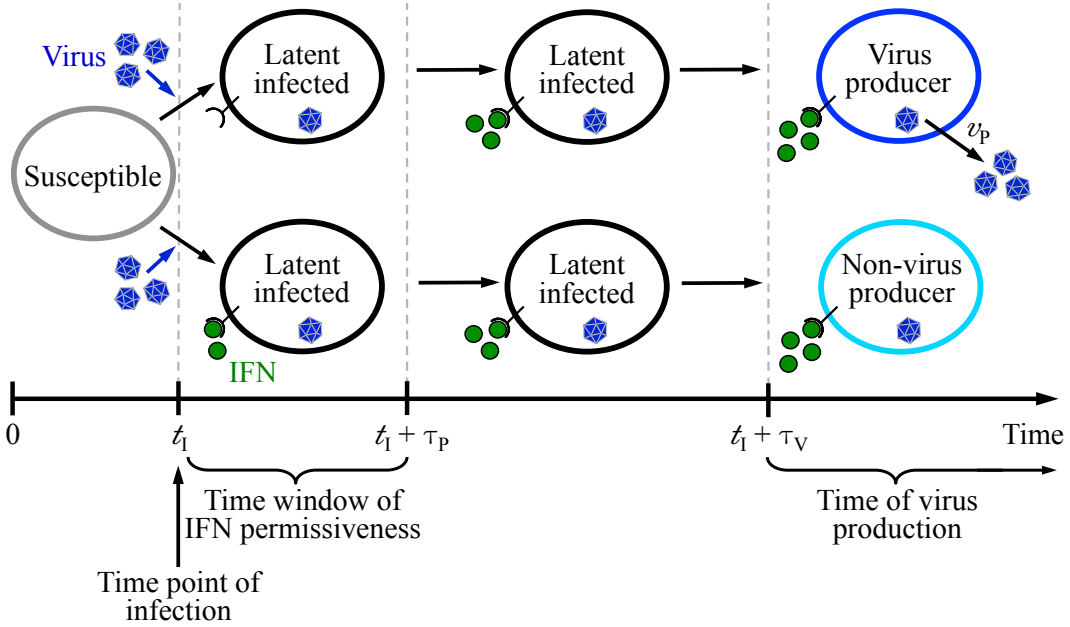


**Figure 3.24.:** Scheme of the modeled antiviral effect of IFN on already infected cells. To incorporate in our model an antiviral impact of IFN on infected cells, we assume after the time point of infection  $t_I$  of susceptible cells (gray oval) an IFN permissive time window  $\tau_P$ . Latent infected cells (black oval), which receive no IFN stimulus in the time interval  $[t_I; t_I + \tau_P]$  become at  $t_I + \tau_V$  virus producing cells (blue oval) and release new infectious viral particles with the rate constant  $v_P$  (upper sequence). In contrast, virus production is inhibited in latent infected cells, which recognize IFN in the time frame  $[t_I; t_I + \tau_P]$  (light blue oval; lower sequence).

In our case, the probability rate of recognizing IFN is given by

$$h(t) = r_P F(t), \quad (3.30)$$

where  $r_P$  denotes the rate of IFN-induced inhibition of virus production and  $F(t)$  is the time-dependent amount of extracellular IFN (cf. Figure 3.23, solid green inhibition link).

The distinction between infected cells, which are stimulated by IFN within the time window  $\tau_P$  after viral entry and those infected cells which are not relevant at the mean latency of virus production  $\tau_V$  after the time point of infection  $t_I \geq 0$  (Figure 3.24) and corresponds to the time

$$\begin{aligned} t &= t_I + \tau_V \\ \iff t - \tau_V &= t_I. \end{aligned} \quad (3.31)$$

Therefore, we compute the probability that IFN is not recognized up to the time

$$t_I + \tau_P \stackrel{(3.31)}{=} t - \tau_V + \tau_P \quad (3.32)$$

under the condition that there was no stimulation through IFN before the time point of viral entry. The condition is necessary, since sensing of IFN before infection leads

### 3.4. Model extension to analyze explicitly the autocrine and paracrine effect of IFN

to antiviral protection in our model. The probability of an infected cell to produce virus without antiviral IFN action is thus calculated by

$$\begin{aligned}
& \mathcal{P}(T > t_I + \tau_P \mid T > t_I) \stackrel{(3.32)}{=} \mathcal{P}(T > t - \tau_V + \tau_P \mid T > t - \tau_V) \\
& = \frac{\mathcal{P}(T > t - \tau_V + \tau_P \cap T > t - \tau_V)}{\mathcal{P}(T > t - \tau_V)} \\
& = \frac{\mathcal{P}(T > t - \tau_V + \tau_P)}{\mathcal{P}(T > t - \tau_V)} \\
& \stackrel{(3.25)}{=} \frac{\mathcal{Z}_T(t - \tau_V + \tau_P)}{\mathcal{Z}_T(t - \tau_V)} \\
& \stackrel{(3.29)}{=} \exp \left( - \int_0^{t - \tau_V + \tau_P} h(x) dx \right) \exp \left( \int_0^{t - \tau_V} h(x) dx \right) \\
& \stackrel{(3.30)}{=} \exp \left( - \int_0^{t - \tau_V + \tau_P} r_P F(x) dx \right) \exp \left( \int_0^{t - \tau_V} r_P F(x) dx \right) \\
& = \exp \left( -r_P \int_{t - \tau_V}^{t - (\tau_V - \tau_P)} F(x) dx \right) \\
& = \exp(r_P [\mathcal{F}(t - \tau_V) - \mathcal{F}(t - (\tau_V - \tau_P))]), \quad (3.33)
\end{aligned}$$

where  $\mathcal{F}$  denotes the antiderivative of  $F$ .

The probability (3.33) enables the separation between infected cells  $I_{V\bar{P}}$ , which receive no IFN stimulus and thus produce virus with the rate constant  $v_P$  and infected, non-virus producing cells  $I_{VP}$ , which recognize IFN within the time window  $\tau_P$  (cf. Figure 3.24). Accordingly, we include  $I_{V\bar{P}}$ ,  $I_{VP}$  and  $\mathcal{F}$  in our DDE model (3.11) and obtain the following DDE system with four time delays:

$$\begin{aligned}
\dot{S}(t) &= -r_V V(t) S(t) - r_F F(t) S(t) + p_S S(t) \\
\dot{I}_{\bar{R}}(t) &= r_V V(t) S(t) - r_V V(t - \tau_R) S(t - \tau_R) \\
\dot{I}_R(t) &= r_V V(t - \tau_R) S(t - \tau_R) \\
\dot{I}_{\bar{V}}(t) &= r_V V(t) S(t) - r_V V(t - \tau_V) S(t - \tau_V) \\
\dot{I}_{V\bar{P}}(t) &= \exp(r_P [\mathcal{F}_1(t) - \mathcal{F}_2(t)]) r_V V(t - \tau_V) S(t - \tau_V) \\
\dot{I}_{VP}(t) &= (1 - \exp(r_P [\mathcal{F}_1(t) - \mathcal{F}_2(t)])) r_V V(t - \tau_V) S(t - \tau_V) \\
\dot{I}_{\bar{F}}(t) &= r_V V(t) S(t) - r_V V(t - \tau_F) S(t - \tau_F) \\
\dot{I}_F(t) &= r_V V(t - \tau_F) S(t - \tau_F) \\
\dot{P}(t) &= r_F F(t) S(t) + p_P P(t) \\
\dot{F}(t) &= v_F I_F(t) - d_F F(t) \\
\dot{\mathcal{F}}_1(t) &= F(t - \tau_V) \\
\dot{\mathcal{F}}_2(t) &= F(t - (\tau_V - \tau_P)) \\
\dot{V}(t) &= v_P I_{V\bar{P}}(t) - d_V V(t).
\end{aligned} \quad (3.34)$$

### 3. Viral fitness is mainly controlled by the effect of IFN on already infected cells

Model parameter	Value	
<b>Virus dynamics</b>		
Virus production rate (wt)	$v_P$	0.54 v.u./h/cells
Virus production rate (mutant)	$v_{P\text{mut}}$	0.27 v.u./h/cells
<b>IFN dynamics</b>		
Time window of IFN permissiveness	$\tau_P$	8 h
Rate of IFN-induced inhibition of virus production	$r_P$	1.5 vol./pg/h

**Table 3.3.:** Additional parameters of the full population-based model. The extended model (3.34) is simulated with the given additional parameter values and the DENV-wt parameter estimates listed in Table 3.1 as well as the established DENV-E217A mutant specific parameter set shown in Table 3.2. Abbreviations: DENV-E217A mutant (mut), DENV-wt (wt), hours (h), picogram (pg), virus units (v.u.), volume (vol.).

The associated initial value problem of the extended model is defined by the DDE system (3.34) for time  $t \geq 0$ . At the starting time  $t_0 = 0$ , only the number of susceptible cells  $S(0) = S_0$  and the extracellular viral load  $V(0) = V_0$  are unequal to zero. For those variables, which have retarded arguments, we use as history functions the constant zero function and consider  $S(t) = 0$ ,  $V(t) = 0$  as well as  $F(t) = 0$  for  $t < 0$ .

The full delay-differential equation model (3.34) is numerically solved by applying the RADAR5 solver written in ANSI Fortran-90 (Guglielmi and Hairer (2005)). To obtain a precise solution, we implemented within the RADAR5 framework the time depending standard Jacobian matrix  $\mathcal{J}_{\text{full}}(t)$  and the Jacobian matrix with respect to the retarded variables  $\mathcal{J}_{\text{full},\tau}(t)$ . Both Jacobian matrices are given in appendix A.2.

The results of the IFN-stimulation experiment depicted in Figure 3.5 indicate an IFN permissive time window of approximately 6 h post infection with DENV-wt at a MOI of 10. The infection with such a high viral dose causes a synchronized infection of the entire cell population. Since the mean latency of virus replication after a not synchronized infection is expected to be delayed, we simulate low dose infections with a time window of IFN permissiveness of  $\tau_P = 8$  h. Additionally, we fix the rate of IFN-induced inhibition of virus production  $r_P = 10^4 r_F$ , as we suspect that restriction of virus replication is achieved faster than antiviral protection.

According to findings from the literature, IFIT1 is one of those ISGs which can be induced directly after viral recognition in an IFN-independent manner (Grandvaux et al. (2002), Diamond and Farzan (2013)). An early IFN-independent IFIT1 induction could thus also be contributing to the predicted decreased virus production of the IFIT1 reporter cells after DENV-E217A mutant infection. To incorporate IFN-independent antiviral effects in the model, we assume that virus producing cells release new infectious virus particles with the rate  $v_{P\text{mut}} = 0.5 v_V$  post infection with DENV-E217A mutant, which represents the half of the virus production rate  $v_P = v_V$  after infection with DENV-wt.

The simulation of the model (3.34) with the mentioned modifications listed in Table

### 3.5. Modeling predicts strong limitation of viral spread by the autocrine effect of IFN

3.3 shows that the simulated dynamics match the observed kinetics of both DENV-wt and DENV-E217A mutant infections as good as the original model (3.11) (see appendix A.3).

In summary, the full model allows to study the competition between spreading DENV and the antiviral immune response induced in an autocrine as well as paracrine manner by secreted IFN. Therefore we will utilize the model (3.34) in the following section 3.5 to analyze the relative importance of decreased virus production and accelerated IFN expression triggered through DENV-E217A mutant by taking into account the antiviral effect of IFN on infected and/or susceptible cells.

### 3.5. Quantitative modeling predicts strong limitation of viral spread by the antiviral effect of IFN on infected cells

The population-based model implies two distinct waves of virus replication after DENV-wt infection. While the first wave illustrates virus replication caused through the initial infection, the second wave, starting at  $\sim 60$  h post infection, is most likely due to spreading wild-type DENV released from primary infected cells (cf. Figure 3.18). In contrast to DENV-wt, virus replication resulting from secondary infection events of propagating DENV-E217A mutant is considerably weaker (cf. Figure 3.21).

The quantitative model explains the attenuated spread of the DENV-E217A mutant on the one hand by a reduced virus production, and on the other hand by a faster IFN induction (cf. Figure 3.22). To examine the individual impact of these two factors on viral spread, we simulate the outcome of DENV-wt infections for varying mutant-specific parameter values by taking into account the following three model variations (M1)-(M3) (Figure 3.25):

- (M1) The full model (3.34), which enables the simulation of the interaction between spreading DENV and the antiviral immune defense induced in an autocrine and paracrine way by released IFN (cf. Figure 3.25, left column).
- (M2) A variation of the model to consider only the antiviral effect of autocrine IFN acting on DENV infected cells. This model is simulated with the full model (3.34) by setting the protection rate  $r_F$  to zero (cf. Figure 3.25, middle column).
- (M3) The original model (3.11), that only regards the antiviral effect of paracrine IFN protecting susceptible cells against DENV infection (cf. Figure 3.25, right column).

After the simulation of all mentioned combinations, we compare the relative change of the population structure consisting of susceptible, virus replicating and protected cells as well as the different amount of IFN and virus (cf. rows in Figure 3.25). For easier comparison, the color diagrams are scaled to the results of the full model simulated with the determined DENV-wt parameter values (cf. Table 3.1 and 3.3), so that these reference results have always value zero (cf. Figure 3.25, green color).

3. Viral fitness is mainly controlled by the effect of IFN on already infected cells

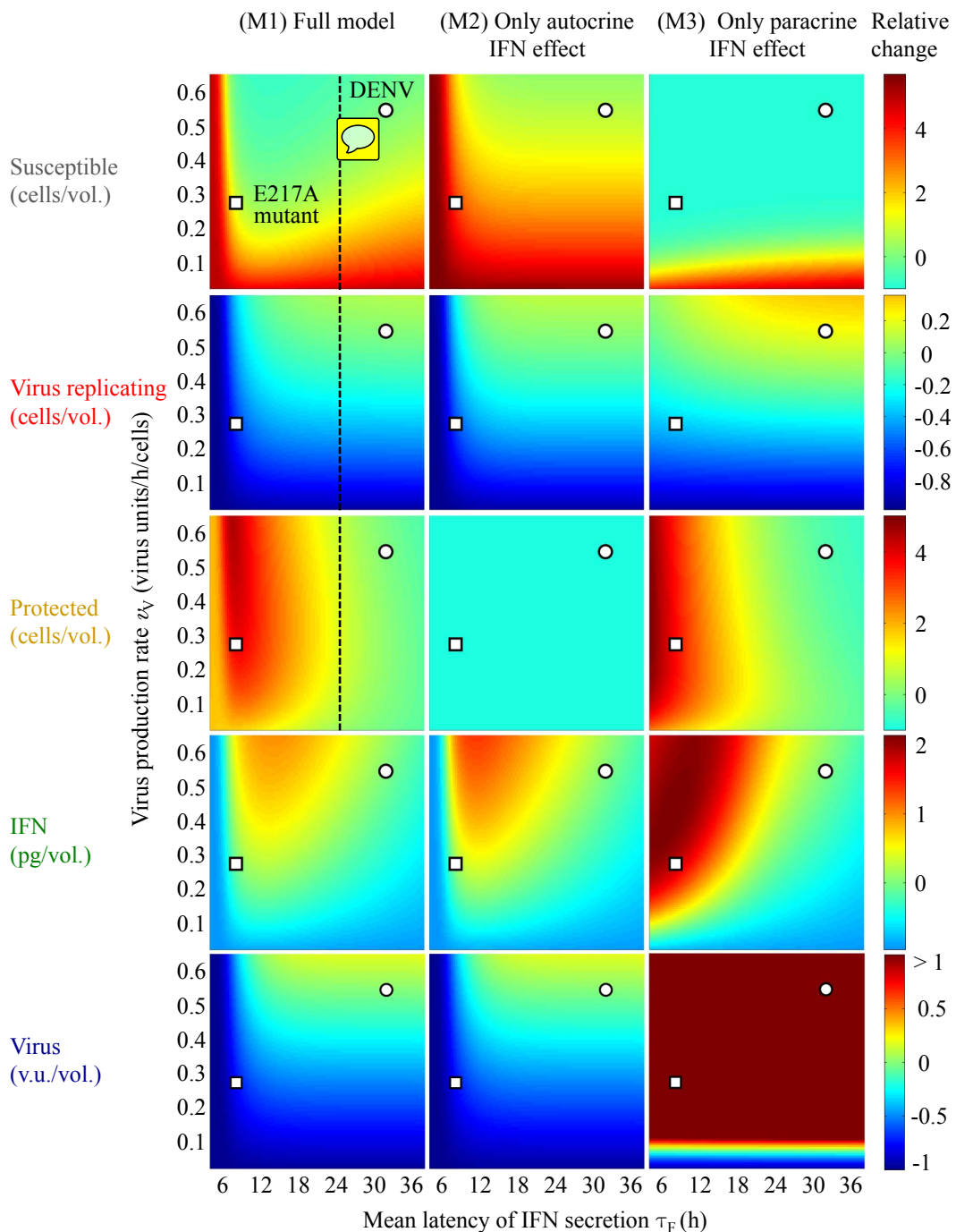


**Figure 3.25.:** Quantitative modeling predicts strong restriction of viral spread by the autocrine effect of IFN on infected cells. DENV-wt infections are simulated with varying parameter values for the mean latency of IFN secretion  $\tau_F$  (x-axis) and virus production rate  $v_V$  (y-axis) by using the three model variations (M1)-(M3) listed on page 77. Shown is the relative change of susceptible, virus replicating and protected cells as well as extracellular IFN and virus at 96 h post infection (arranged in rows). The relative values are obtained by scaling to the results of the full model simulated with the determined DENV-wt parameter values (white circles), so that these reference results have always value zero (green color). Values below or above the respective reference value are plotted in cool or warm colors, respectively. For the purpose of comparison, the results of the full model simulated with the DENV-E217A mutant parameter estimates are denoted through the white squares.

### 3.5. Modeling predicts strong limitation of viral spread by the autocrine effect of IFN

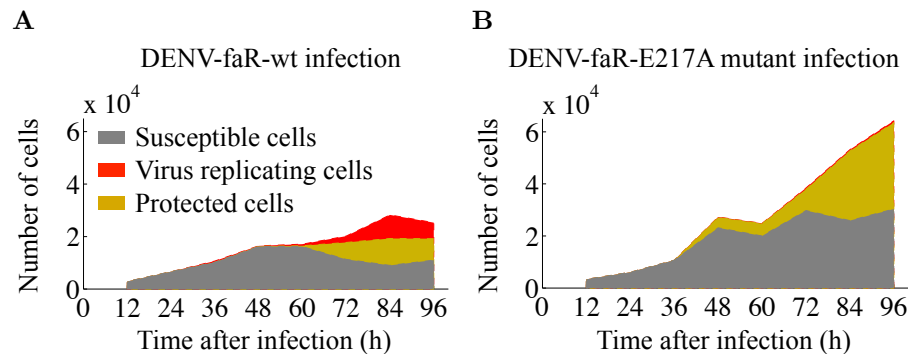


**Figure 3.26.:** A large proportion of the cell population remains susceptible after infection with DENV-wt or DENV-E217A mutant. (A, B) A549 IFIT1-deGFP reporter cells were infected with DENV-faR-wt (A) or DENV-faR-E217A mutant (B) at a MOI of 0.1. At the indicated time points post infection, cells were fixed and  $100 \mu\text{l}$  of the cell suspension was subjected to flow cytometry. The area plots represent the distribution of the observed population structure consisting of susceptible IFIT1-deGFP - DENV-faR double-negative (gray color), virus replicating DENV-faR positive (red color) and protected IFIT1-deGFP $^{+}$  - DENV-faR $^{-}$  cells (yellow color). Shown is the first of two independent experiments after infection with DENV-wt or DENV-E217A mutant replotted from Figure 3.21. (Experiments by Bianca Schmid and Ralf Bartenschlager)

The simulations of the full model (M1) with varying mutant-specific parameter values show, that both the mean latency of IFN secretion  $\tau_F$  and the virus production rate  $v_V$  can independently control the fraction of susceptible as well as virus replicating cells and, consequently, the spread of IFN and virus. Moreover, the relative change of the protected cells implies the existence of a time limit for the mean latency of IFN secretion of  $\sim 24$  h (cf. left column in Figure 3.25, dashed vertical line) after which the population is separated in susceptible and infected cells in dependency of the virus production rate.

The control function of the mutant-specific parameters with respect to the susceptible cells, virus replicating cells, secreted IFN and extracellular virus still remains intact if a solely autocrine effect of IFN is simulated with the model variant (M2). It is particularly notable that the simulations of the model (M2) concerning the number of virus replicating cells and the amount of produced virus look practically identical to the full model.

In contrast to the models (M1) and (M2), the influence of IFN on viral spread largely disappears if IFN has only a paracrine effect. Moreover, the simulations of the model (M3) regarding the amount of extracellular virus illustrate a very high virus production, that by far exceeds the virus concentration in the models with autocrine effect of IFN.

According to this model analysis, the spread of the DENV-E217A mutant is mainly restricted through an autocrine effect of IFN on infected cells which causes a decreased virus production. Remarkably, an increased paracrine effect due to accelerated IFN secretion is predicted to have very little effect on viral spread.

The distribution of the measured population structure after infection with DENV-

### 3. Viral fitness is mainly controlled by the effect of IFN on already infected cells

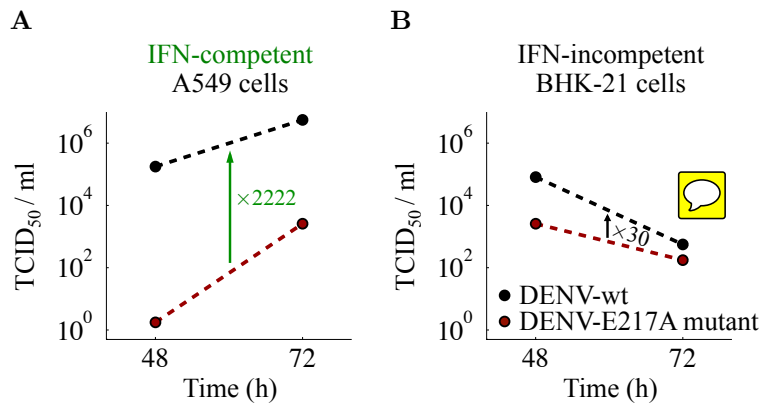


**Figure 3.27.:** The virus production of the DENV-E217A mutant is reduced through the action of autocrine IFN. (A, B) IFN-competent A549 cells (A) and IFN-incompetent BHK-21 cells (B) were electroporated with the RNA genome of DENV-faR-wt (black color) or DENV-faR-E217A mutant (dark red color). Infectious virus release was determined by TCID<sub>50</sub> assay at 48 h and 72 h post electroporation. Arrows and numbers refer to fold difference of virus titers monitored on average in the supernatant of the cell cultures. (Experiments by Bianca Schmid and Ralf Bartenschlager)

faR-wt or DENV-faR-E217A mutant illustrates the persistence of a large fraction of susceptible cells throughout the entire 4-day time course (cf. Figure 3.26). The number of naïve cells remained even larger in the DENV-E217A mutant infected cell population, although IFN is faster induced post DENV-E217A mutant infection. This observation confirms the modeling prediction, that viral spread is primarily limited by decreased virus production, rather than by the effect of IFN to protect as many cells as possible.

To further examine the ability of autocrine acting IFN to reduce virus production, we electroporated IFN-competent A549 cells and IFN-incompetent BHK-21 cells with DENV-faR-wt or DENV-faR-E217A mutant RNA (Figure 3.27). In the IFN-competent A549 cell culture, we detected a strong decrease of infectious particle release after electroporation with DENV-faR-E217A mutant compared to DENV-faR-wt. Hardly any difference between the two types of virus reporter constructs could be found in the electroporated IFN-incompetent BHK-21 cells. The lacking attenuation of DENV-E217A mutant production in an IFN-incompetent cell line corroborates the modeling prediction, that the autocrine effect of IFN on infected cells limits viral spread.

Taken together, our study of the competition between spreading DENV and the antiviral IFN response by means of mathematical modeling and experimental validation demonstrates that the fitness of the DENV-E217A mutant is attenuated due to an early IFN effect on already infected cells, which in turn curbs virus production. Since we also consider an IFN-independent inhibition of virus production in the full model (cf. section 3.4 page 76), the reduction in virus production appears to have both an IFN-independent component and an IFN-dependent component. However, the virus production rate is the key parameter for the limitation of viral spread, while a faster IFN-induced protection of naïve cells has only a minor effect against spreading DENV.

## 4. Discussion

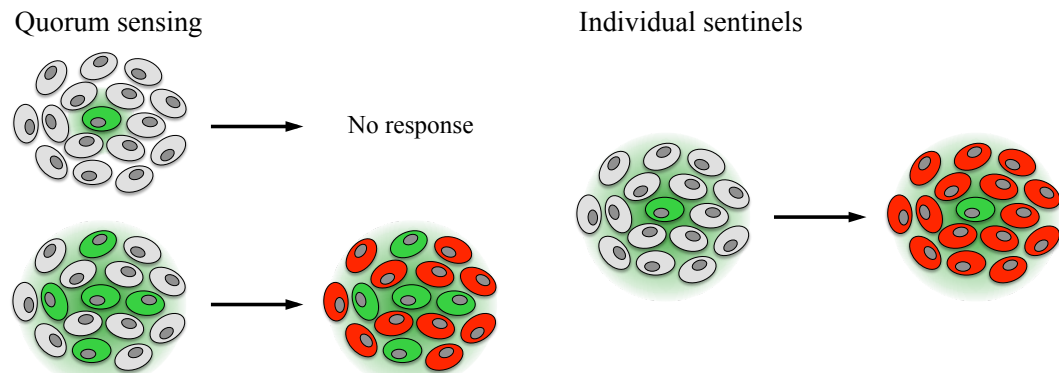


**Figure 4.1.:** IFN expressing cells act as sentinels of viral infection.



# A. Appendix

## A.1. Jacobian matrices of the delay-differential equation model

The population-based delay-differential equation model (3.11) is numerically solved by using the RADAR5 solver written in ANSI Fortran-90 (Guglielmi and Hairer (2005)). To ensure a high accuracy of the solution, we implemented within the RADAR5 framework the following sparse standard Jacobian matrix  $\mathcal{J}(t)$  and the Jacobian matrix with respect to the retarded variables  $\mathcal{J}_\tau(t)$  for time  $t \in \mathbb{R}$ :

$$\mathcal{J}(t) = \begin{pmatrix} -r_V V(t) - r_F F(t) + p_S & 0 & 0 & 0 & 0 & 0 & 0 & -r_F S(t) & -r_V S(t) \\ r_V V(t) & 0 & 0 & 0 & 0 & 0 & 0 & 0 & r_V S(t) \\ 0 & 0 & 0 & 0 & 0 & 0 & 0 & 0 & 0 \\ r_V V(t) & 0 & 0 & 0 & 0 & 0 & 0 & 0 & r_V S(t) \\ 0 & 0 & 0 & 0 & 0 & 0 & 0 & 0 & 0 \\ r_V V(t) & 0 & 0 & 0 & 0 & 0 & 0 & 0 & r_V S(t) \\ 0 & 0 & 0 & 0 & 0 & 0 & 0 & 0 & 0 \\ r_F F(t) & 0 & 0 & 0 & 0 & 0 & p_P & r_F S(t) & 0 \\ 0 & 0 & 0 & 0 & 0 & v_F & 0 & -d_F & 0 \\ 0 & 0 & 0 & v_V & 0 & 0 & 0 & 0 & -d_V \end{pmatrix}$$

$$\mathcal{J}_\tau(t) = \begin{pmatrix} 0 & 0 & 0 & 0 & 0 & 0 & 0 & 0 & 0 \\ -r_V V(t - \tau_R) & 0 & 0 & 0 & 0 & 0 & 0 & 0 & -r_V S(t - \tau_R) \\ r_V V(t - \tau_R) & 0 & 0 & 0 & 0 & 0 & 0 & 0 & r_V S(t - \tau_R) \\ -r_V V(t - \tau_V) & 0 & 0 & 0 & 0 & 0 & 0 & 0 & -r_V S(t - \tau_V) \\ r_V V(t - \tau_V) & 0 & 0 & 0 & 0 & 0 & 0 & 0 & r_V S(t - \tau_V) \\ -r_V V(t - \tau_F) & 0 & 0 & 0 & 0 & 0 & 0 & 0 & -r_V S(t - \tau_F) \\ r_V V(t - \tau_F) & 0 & 0 & 0 & 0 & 0 & 0 & 0 & r_V S(t - \tau_F) \\ 0 & 0 & 0 & 0 & 0 & 0 & 0 & 0 & 0 \\ 0 & 0 & 0 & 0 & 0 & 0 & 0 & 0 & 0 \\ 0 & 0 & 0 & 0 & 0 & 0 & 0 & 0 & 0 \end{pmatrix}.$$

## A. Appendix

### A.2. Jacobian matrices of the full delay-differential equation model

A numerical solution of the full population-based delay-differential equation model (3.34) is obtained by utilizing the RADAR5 solver written in ANSI Fortran-90 (Guglielmi and Hairer (2005)). For an increased accuracy of the solution, we provided within the RADAR5 framework the following sparse standard Jacobian matrix  $\mathcal{J}_{\text{full}}(t)$  and the Jacobian matrix with respect to the retarded variables  $\mathcal{J}_{\text{full},\tau}(t)$  for time  $t \in \mathbb{R}$ :

$$\mathcal{J}_{\text{full}}(t) = \begin{pmatrix} j_1 & 0 & 0 & 0 & 0 & 0 & 0 & 0 & -r_F S(t) & 0 & 0 & -r_V S(t) \\ r_V V(t) & 0 & 0 & 0 & 0 & 0 & 0 & 0 & 0 & 0 & 0 & r_V S(t) \\ 0 & 0 & 0 & 0 & 0 & 0 & 0 & 0 & 0 & 0 & 0 & 0 \\ r_V V(t) & 0 & 0 & 0 & 0 & 0 & 0 & 0 & 0 & 0 & 0 & r_V S(t) \\ 0 & 0 & 0 & 0 & 0 & 0 & 0 & 0 & 0 & j_{\mathcal{F}} & -j_{\mathcal{F}} & 0 \\ 0 & 0 & 0 & 0 & 0 & 0 & 0 & 0 & 0 & -j_{\mathcal{F}} & j_{\mathcal{F}} & 0 \\ r_V V(t) & 0 & 0 & 0 & 0 & 0 & 0 & 0 & 0 & 0 & 0 & r_V S(t) \\ 0 & 0 & 0 & 0 & 0 & 0 & 0 & 0 & 0 & 0 & 0 & 0 \\ r_F F(t) & 0 & 0 & 0 & 0 & 0 & 0 & p_P & r_F S(t) & 0 & 0 & 0 \\ 0 & 0 & 0 & 0 & 0 & 0 & v_F & 0 & -d_F & 0 & 0 & 0 \\ 0 & 0 & 0 & 0 & 0 & 0 & 0 & 0 & 0 & 0 & 0 & 0 \\ 0 & 0 & 0 & 0 & 0 & 0 & 0 & 0 & 0 & 0 & 0 & 0 \\ 0 & 0 & 0 & 0 & v_P & 0 & 0 & 0 & 0 & 0 & 0 & -d_V \end{pmatrix}$$

$$\mathcal{J}_{\text{full},\tau}(t) = \begin{pmatrix} 0 & 0 & 0 & 0 & 0 & 0 & 0 & 0 & 0 & 0 & 0 & 0 \\ -r_V V(t - \tau_R) & 0 & 0 & 0 & 0 & 0 & 0 & 0 & 0 & 0 & 0 & -r_V S(t - \tau_R) \\ r_V V(t - \tau_R) & 0 & 0 & 0 & 0 & 0 & 0 & 0 & 0 & 0 & 0 & r_V S(t - \tau_R) \\ -r_V V(t - \tau_V) & 0 & 0 & 0 & 0 & 0 & 0 & 0 & 0 & 0 & 0 & -r_V S(t - \tau_V) \\ j_{\tau,(5,1)} & 0 & 0 & 0 & 0 & 0 & 0 & 0 & 0 & 0 & 0 & j_{\tau,(5,13)} \\ j_{\tau,(6,1)} & 0 & 0 & 0 & 0 & 0 & 0 & 0 & 0 & 0 & 0 & j_{\tau,(6,13)} \\ -r_V V(t - \tau_F) & 0 & 0 & 0 & 0 & 0 & 0 & 0 & 0 & 0 & 0 & -r_V S(t - \tau_F) \\ r_V V(t - \tau_F) & 0 & 0 & 0 & 0 & 0 & 0 & 0 & 0 & 0 & 0 & r_V S(t - \tau_F) \\ 0 & 0 & 0 & 0 & 0 & 0 & 0 & 0 & 0 & 0 & 0 & 0 \\ 0 & 0 & 0 & 0 & 0 & 0 & 0 & 0 & 0 & 0 & 0 & 0 \\ 0 & 0 & 0 & 0 & 0 & 0 & 0 & 0 & 1 & 0 & 0 & 0 \\ 0 & 0 & 0 & 0 & 0 & 0 & 0 & 0 & 1 & 0 & 0 & 0 \\ 0 & 0 & 0 & 0 & 0 & 0 & 0 & 0 & 0 & 0 & 0 & 0 \end{pmatrix}$$

with

$$\begin{aligned} j_1 &= -r_V V(t) - r_F F(t) + p_S \\ j_{\mathcal{F}} &= r_P \exp(r_P [\mathcal{F}_1(t) - \mathcal{F}_2(t)]) r_V V(t - \tau_V) S(t - \tau_V) \\ j_{\tau,(5,1)} &= \exp(r_P [\mathcal{F}_1(t) - \mathcal{F}_2(t)]) r_V V(t - \tau_V) \\ j_{\tau,(5,13)} &= \exp(r_P [\mathcal{F}_1(t) - \mathcal{F}_2(t)]) r_V S(t - \tau_V) \\ j_{\tau,(6,1)} &= (1 - \exp(r_P [\mathcal{F}_1(t) - \mathcal{F}_2(t)])) r_V V(t - \tau_V) \\ j_{\tau,(6,13)} &= (1 - \exp(r_P [\mathcal{F}_1(t) - \mathcal{F}_2(t)])) r_V S(t - \tau_V). \end{aligned}$$

**A.3. The full model reproduces the observed dynamics  
of both DENV-wt and DENV-E217A mutant  
infections**



# Bibliography

- Eliana G Acosta, Anil Kumar, and Ralf Bartenschlager. Revisiting dengue virus-host cell interaction: new insights into molecular and cellular virology. *Advances in virus research*, 88:1–109, 2014.
- Uri Alon. *An introduction to systems biology: design principles of biological circuits*. CRC press, 2006.
- Effie Apostolou and Dimitris Thanos. Virus Infection Induces NF- $\kappa$ B-Dependent Interchromosomal Associations Mediating Monoallelic IFN- $\beta$  Gene Expression. *Cell*, 134(1):85–96, 2008.
- Joseph Ashour, Maudry Laurent-Rolle, Pei-Yong Shi, and Adolfo García-Sastre. NS5 of dengue virus mediates STAT2 binding and degradation. *Journal of virology*, 83(11):5408–5418, 2009.
- Christopher TH Baker, Gennadii A Bocharov, and Fathalla A Rihan. *A report on the use of delay differential equations in numerical modelling in the biosciences*. Citeseer, 1999.
- Steve Baker and Robert D Cousins. Clarification of the use of chi-square and likelihood functions in fits to histograms. *Nuclear Instruments and Methods in Physics Research*, 221(2):437–442, 1984.
- Sudip K Bandyopadhyay, George T Leonard, Tanya Bandyopadhyay, George R Stark, and Ganes C Sen. Transcriptional induction by double-stranded RNA is mediated by interferon-stimulated response elements without activation of interferon-stimulated gene factor 3. *Journal of Biological Chemistry*, 270(33):19624–19629, 1995.
- Harvey Thomas Banks, Anna Broido, Brandi Canter, Kaitlyn Gayvert, Shuhua Hu, Michele Joyner, and Kathryn Link. Simulation Algorithms for Continuous Time Markov Chain Models. 2011.
- Maria Vittoria Barbarossa. *On a class of neutral equations with state-dependent delay in population dynamics*. PhD thesis, Mu nchen, Technische Universita t Mu nchen, Diss., 2013, 2013.
- Ralf Bartenschlager and Sven Miller. Molecular aspects of Dengue virus replication. 2008.
- Oliver Bauhofer, Alessia Ruggieri, Bianca Schmid, Peter Schirmacher, and Ralf Bartenschlager. Persistence of HCV in quiescent hepatic cells under conditions of an interferon-induced antiviral response. *Gastroenterology*, 143(2):429–438, 2012.

## Bibliography

- G Bocharov and KP Hadeler. Structured population models, conservation laws, and delay equations. *Journal of Differential Equations*, 168(1):212–237, 2000.
- Gennadii A Bocharov and Fathalla A Rihan. Numerical modelling in biosciences using delay differential equations. *Journal of Computational and Applied Mathematics*, 125(1):183–199, 2000.
- Przemyslaw Bogacki and Lawrence F Shampine. A 3 (2) pair of Runge-Kutta formulas. *Applied Mathematics Letters*, 2(4):321–325, 1989.
- Kiva Brennan and Andrew G Bowie. Activation of host pattern recognition receptors by viruses. *Current opinion in microbiology*, 13(4):503–507, 2010.
- Yang Cao and David C Samuels. Discrete stochastic simulation methods for chemically reacting systems. *Methods in enzymology*, 454:115–140, 2009.
- I Capua and DJ Alexander. Human health implications of avian influenza viruses and paramyxoviruses. *European Journal of Clinical Microbiology and Infectious Diseases*, 23(1):1–6, 2004.
- TJ Chambers and CM Rice. Molecular biology of the flaviviruses. *Microbiological sciences*, 4(7):219–223, 1987.
- Tsung-Hsien Chang, Ching-Len Liao, and Yi-Ling Lin. Flavivirus induces interferon-beta gene expression through a pathway involving RIG-I-dependent IRF-3 and PI3K-dependent NF- $\kappa$ B activation. *Microbes and infection*, 8(1):157–171, 2006.
- Won-Suk Chang, Hao Shang, Rushika M Perera, Shee-mei Lok, Dagmar Sedlak, Richard J Kuhn, and Gil U Lee. Rapid detection of dengue virus in serum using magnetic separation and fluorescence detection. *Analyst*, 133(2):233–240, 2008.
- Brian Charlesworth. *Evolution in age-structured populations*, volume 1. Cambridge University Press Cambridge, 1980.
- S Chen, JAL Short, DF Young, MJ Killip, M Schneider, S Goodbourn, and RE Randall. Heterocellular induction of interferon by negative-sense RNA viruses. *Virology*, 407(2):247–255, 2010.
- Kay Childs, Nicola Stock, Craig Ross, Jelena Andrejeva, Louise Hilton, Michael Skinner, Richard Randall, and Stephen Goodbourn. mda-5, but not RIG-I, is a common target for paramyxovirus V proteins. *Virology*, 359(1):190–200, 2007.
- T Coleman and Y Zhang. Optimization Toolbox For Use with MATLAB. Natick (MA): The MathWorks. Inc., Sep, 2003.
- David Roxbee Cox and David Oakes. *Analysis of survival data*, volume 21. CRC Press, 1984.
- Stephane Daffis, Kristy J Szretter, Jill Schriewer, Jianqing Li, Soonjeon Youn, John Errett, Tsai-Yu Lin, Stewart Schneller, Roland Zust, Hongping Dong, et al. 2 [prime]-O methylation of the viral mRNA cap evades host restriction by IFIT family members. *Nature*, 468(7322):452–456, 2010.

## Bibliography

- Michael S Diamond and Michael Farzan. The broad-spectrum antiviral functions of IFIT and IFITM proteins. *Nature Reviews Immunology*, 13(1):46–57, 2013.
- Michael S Diamond, T Guy Roberts, Dianna Edgil, Betty Lu, Joel Ernst, and Eva Harris. Modulation of dengue virus infection in human cells by alpha, beta, and gamma interferons. *Journal of Virology*, 74(11):4957–4966, 2000.
- Annette J Dobson. *An introduction to generalized linear models*. CRC press, 2001.
- Hongping Dong, Katja Fink, Roland Züst, Siew Pheng Lim, Cheng-Feng Qin, and Pei-Yong Shi. Flavivirus RNA methylation. *Journal of General Virology*, 95(Pt 4):763–778, 2014.
- Marie-Pierre Egloff, Delphine Benarroch, Barbara Selisko, Jean-Louis Romette, and Bruno Canard. An RNA cap (nucleoside-2'-O)-methyltransferase in the flavivirus RNA polymerase NS5: crystal structure and functional characterization. *The EMBO journal*, 21(11):2757–2768, 2002.
- Emory L Ellis and Max Delbrück. The growth of bacteriophage. *The Journal of general physiology*, 22(3):365–384, 1939.
- Michael B Elowitz, Arnold J Levine, Eric D Siggia, and Peter S Swain. Stochastic gene expression in a single cell. *Science*, 297(5584):1183–1186, 2002.
- Katja Fink and Pei-Yong Shi. Live attenuated vaccine: the first clinically approved dengue vaccine? *Expert review of vaccines*, 13(2):185–188, 2014.
- Wolfgang Fischl and Ralf Bartenschlager. High-Throughput Screening Using Dengue Virus Reporter Genomes. In *Antiviral Methods and Protocols*, pages 205–219. Springer, 2013.
- Ethan Ford and Dimitris Thanos. The transcriptional code of human IFN- $\beta$  gene expression. *Biochimica et Biophysica Acta (BBA)-Gene Regulatory Mechanisms*, 1799(3):328–336, 2010.
- Ph Getto, M Kimmel, and A Marciniak-Czochra. Modelling and analysis of dynamics of viral infection of cells and of interferon resistance. *Journal of Mathematical Analysis and Applications*, 344(2):821–850, 2008.
- Daniel T Gillespie. A general method for numerically simulating the stochastic time evolution of coupled chemical reactions. *Journal of computational physics*, 22(4):403–434, 1976.
- Daniel T Gillespie. Exact stochastic simulation of coupled chemical reactions. *The journal of physical chemistry*, 81(25):2340–2361, 1977.
- Daniel T Gillespie. Stochastic simulation of chemical kinetics. *Annu. Rev. Phys. Chem.*, 58:35–55, 2007.
- Yunhao Gong, Rachel Trowbridge, Thomas B Macnaughton, Edwin G Westaway, Anthony D Shannon, and Eric J Gowans. Characterization of RNA synthesis during a one-step growth curve and of the replication mechanism of bovine viral diarrhoea virus. *Journal of General Virology*, 77(11):2729–2736, 1996.

## Bibliography

- Orland R Gonzalez, Christoph Küper, Kirsten Jung, Prospero C Naval, and Eduardo Mendoza. Parameter estimation using Simulated Annealing for S-system models of biochemical networks. *Bioinformatics*, 23(4):480–486, 2007.
- Nathalie Grandvaux, Marc J Servant, Ganes C Sen, Siddarth Balachandran, Glen N Barber, Rongtuan Lin, John Hiscott, et al. Transcriptional profiling of interferon regulatory factor 3 target genes: direct involvement in the regulation of interferon-stimulated genes. *Journal of virology*, 76(11):5532–5539, 2002.
- N Guglielmi and E Hairer. Users' guide for the code RADAR5-version 2.1. Technical report, Università dell' Aquila, Italy, 2005.
- Nicola Guglielmi. On the Newton iteration in the application of collocation methods to implicit delay equations. *Applied numerical mathematics*, 53(2):281–297, 2005.
- Nicola Guglielmi and Ernst Hairer. Implementing Radau IIA methods for stiff delay differential equations. *Computing*, 67(1):1–12, 2001.
- Nicola Guglielmi and Ernst Hairer. Computing breaking points in implicit delay differential equations. *Advances in Computational Mathematics*, 29(3):229–247, 2008.
- Piotr Gwiazda, Jędrzej Jabłonski, Anna Marciniak-Czochra, and Agnieszka Ulikowska. Analysis of particle methods for structured population models with nonlocal boundary term in the framework of bounded Lipschitz distance. *Numerical Methods for Partial Differential Equations*, 2014.
- Matthias Habjan, Philipp Hubel, Livia Lacerda, Christian Benda, Cathleen Holze, Christian H Eberl, Angelika Mann, Eveline Kindler, Cristina Gil-Cruz, John Ziebuhr, et al. Sequestration by IFIT1 impairs translation of 2 O-unmethylated capped RNA. *PLoS pathogens*, 9(10):e1003663, 2013.
- Ernst Hairer and Gerhard Wanner. Stiff differential equations solved by Radau methods. *Journal of Computational and Applied Mathematics*, 111(1):93–111, 1999.
- JC Hierholzer, RA Killington, BW Mahy, and HO Kangro. Virology methods manual. *Eds. BWJ Mahy and HO Kangro. London*, 1996.
- Kenya Honda, Hideyuki Yanai, Hideo Negishi, Masataka Asagiri, Mitsuharu Sato, Tatsuaki Mizutani, Naoya Shimada, Yusuke Ohba, Akinori Takaoka, Nobuaki Yoshida, et al. IRF-7 is the master regulator of type-I interferon-dependent immune responses. *Nature*, 434(7034):772–777, 2005.
- Jianzhong Hu, Stuart C Sealfon, Fernand Hayot, Ciriyam Jayaprakash, Madhu Kumar, Audrey C Pendleton, Arnaud Ganee, Ana Fernandez-Sesma, Thomas M Moran, and James G Wetmur. Chromosome-specific and noisy IFNB1 transcription in individual virus-infected human primary dendritic cells. *Nucleic acids research*, 35(15):5232–5241, 2007.
- Jianzhong Hu, German Nudelman, Yishai Shimon, Madhu Kumar, Yaomei Ding, Carolina López, Fernand Hayot, James G Wetmur, and Stuart C Sealfon. Role of

## Bibliography

- cell-to-cell variability in activating a positive feedback antiviral response in human dendritic cells. *PLoS one*, 6(2):e16614, 2011.
- Meleri Jones, Andrew Davidson, Linda Hibbert, Petra Gruenwald, Joerg Schlaak, Simon Ball, Graham R Foster, and Michael Jacobs. Dengue virus inhibits alpha interferon signaling by reducing STAT2 expression. *Journal of virology*, 79(9):5414–5420, 2005.
- Mads Kærn, Timothy C Elston, William J Blake, and James J Collins. Stochasticity in gene expression: from theories to phenotypes. *Nature Reviews Genetics*, 6(6):451–464, 2005.
- Hiroki Kato, Shintaro Sato, Mitsutoshi Yoneyama, Masahiro Yamamoto, Satoshi Uematsu, Kosuke Matsui, Tohru Tsujimura, Kiyoshi Takeda, Takashi Fujita, Osamu Takeuchi, et al. Cell type-specific involvement of RIG-I in antiviral response. *Immunity*, 23(1):19–28, 2005.
- David G Kendall. Stochastic processes and population growth. *Journal of the Royal Statistical Society. Series B (Methodological)*, 11(2):230–282, 1949.
- MJ Killip, DF Young, CS Ross, S Chen, S Goodbourn, and RE Randall. Failure to activate the IFN- $\beta$  promoter by a paramyxovirus lacking an interferon antagonist. *Virology*, 415(1):39–46, 2011.
- Taishi Kimura, Hiroshi Katoh, Hisako Kayama, Hiroyuki Saiga, Megumi Okuyama, Toru Okamoto, Eiji Umemoto, Yoshiharu Matsuura, Masahiro Yamamoto, and Kiyoshi Takeda. Ifit1 Inhibits Japanese encephalitis virus replication through binding to 5 capped 2'-O unmethylated RNA. *Journal of virology*, 87(18):9997–10003, 2013.
- K Königsberger. Analysis 1 (6., durchges. Aufl.) (German Edition). Springer, 2004.
- Leo E Kreuz and Allan H Levy. Physical properties of chick interferon. *Journal of bacteriology*, 89(2):462–469, 1965.
- Yutaro Kumagai, Himanshu Kumar, Shohei Koyama, Taro Kawai, Osamu Takeuchi, and Shizuo Akira. Cutting Edge: TLR-Dependent viral recognition along with type I IFN positive feedback signaling masks the requirement of viral replication for IFN-alpha production in plasmacytoid dendritic cells. *J Immunol*, 182(7):3960–3964, Apr 2009.
- Anil Kumar, Sandra Bühler, Barbara Selisko, Andrew Davidson, Klaas Mulder, Bruno Canard, Sven Miller, and Ralf Bartenschlager. Nuclear localization of dengue virus nonstructural protein 5 does not strictly correlate with efficient viral RNA replication and inhibition of type I interferon signaling. *Journal of virology*, 87(8):4545–4557, 2013.
- Myriam S Kunzi and Paula M Pitha. Interferon targeted genes in host defense. *Autoimmunity*, 36(8):457–461, 2003.
- Chih-Yun Lai, Hsien-Ping Hu, Chwan-Chuen King, and Wei-Kung Wang. Incorporation of dengue virus replicon into virus-like particles by a cell line stably

## Bibliography

- expressing precursor membrane and envelope proteins of dengue virus type 2. *Journal of biomedical science*, 15(1):15–27, 2008.
- Ha Youn Lee, David J Topham, Sung Yong Park, Joseph Hollenbaugh, John Treanor, Tim R Mosmann, Xia Jin, Brian M Ward, Hongyu Miao, Jeanne Holden-Wiltse, et al. Simulation and prediction of the adaptive immune response to influenza A virus infection. *Journal of virology*, 83(14):7151–7165, 2009.
- Doron Levin, Daniel Harari, and Gideon Schreiber. Stochastic receptor expression determines cell fate upon interferon treatment. *Molecular and cellular biology*, 31(16):3252–3266, 2011.
- Kun Li, Ruben M Markosyan, Yi-Min Zheng, Ottavia Gelfetto, Brittani Bungart, Minghua Li, Shilei Ding, Yuxian He, Chen Liang, James C Lee, et al. IFITM proteins restrict viral membrane hemifusion. *PLoS pathogens*, 9(1):e1003124, 2013.
- Björn F Lillemeier, Mario Köster, and Ian M Kerr. STAT1 from the cell membrane to the DNA. *The EMBO journal*, 20(10):2508–2517, 2001.
- BD Lindenbach. H. J. Thiel, and C. M. Rice. Flaviviridae: The Viruses and Their Replication. *Fields Virology*. Lippincott Williams & Wilkins, Philadelphia, 2007.
- Brett D Lindenbach, Matthew J Evans, Andrew J Syder, Benno Wölk, Timothy L Tellinghuisen, Christopher C Liu, Toshiaki Maruyama, Richard O Hynes, Dennis R Burton, Jane A McKeating, et al. Complete replication of hepatitis C virus in cell culture. *Science*, 309(5734):623–626, 2005.
- Narendra Maheshri and Erin K O’Shea. Living with noisy genes: how cells function reliably with inherent variability in gene expression. *Annu. Rev. Biophys. Biomol. Struct.*, 36:413–434, 2007.
- Tim Maiwald, Annette Schneider, Hauke Busch, Sven Sahle, Norbert Gretz, Thomas S Weiss, Ursula Kummer, and Ursula Klingmüller. Combining theoretical analysis and experimental data generation reveals IRF9 as a crucial factor for accelerating interferon  $\alpha$ -induced early antiviral signalling. *FEBS journal*, 277(22):4741–4754, 2010.
- Luca Mariani, Edda G Schulz, Maria H Lexberg, Caroline Helmstetter, Andreas Radbruch, Max Löhnig, and Thomas Höfer. Short-term memory in gene induction reveals the regulatory principle behind stochastic IL-4 expression. *Molecular systems biology*, 6(1), 2010.
- I Matheson, DF Walls, and CW Gardiner. Stochastic models of firstorder nonequilibrium phase transitions in chemical reactions. *Journal of Statistical Physics*, 12(1):21–34, 1975.
- Michela Mazzon, Meleri Jones, Andrew Davidson, Benjamin Chain, and Michael Jacobs. Dengue virus NS5 inhibits interferon- $\alpha$  signaling by blocking signal transducer and activator of transcription 2 phosphorylation. *Journal of Infectious Diseases*, 200(8):1261–1270, 2009.
- Donald A McQuarrie. Stochastic approach to chemical kinetics. *Journal of Applied Probability*, 4(3):413–478, 1967.

## Bibliography

- Johan AJ Metz and Odo Diekmann. The dynamics of physiologically structured populations. *Lecture notes in biomathematics*, 68, 1986.
- Juliet Morrison, Maudry Laurent-Rolle, Ana M Maestre, Ricardo Rajsbaum, Giuseppe Pisanelli, Viviana Simon, Lubbertus CF Mulder, Ana Fernandez-Sesma, and Adolfo García-Sastre. Dengue virus co-opts UBR4 to degrade STAT2 and antagonize type I interferon signaling. *PLoS pathogens*, 9(3):e1003265, 2013.
- James D. Murray. *Mathematical Biology: I. An Introduction (Interdisciplinary Applied Mathematics) (Pt. 1)*. Springer, 2002.
- In Jae Myung. Tutorial on maximum likelihood estimation. *Journal of mathematical Psychology*, 47(1):90–100, 2003.
- Kazuhide Onoguchi, Koji Onomoto, Shiori Takamatsu, Michihiko Jogi, Azumi Take-mura, Shiho Morimoto, Ilkka Julkunen, Hideo Namiki, Mitsutoshi Yoneyama, and Takashi Fujita. Virus-infection or 5'ppp-RNA activates antiviral signal through redistribution of IPS-1 mediated by MFN1. *PLoS pathogens*, 6(7):e1001012, 2010.
- Kasia A Pawelek, Shengqiang Liu, Faranak Pahlevani, and Libin Rong. A model of HIV-1 infection with two time delays: mathematical analysis and comparison with patient data. *Mathematical biosciences*, 235(1):98–109, 2012.
- José Peña and Eva Harris. Early dengue virus protein synthesis induces extensive rearrangement of the endoplasmic reticulum independent of the UPR and SREBP-2 pathway. *PloS one*, 7(6):e38202, 2012.
- Andreas Pichlmair, Caroline Lassnig, Carol-Ann Eberle, Maria W Górná, Christoph L Baumann, Thomas R Burkard, Tilmann Bürcstümmer, Adrijana Stefanovic, Sigurd Krieger, Keiryn L Bennett, et al. IFIT1 is an antiviral protein that recognizes 5' [prime]-triphosphate RNA. *Nature immunology*, 12(7):624–630, 2011.
- William H. Press, Saul A. Teukolsky, William T. Vetterling, and Brian P. Flannery. *Numerical Recipes 3rd Edition: The Art of Scientific Computing*. Cambridge University Press, 2007.
- Arjun Raj and Alexander van Oudenaarden. Nature, nurture, or chance: stochastic gene expression and its consequences. *Cell*, 135(2):216–226, 2008.
- Ulfert Rand and Hansjörg Hauser. *Dynamics of Type I Interferon Induction and Action*. 2010.
- Jonathan M Raser and Erin K O’Shea. Noise in gene expression: origins, consequences, and control. *Science*, 309(5743):2010–2013, 2005.
- Debashish Ray, Aaloki Shah, Mark Tilgner, Yi Guo, Yiwei Zhao, Hongping Dong, Tia S Deas, Yangsheng Zhou, Hongmin Li, and Pei-Yong Shi. West Nile virus 5'-cap structure is formed by sequential guanine N-7 and ribose 2'-O methylations by nonstructural protein 5. *Journal of virology*, 80(17):8362–8370, 2006.

## Bibliography

- Jan Rehwinkel, Choon Ping Tan, Delphine Goubau, Oliver Schulz, Andreas Pichlmair, Katja Bier, Nicole Robb, Frank Vreede, Wendy Barclay, Ervin Fodor, et al. RIG-I detects viral genomic RNA during negative-strand RNA virus infection. *Cell*, 140(3):397–408, 2010.
- G Rodriguez. Lecture notes on generalized linear models, 2007.
- R Rott. Molecular basis of infectivity and pathogenicity of myxovirus. *Archives of virology*, 59(4):285–298, 1979.
- Anthony J Sadler and Bryan RG Williams. Interferon-inducible antiviral effectors. *Nature Reviews Immunology*, 8(7):559–568, 2008.
- Bianca Schmid. *Dynamics of Hepatitis C Virus and Dengue Virus-induced Innate Immune Responses*. PhD thesis, 2014.
- Johannes Josef Schneider and Scott Kirkpatrick. *Stochastic optimization*. Springer, 2006.
- John W Schoggins, Marcus Dorner, Michael Feulner, Naoko Imanaka, Mary Y Murphy, Alexander Ploss, and Charles M Rice. Dengue reporter viruses reveal viral dynamics in interferon receptor-deficient mice and sensitivity to interferon effectors in vitro. *Proceedings of the National Academy of Sciences*, 109(36):14610–14615, 2012.
- Larry F Shampine and Sylvester Thompson. Numerical solution of delay differential equations. In *Delay Differential Equations*, pages 1–27. Springer, 2009.
- Lawrence F Shampine and Mark W Reichelt. The matlab ode suite. *SIAM journal on scientific computing*, 18(1):1–22, 1997.
- Lawrence F Shampine and Skip Thompson. Solving ddes in matlab. *Applied Numerical Mathematics*, 37(4):441–458, 2001.
- Berend Snijder and Lucas Pelkmans. Origins of regulated cell-to-cell variability. *Nature Reviews Molecular Cell Biology*, 12(2):119–125, 2011.
- Sabrina L Spencer, Suzanne Gaudet, John G Albeck, John M Burke, and Peter K Sorger. Non-genetic origins of cell-to-cell variability in TRAIL-induced apoptosis. *Nature*, 459(7245):428–432, 2009.
- David G Spiller, Christopher D Wood, David A Rand, and Michael RH White. Measurement of single-cell dynamics. *Nature*, 465(7299):736–745, 2010.
- Peter S Swain, Michael B Elowitz, and Eric D Siggia. Intrinsic and extrinsic contributions to stochasticity in gene expression. *Proceedings of the National Academy of Sciences*, 99(20):12795–12800, 2002.
- Kristy J Szretter, Brian P Daniels, Hyelim Cho, Maria D Gainey, Wayne M Yokoyama, Michael Gale Jr, Herbert W Virgin, Robyn S Klein, Ganes C Sen, and Michael S Diamond. 2'-O methylation of the viral mRNA cap by West Nile virus evades ifit1-dependent and-independent mechanisms of host restriction in vivo. *PLoS pathogens*, 8(5):e1002698, 2012.

## Bibliography

- Osamu Takeuchi and Shizuo Akira. Innate immunity to virus infection. *Immunological reviews*, 227(1):75–86, 2009.
- Richard Taylor. Interpretation of the correlation coefficient: a basic review. *Journal of diagnostic medical sonography*, 6(1):35–39, 1990.
- Argyrios N Theofilopoulos, Roberto Baccala, Bruce Beutler, and Dwight H Kono. Type I interferons ( $\alpha/\beta$ ) in immunity and autoimmunity. *Annu. Rev. Immunol.*, 23:307–335, 2005.
- DJ Venzon and SH Moolgavkar. A method for computing profile-likelihood-based confidence intervals. *Applied Statistics*, pages 87–94, 1988.
- Uwe Vinkemeier. Getting the message across, STAT! Design principles of a molecular signaling circuit. *The Journal of cell biology*, 167(2):197–201, 2004.
- Karl-Heinz Waldmann and Ulrike M Stocker. Stochastische Modelle: Eine anwendungsorientierte Einführung, EMILeAstat, 2004.
- Sonja Welsch, Sven Miller, Ines Romero-Brey, Andreas Merz, Christopher KE Bleck, Paul Walther, Stephen D Fuller, Claude Antony, Jacomine Krijnse-Locker, and Ralf Bartenschlager. Composition and three-dimensional architecture of the dengue virus replication and assembly sites. *Cell host & microbe*, 5(4):365–375, 2009.
- Dirk Werner. *Funktionalanalysis (Springer-Lehrbuch) (German Edition)*. Springer, 2005.
- Rainer Zawatzky, Edward De Maeyer, and Jacqueline De Maeyer-Guignard. Identification of individual interferon-producing cells by in situ hybridization. *Proceedings of the National Academy of Sciences*, 82(4):1136–1140, 1985.
- Roland Züst, Luisa Cervantes-Barragan, Matthias Habjan, Reinhard Maier, Benjamin W Neuman, John Ziebuhr, Kristy J Szretter, Susan C Baker, Winfried Barchet, Michael S Diamond, et al. Ribose 2'-O-methylation provides a molecular signature for the distinction of self and non-self mRNA dependent on the RNA sensor Mda5. *Nature immunology*, 12(2):137–143, 2011.
- Roland Züst, Hongping Dong, Xiao-Feng Li, David C Chang, Bo Zhang, Thavamalar Balakrishnan, Ying-Xiu Toh, Tao Jiang, Shi-Hua Li, Yong-Qiang Deng, et al. Rational design of a live attenuated dengue vaccine: 2'-o-methyltransferase mutants are highly attenuated and immunogenic in mice and macaques. *PLoS pathogens*, 9(8):e1003521, 2013.



# Abbreviations and symbols

**1<sub>A</sub>** characteristic function of the set *A*, p. 27

$\cong$  corresponds to

$\coloneqq$  equal by definition

$\emptyset$  degradation

$\dot{f}(t) = \frac{d}{dt} f(t)$  derivative of the function *f(t)* with respect to time *t*

**A ∩ B** intersection of the sets *A* and *B*

$\mathcal{O}$  replication

$\subseteq$  subset of

$\forall$  universal quantifier; for all

$\alpha$  alpha

**A549** carcinomic human alveolar epithelial cell line, p. 40

$\beta$  beta

**BAC** bacterial artificial chromosome, p. 4

**BHK-21** baby hamster kidney cell line, p. 61

$\mathbb{C}$  set of complex numbers

**C** capsid protein of DENV, p. 38

**CDF** cumulative distribution function, p. 27, 72

**CFP** cyan fluorescent protein, p. 4

$\chi^2$  chi-squares statistic, p. 26, 32, 62

**CI** confidence interval, p. 64

**CS1** circularization sequence 1, p. 39

**CV** coefficient of variation, p. 6

## Abbreviations and symbols

- $\delta(x)$**  delta function also known as delta distribution, p. 56
- DAPI** 4',6-diamidino-2-phenylindole fluorescent stain, p. 44
- DDE** delay-differential equation, p. 55
- deGFP** destabilized version of enhanced green fluorescent protein, p. 40
- $\Delta T_{\text{gen}}$**  time difference between sister cells regarding IFN- $\beta$ -tGFP expression, p. 11
- $\Delta T_{\text{sig}}$**  time difference between sister cells regarding IRF-7 signaling, p. 11
- DENV** dengue virus, p. 37
- DF** degree of freedom, p. 28
- dsRNA** double-stranded RNA, p. 40
- $\epsilon$**  element of
- $\epsilon$**  epsilon
- E** envelope protein of DENV, p. 38
- E217A** DENV mutant, which differ from the DENV-wt due to a single substitution of the glutamic acid residue (E) by an alanine residue (A) at the amino acid position 217 of the NS5 protein, p. 51
- eGFP** enhanced green fluorescent protein, p. 38
- ELISA** enzyme-linked immunosorbent assay, p. 45
- $\exp(x) = e^x$**  natural exponential function of x, p. 29
- exp.** experiment
- FACS** fluorescence-activated cell sorting, p. 13
- faR** far red fluorescent protein, p. 38
- $\gamma$**  gamma
- $\gamma(m, z)$**  gamma distribution with the positive parameters m and z, p. 29
- $\Gamma$**  Gamma
- $\Gamma(m)$**  gamma function with the positive parameters m, p. 29
- g** gram
- GFP** green fluorescent protein, p. 4
- h** hours
- $\mathcal{H}$**  Heaviside step function, p. 18

**HAU** haemagglutinating unit, p. 5

**HN** hemagglutinin-neuraminidase, p. 7

**HZI** Helmholtz Centre for Infection Research, p. 3

**IFIT** interferon-induced protein with tetratricopeptide repeats

**IFIT1** interferon-induced protein with tetratricopeptide repeats 1 also known as ISG56, p. 38

**IFN** interferon, p. 1

**i.i.d.** independent and identically distributed, p. 30

**IRF** interferon regulatory factor, p. 1

**ISG** interferon stimulated genes, p. 1

**ISG56** interferon stimulated gene 56, also known as IFIT1, p. 39

**IU** international unit, p. 44

**JAK** janus activated kinase, p. 1

**$\kappa$**  kappa

**kDa** kilodalton

**$\lambda$**  lambda

**l** liter

**L** likelihood function, p. 29

**$\mathcal{L}$**  log-likelihood function, p. 30

**ln** natural logarithm

**log** logarithm

**mCherry** monomeric cherry (red fluorescent protein), p. 4

**MFI** mean fluorescence intensity, p. 8

**$\mu$**  micro

**m** milli

**mex-file** Matlab executable file, p. 62

**min** minutes

**ml** milliliter

## *Abbreviations and symbols*

**MOI** multiplicity of infection

**MP** potentially DENV-E217A mutant specific model parameter

**mRNA** messenger RNA

**Mx** myxovirus resistance protein

**N** set of natural numbers  $\{1, 2, 3, \dots\}$

**N<sub>0</sub>** set of whole numbers  $\{0, 1, 2, 3, \dots\}$

**ng** nanogram

**NDV** newcastle disease virus

**NF- $\kappa$ B** nuclear factor kappa B

**NIH3T3** mouse embryonic fibroblast cell line

**NLS** nuclear localization signal, p. 38

**NS** non-structural protein of DENV, p. 38

**ODE** ordinary differential equation, p. 55

**P(A)** probability of  $A$

**P(A | B)** conditional probability of  $A$  under the condition  $B$

**PCS** sequence encoding for the 2A cleavage factor of the Thosea asigna virus

**PDE** partial differential equation, p. 55

**p.i.** post infection

**pg** picogram

**poly I:C** polyinosinic-polycytidylic acid

**prM** premembrane protein of DENV, p. 38

**p65** protein involved in nuclear factor kappa B heterodimer formation

**qPCR** quantitative polymerase chain reaction

**qRT-PCR** quantitative real time reverse polymerase chain reaction

**r** correlation coefficient

**r<sup>2</sup>** coefficient of determination

**R** set of real numbers

**R<sub>≥0</sub>** set of nonnegative real numbers

**RIG-I** retinoic-acid-inducible gene I

**RNA** ribonucleinacid

**RO** readout

**RPS9** 40S ribosomal protein S9

**RSAD2** radical S-adenosyl methionine domain containing 2

**SSA** stochastic simulation algorithm

**STAT** signal transducer and activator of transcription, p. 1

**STING** stimulator of interferon genes, p. 1

**TagRFP** red fluorescent protein tag

**TCID<sub>50</sub>** tissue culture infectious dose 50

**TCP** trans-complementation particle

**T<sub>div</sub>** time of cell division, p. 11

**TF** transcription factor

**T<sub>gen</sub>** time delay between nuclear translocation of NF- $\kappa$ B/IRF-7 and onset of IFN- $\beta$  expression, p. 9

**$\overline{T}_{\text{gen}}$**  mean value of  $T_{\text{gen}}$ , p. 9

**$\mathcal{T}_{\text{gen}}$**  simulated time delay between nuclear translocation of NF- $\kappa$ B/IRF-7 and onset of IFN- $\beta$  expression

**tGFP** turbo green fluorescent protein

**T<sub>sig</sub>** signaling delay from viral infection to nuclear translocation of the transcription factors NF- $\kappa$ B and IRF-7, p. 8

**$\overline{T}_{\text{sig}}$**  mean value of  $T_{\text{sig}}$ , p. 8

**$\mathcal{T}_{\text{sig}}$**  simulated signaling delay from viral infection to nuclear translocation of the transcription factors NF- $\kappa$ B and IRF-7

**U** unit

**$\mu$ l** microlitre

**USP18** ubiquitin specific peptidase 18

**UTR** untranslated region

**vol.** volume

*Abbreviations and symbols*

**v.u.** virus unit

**wt** wild-type

**YFP** yellow fluorescent protein, p. 4

## Acknowledgments